

#### **Archive ouverte UNIGE**

https://archive-ouverte.unige.ch

Thèse 2018

**Open Access** 

This version of the publication is provided by the author(s) and made available in accordance with the copyright holder(s).

High-resolution simulations of the solar photosphere with focus on the polarimetry of the solar continuum

-----

Calvo, Flavio

#### How to cite

CALVO, Flavio. High-resolution simulations of the solar photosphere with focus on the polarimetry of the solar continuum. Doctoral Thesis, 2018. doi: 10.13097/archive-ouverte/unige:115257

This publication URL: <a href="https://archive-ouverte.unige.ch/unige:115257">https://archive-ouverte.unige.ch/unige:115257</a>

Publication DOI: 10.13097/archive-ouverte/unige:115257

© This document is protected by copyright. Please refer to copyright holder(s) for terms of use.

#### ISTITUTO RICERCHE SOLARI LOCARNO

Dr. Sc. ETH O. Steiner

# High-resolution simulations of the solar photosphere with focus on the polarimetry of the solar continuum

#### THÈSE

présentée à la Faculté des Sciences de l'Université de Genève pour obtenir le grade de Docteur ès Sciences, mention Astrophysique par

Flavio Carvo

de

Genève (GE)

Thèse № 5281

Le Grand-Saconnex (GE)
Imprimerie du Cachot
2019



#### DOCTORAT ÈS SCIENCES, MENTION ASTRONOMIE ET ASTROPHYSIQUE

#### Thèse de Monsieur Flavio CALVO

intitulée :

## «High-resolution Simulations of the Solar Photosphere with Focus on the Polarimetry of the Solar Continuum»

La Faculté des sciences, sur le préavis de Monsieur G. MEYNET, professeur ordinaire et directeur de thèse (Département d'astronomie), Monsieur O. STEINER, docteur et codirecteur de thèse (Kiepenheuer-Institut für Sonnenphysik, Freiburg, Deutschland - Istituto Ricerche Solari Locarno, Svizzera), Monsieur C. GEORGY, docteur (Département d'astronomie), Monsieur M. BIANDA, docteur (Istituto Ricerche Solari Locarno, Svizzera), Monsieur J. LEENAARTS, docteur (Institute for Solar Physics, Department of Astronomy, Stockholm University, Sweden), Monsieur R. CASINI, docteur (High Altitude Observatory, National Center for Atmospheric Research, Boulder, USA), autorise l'impression de la présente thèse, sans exprimer d'opinion sur les propositions qui y sont énoncées.

Genève, le 29 mars 2018

Thèse - 5281 -

Le Doven

N.B. - La thèse doit porter la déclaration précédente et remplir les conditions énumérées dans les "Informations relatives aux thèses de doctorat à l'Université de Genève".

#### Jury:

Advisors: Prof. Georges Meynet - Université de Genève

Dr. Oskar Steiner - Kiepenheuer-Institut

für Sonnenphysik

Examinators: Dr. Michele BIANDA - Istituto Ricerche Solari

Locarno

Dr. Cyril Georgy - Université de Genève

Dr. Jorrit Leenaarts - Stockholms universitet

External reviewer: Dr. Roberto Casini - High Altitude Observatory,

National Center for Atmospheric Research

#### Remerciements

Si les scientifiques sont des nains sur des épaules de géants, cette thèse doctorale est peut-être elle aussi un petit pas dans un projet commun et de longue haleine, qui se poursuit au fil des générations. Je souhaiterais dédier cette thèse à tous les nains qui ne se sont pas imposés ou qui ne s'imposeront jamais dans la mémoire collective comme les géants du passé.

Aussi souhaiterais-je dédier ce travail de recherche à toutes celles et ceux qui l'ont rendu possible, à commencer par ma famille, qui m'a toujours encouragé à faire de ma vie un rêve, et de mes rêves une réalité. L'équipe de recherche de l'IRSOL a aussi joué un rôle déterminant : à Michele Bianda je lui dois son optimisme, capable à lui seul de déplacer les plus imposantes montagnes tessinoises ; Renzo Ramelli a également embarqué dans ce bateau depuis longtemps, et on lui doit d'avoir écrit plus d'une page dans l'histoire de l'institut ; à Oskar Steiner, qui a été mon superviseur de thèse jusqu'au bout de cette aventure, je lui suis infiniment reconnaissant et soulignerai ici sa patience sans bornes et ses excellents conseils ; je me souviendrai de Luca Belluzzi et d'Edgar S. Carlín Ramírez pour leur art de raconter avec simplicité les aspects les plus sombres du transfert radiatif ; de Boris "Jack" Liver j'ai appris à faire de l'air frais et du soleil le remède à presque tous les maux, lui qui grâce à sa double passion pour l'informatique et le trail a toujours été présent pour détendre l'atmosphère.

D'autres personnes se sont retrouvées à l'IRSOL de passage : des étudiants et des civilistes, des membres de l'institut à temps partiel, la famille des membres de l'IRSOL, qui ont à leur manière donné vie à l'institut. En particulier je me souviendrai de Katya Gobbi et de Mari Gianpaolo, dont le professionnalisme est à tous les égards digne d'admiration. De nombreux soupés ont été partagés, avec Mathis Engelhard, avec Valentin Stalder, avec Ernest Alsina Ballester, avec Daniel Gisler, avec Agne Puckaite et avec bien d'autres, et tous ont été source d'inspiration. Deux autres doctorants, Gioele Janett et Emilia Capozzi, ont aussi été une compagnie amicale et enthousiaste, avec qui échanger de nouvelles idées et soulever les questions clés. Je vous souhaite bonne suite à tous les deux !

Aussi suis-je très reconnaissant avec le Prof. Georges Meynet, qui a accepté de superviser ce projet du côté de l'Université de Genève. Pour finir, je souhaiterais remercier autant Natalia Shchukina que Jiří Štěpán pour leur appui dans le projet du Chapitre 6, ainsi que Jhih-Huang Li, pour ses bons conseils concernant les démonstrations dans l'Appendice au Chapitre 5.

Cette thèse doctorale a été financée par le Fonds National Suisse, par le biais de la bourse ID 200020\_157103/1, et par une allocation du Centre Suisse de Calcul Scientifique (CSCS), avec numéros de projet s560 et sm14. Les simulations numériques ainsi que le post-traitement des données ont été effectués sur les machines nommées Rothorn, Piz Dora et Piz Daint du CSCS.

#### Acknowledgements

If scientists are dwarfs standing on the shoulders of giants, this Ph.D. work is maybe also one small step in a common and long-term project carried out by past and future generations. I wish to dedicated this manuscript to all the dwarfs who are not or will never be remembered as the giants of the past. I dedicate it to all those who inspire new generations of scientists, and whose work is a small piece in an enormous puzzle.

I also wish to dedicate this work to all those who made it possible, starting with my family, who always encouraged me to pursue my dreams and to make them real. A key part was also played by all the staff of the IRSOL institute: by Michele Bianda, whose optimism alone is capable of moving mountains, by Renzo Ramelli, who is also in this boat since a long time and is definitively a co-writer of the history of the institute, by Oskar Steiner, who became my actual Ph.D. supervisor and whose patience and excellent advice accompanied this project until the very end, by Luca Belluzzi and Edgar S. Carlín Ramírez, who are two masters at explaining the darkest aspects of radiative transfer, by Boris "Jack" Liver, who would resolve all kinds of problems in ways only him could think of, and whose double passion for computer engineering and trail running would provide me with a bowl of fresh air when it was most required.

Many other persons were "transient" at IRSOL: students or civil servants, partial-time IRSOL staff, and families of the IRSOL staff, and made IRSOL become a living place. Among the partial-time staff, I particularly remember Katya Gobbi and Mari Gianpaolo for their admirable professionalism. Many dinners were shared with Mathis Engelhard, with Valentin Stalder, with Ernest Alsina Ballester, with Daniel Gisler, with Agne Puckaite and with many others who always were a source of inspiration. The two other Ph.D. students at the time, Gioele Janett and Emilia Capozzi, were very friendly company, always willing to exchange new ideas, raise the critical questions, and give life to the institute. Good luck to both of you!

I am also very grateful to Prof. Georges Meynet, who accepted the supervision of this project from the University of Geneva. Last but not least, I would like to thank both Natalia Shchukina and Jiří Štěpán for their enthusiastic support with the project of Chapter 6, as well as Jhih-Huang Li for his useful advice regarding the proofs in the Appendix to Chapter 5.

This Ph.D. thesis was supported by the Swiss National Science Foundation under grant ID 200020\_157103/1 and by a grant from the Swiss National Supercomputing Centre (CSCS) in Lugano under project IDs s560 and sm14. The numerical simulations and the post-processing were carried out at CSCS on the machines named Rothorn, Piz Dora and Piz Daint.

## Contents

1	Intr	Introduction				
<b>2</b>	Bac	kgroui	nd information	•		
	2.1	Radia	tive magnetohydrodynamic simulations	4		
		2.1.1	Historical overview	4		
		2.1.2	A general description of MHD	(		
		2.1.3	Radiative MHD applied to the Sun	8		
		2.1.4	The CO <sup>5</sup> BOLD code	9		
		2.1.5	The numerical simulation runs	1		
	2.2	The p	hysics of the polarized continuum	1		
		2.2.1	Scattering processes in the context of the formalism of			
			Landi Degl'Innocenti & Landolfi	1		
		2.2.2	Non-scattering processes	19		
		2.2.3	The emergence of linear polarization	19		
		2.2.4	Radiation-matter interactions	2		
	2.3	Polari	zed radiative transport in the continuum	2		
		2.3.1	Simplifications and approximations	2		
		2.3.2	Derivation of the equations for the polarized transport			
			of light in the continuum	2		
	2.A	Detail	s on the formalism of LL04	28		
		2.A.1	Radiative transfer equation for polarized radiation	28		
		2.A.2	Radiative transfer coefficients	28		
		2.A.3	The radiation field tensor	30		
		2.A.4	Einstein coefficients	30		
		2.A.5	6-j symbols	30		
		2.A.6	The density matrix	30		
	2.B	Quadr	rature formulas	3		
		2.B.1	The product quadrature with Gauss-Legendre nodes	3		
		2.B.2	Lobatto's quadrature	3		
		2.B.3	The double-Gauss quadrature	3		
		2.B.4	Lebedev's quadrature	3		
	Bibl	iograph	-	3.		
3	Cor	ıstrain	ts on the magnetic field	39		
	3.1	Overv	3	3		
	3.2	Const	rained transport with the CO <sup>5</sup> BOLD code	4		
	3.3		methods for ensuring $\nabla \mathbf{B} = 0 \dots \dots$	4		
	-	3.3.1	Advection of magnetic monopoles	4		

x Contents

		3.3.2 Divergency cleaning	44
	3.4	A code for divergency cleaning	44
		3.4.1 Magnetic monopoles associated to numerical errors	45
		3.4.2 The Hodge projection scheme	45
		3.4.3 Implementation of the BiCGSTAB method	46
		3.4.4 Boundary conditions and ghost cells	47
	3.5	Magnetic monopoles in CO <sup>5</sup> BOLD simulations	48
	3.6	A potential magnetic field	49
		3.6.1 General construction	49
		3.6.2 The p200 magnetic configuration	51
	Bibl	iography	52
4	Noi	n-magnetic photospheric bright points	55
	4.1	Introduction	57
	4.2	nMBPs from the simulations	58
	4.3	From a nMBP toy-model to a recognition algorithm	62
	4.4	Physical properties of nMBPs	64
	4.5	nMBPs in intensity maps of virtual observations	71
	4.6	Conclusion	73
	Bibl	iography	75
5	Str	ucture of the Balmer jump	79
	5.1	Introduction	81
	5.2	Absorption coefficient	82
	5.3	Density of quantum states	85
	5.4	Einstein coefficients	86
		5.4.1 Reduced matrix elements	86
		5.4.2 Radial wavefunctions	87
	5.5	Total absorption coefficient at the Balmer limit	89
		5.5.1 Continuity of the total absorption coefficient	89
		5.5.2 Analytic expression for the total absorption coefficient .	90
	5.6	Numerical modelling of the total cross-section	91
	5.7	Conclusion	96
	5.A	Reduced matrix elements of the dipole operator	97
	5.B	Asymptotic properties of the Whittaker $M$ function $\ldots$	98
	Bibl	iography	101
6	Pol	arization in the continuum	103
	6.1	Introduction	103
	6.2	The physics and equations	106
		6.2.1 Generalities	106
		6.2.2 Scattering and non-scattering processes	109
		6.2.3 Methods used for the solution of the equations	111

Contents xi

7	Cor	clusio	n	133
	Bibl	liograph	ny	. 129
	6.5		ssion and conclusions	
		6.4.4	The contribution of the far red wing of Lyman- $\beta$	
		6.4.3	Centre-to-limb variation of polarization	. 123
		6.4.2	Limb-darkening	. 121
		6.4.1	Polarization maps at disc centre	. 119
	6.4	The co	ontinuum from 3D models	. 118
		6.3.3	Centre-to-limb variation of polarization	. 117
		6.3.2	Limb-darkening	. 116
		6.3.1	Temperature structure	. 114
	6.3	Obser	vational data and 1D models	. 112

### Introduction

Research often starts with sketchy problems, leads us through unforeseen paths, provides us surprising answers, and raises unexpected questions for us to answer. This modest contribution to solar physics is no exception. The projects and results that comprise this work were achieved in the Istituto Ricerche Solari Locarno (IRSOL), a small and independent research institute located in the southern Italian-speaking region of Switzerland. The IRSOL observatory is dedicated to solar research and it is a leading institute in the field of observational high-precision spectropolarimetry. The idea of studying the linear polarization in the solar continuum and its centre-to-limb variation (CLV) with the help of numerical simulations emerged quite naturally. At the time I arrived at the observatory, corresponding observational measurements were already planned. The centre-to-limb variation of linear polarization (CLVP) in the continuum radiation in stellar atmospheres was already predicted by Chandrasekhar in the 40s, but a precise measurement in the case of the Sun still awaits completion because of the required high degree of absolute polarimetric accuracy. The IRSOL institute started witnessing its forthcoming growth with the arrival of Luca Belluzzi, a specialist in theoretical spectropolarimetry, and Oskar Steiner, a specialist in numerical simulations of the solar and stellar atmospheres. Producing numerical models to confront to the observations was a logical step, and a task that was proposed to me, under the supervision of Oskar Steiner, after my own arrival to the institute at the end of the year 2013.

It was surprisingly easy to get an account at the nearby Swiss National Supercomputing Centre (Centro Svizzero di Calcolo Scientifico, CSCS), and shortly after the beginning of my Ph.D. we could already start simulating dynamic models of the solar photosphere and convective layers beneath it by using the already-existing Conservative Code for the Computation of Compressible Convection in a BOx of L Dimensions with l=2,3 (CO<sup>5</sup>BOLD) (magneto-)hydrodynamic computer code. We constructed a few high-resolution magnetic models, and faithfully reproduced the solar granulation pattern due to the convecting plasma. The darker intergranular lanes with its conspicuous magnetic bright features were also clearly visible. We also started non-magnetic simulations, that revealed again the solar granulation and, interestingly, small bright features in the intergranular lanes that obviously were of non-magnetic origin, and smaller than the corresponding magnetic features. We called them "non-magnetic bright points" and started studying them, first individually, and then

collectively with a statistical approach. This study lead to a publication, that is found hereafter in Chapter 4, and it also lead us aside of our initial project of studying the linearly polarized solar continuum. This was only one of the many detours that were to come before focusing on the polarized continuum.

A well-known issue with numerical magneto-hydrodynamic simulations is their limited ability to preserve the solenoidal structure of physical magnetic fields. A great effort was done in the implementation of the  $CO^5BOLD$  code we started using in order to avoid non-solenoidal magnetic fields arising from discretization errors. However, since no numerical scheme can prevent the appearance of round-off errors, we decided to have a close look to the behaviour of magnetic fields in our own simulations. A summary of the problematic and a report of the performance of the  ${\rm CO}^5{\rm BOLD}$  code with our models is found in Chapter 3.

In an attempt to come back to the initial problem, I returned to the alreadyexisting scientific literature regarding polarization in the solar continuum. Various papers were reporting the displacement of the Balmer jump due to the Stark effect that results in the broadening of spectral lines. This specific information caught my attention, since a displacement of the Balmer jump would also imply a different definition of the Balmer jump than merely the Balmer limit corresponding to the threshold energy at which a photon is able to photo ionize an initially bound electron in the n=2 energy level of the Hydrogen atom. The existence of a discontinuity near the Balmer limit that would be displaced due to the Stark effect was a possibility that I refused to believe. For this reason I decided to start from quantum mechanical grounds and use a modern formalism in order to prove the continuity of the total cross-section for bound-bound and bound-free process in the isolated Hydrogen atom. By including different broadening mechanisms, I proposed a precise meaning to the concept of "Balmer jump" and showed how its position would be shifted according to the amount of broadening. This study lead to a second publication that is also found hereafter, on Chapter 5.

The study of linear polarization in the solar continuum and its centre-to-limb variation was a long-term endeavour that lead to unexpected projects, and that also required the development of computational tools in order to numerically solve the radiative transfer equations in the context of the solar continuum, but that eventually saw light at the very end of this Ph.D. The confrontation of already-existing calculations and observations to our own simulations reveals surprising results and raises many new questions and ideas. This initial (and final) project is presented in Chapter 6.

# **Background information**

$\mathbf{nt}$	$\mathbf{e}\mathbf{n}$	${ m ts}$
	$\mathbf{nt}$	nten

2.1	Radiat	ive magnetohydrodynamic simulations	4
	2.1.1	Historical overview	4
	2.1.2	A general description of MHD	6
	2.1.3	Radiative MHD applied to the Sun $\ldots \ldots \ldots$	8
	2.1.4	The $CO^5BOLD$ code	9
	2.1.5	The numerical simulation runs	13
2.2	The ph	sysics of the polarized continuum	<b>15</b>
	2.2.1	Scattering processes in the context of the formalism of	
		Landi Degl'Innocenti & Landolfi	15
	2.2.2	Non-scattering processes	19
	2.2.3	The emergence of linear polarization $\dots \dots$ .	19
	2.2.4	Radiation-matter interactions	21
2.3	Polariz	ed radiative transport in the continuum	22
	2.3.1	Simplifications and approximations	22
	2.3.2	Derivation of the equations for the polarized transport	
		of light in the continuum	22
2.A	Details	on the formalism of LL04	<b>28</b>
	2.A.1	Radiative transfer equation for polarized radiation $$	28
	2.A.2	Radiative transfer coefficients	28
	2.A.3	The radiation field tensor	30
	2.A.4	Einstein coefficients	30
	2.A.5	6-j symbols	30
	2.A.6	The density matrix	30
2.B	Quadra	ature formulas	31
	2.B.1	The product quadrature with Gauss-Legendre nodes $$ .	31
	2.B.2	Lobatto's quadrature	32
	2.B.3	The double-Gauss quadrature	33
	2.B.4	Lebedev's quadrature	33
Bibli	ography		35

# 2.1 Radiative magnetohydrodynamic simulations

#### 2.1.1 Historical overview

The use of the word magnetohydrodynamics (MHD) dates back to the early 1940s. In 1946, Alfvén referred to a theory according to which "the sunspots are due to a new type of wave, called magneto-hydrodynamic waves, which are produced through convection near the Sun's centre and are transmitted along the magnetic lines of force of the general magnetic field out of the surface, where they cause sunspots". This theory is of course known to be inexact nowadays, but at the time, numerical simulations had not vet seen the light of day and were probably not even conceived as feasible in any near future, and instrumentation was far behind when compared to the present developments. However, theories regarding the dynamics inside the solar atmosphere were already circulating, and observations would provide only very indirect ways to validate them. Making predictions about how the three-dimensional (3D) plasma dynamics in the atmosphere and beneath it would affect the two-dimensional (2D) observations of the surface layers and the observed spectra would also be a difficult and sometimes speculative task, since the tools to numerically solve the radiative transfer equation in a realistic atmosphere were missing. The development of MHD, for which Alfvén received the Nobel Prize in 1970, was a decisive step in many topics, and in particular in the understanding of the solar atmosphere.

It took less than a decade till the first computers were used in the field of astrophysics, and more specifically for solar physics. As early as 1964, Feautrier proposed improvements for the numerical solution of the radiative transfer equations. In 1972, Wittmann had already an LTE radiative transfer code including polarization. One of the first non-LTE radiative transfer codes would be presented in the same year by Auer et al. (1972), and parts of the more efficient MULTI code later developed by Carlsson (1986) are still used in more recent non-LTE radiative transfer codes. Before these papers describing the codes were published, radiative transfer computations were already carried out numerically, as it can be seen in Auer & Mihalas (1969). Those early codes aimed at investigating the solar atmosphere by fitting observed spectra. One would not start from model atmospheres by solving the magnetohydrodynamic equations, but would rather start from the observed profiles of a variety of spectral lines and derive a model atmosphere that would best fit these profiles, or one would try to fit the limb-darkening of the continuous radiation. The idea of inversion was born around that time, resulting in the first one-dimensional semi-empirical models of the solar atmosphere. The well-known HSRA model of the solar atmosphere was presented by Gingerich et al. (1971). In the paper of Holweger & Mueller (1974), another model atmosphere is used to derive the

solar abundance of Barium, and the paper of Fontenla et al. (1993) is regularly cited almost 25 years after its publication for the valuable semi-empirical 1D models it proposed.

In parallel, computer codes were developed to simulate different problems arising from solar physics and magnetohydrodynamics. Already in the 1970s some effort was done in developing an MHD particle code (Leboeuf et al. 1978) in order to simulate the interaction of the solar wind with the magnetosphere, and early 2D simulations of the magneto-convection were carried out by Peckover & Weiss (1978). Independently, the MHD wave propagation in the solar chromosphere had already been studied with numerical simulations by Shibata (1983). It is certainly fair to say that simulations of the solar granulation really made their appearance in the 1980s, following the efforts of Nordlund (1982), who developed a code using Fourrier techniques, but restricting it to radiative hydrodynamics (no magnetic fields), which lead to an extended review of the hydrodynamics of the solar convection by Nordlund (1985a). The first 3D radiative MHD simulation was reported in conference papers of Nordlund (1983, 1984, 1985b, 1986). A quantitative comparison of the simulated solar surface convection to the observations was carried out later by Stein & Nordlund (2000).

The computational developments taking place during the last decades of the 20th century marked a new era in the study of the solar and stellar atmospheres. The Sun remained for a long time the only star with its disc resolved, and being the closest star, it provided and still provides a natural and very special physics laboratory for the broader study of stellar physics. It was not until 1989 that a bright feature was detected in a star other than the Sun (Buscher et al. 1990), not to mention stellar granulation, that was directly observed in a star other than the Sun only a few months ago (Paladini et al. 2017). However, and in spite of the proximity of the Sun, its sub-surface layers required at the time indirect helioseismic techniques to be "observed". Still now, no experiment can be carried out in-situ, and all direct information available is solely given by the light and particles (e.g. neutrinos) that are reaching us from the Sun. The ability to numerically simulate the Sun marked an incredible step forward, since it brought a physics laboratory 149 millions kilometres away from the Earth right at home, inside computers.

Some care should however be taken when comparing simulations with the real Sun. Hydrodynamic simulations are essentially parameter-free (Stein & Nordlund 2000): the only fundamental parameters, which are the effective temperature, the surface gravity, and the chemical composition of the plasma are fixed by observations and stellar evolution models of the Sun. However, the spatial and temporal resolution of the numerical schemes limit the effective viscosity and electric resistivity. Thus, the numerical schemes used in such simulations introduce a numerical viscosity and resistivity that is orders of magnitudes higher than the actual solar values. In magnetohydrodynamic

simulations the specific configuration of the initial magnetic field plays a determinant role, especially in the highest layers of the solar atmosphere, and it is also considered to be a free parameter. In all realistic simulations the equation of state and the radiative transfer must also encompass detailed physics.

In order to compare simulations to observations, one additional important step is required. The output of simulations (e.g. 3D scalar and vector fields representing the density, the temperature, the velocity field and the magnetic field at every point of a discretized computational grid) is very different from the output of observations (e.g. a monochromatic linear polarization map, an intensity spectrum along a slit, an intensity map at a given wavelength, etc.). The process taking as input a simulated model atmosphere and that outputs any of the observable quantities is called radiative transfer, and the output provides synthetic observations. The synthetic observations can be further degraded in order to mimic the effects of diffraction or diffused light on an instrumental set-up, and finally be compared to observations with the given instrument.

When simulations allow the reproduction of observable quantities in a trust-worthy manner, the underlying simulated atmosphere is assumed to be realistic. Diagnosis and experiments that are impossible to carry out on the real Sun can then be carried out inside simulations. Is some feature appearing in the solar spectra a consequence of velocity gradients or of non-LTE effect? Is the magnetic field responsible for enhanced continuum polarization in intergranular lanes or is the anisotropy alone to blame for it? This is the kind of questions we can deal with by comparing magnetic and non-magnetic simulations, or by directly modifying the underlying structure of the atmosphere before computing radiative transfer.

#### 2.1.2 A general description of MHD

The magnetohydrodynamic (MHD) equations are derived by coupling the fluid dynamics equations expressing the conservation of mass, momentum and energy, with the Maxwell equations describing the dynamics of electromagnetic fields. In their conservative form, these equations are given by

$$\frac{\partial \rho}{\partial t} + \nabla \cdot (\rho \mathbf{v}) = 0,$$

$$\frac{\partial (\rho \mathbf{v})}{\partial t} + \nabla \cdot \left( \rho \mathbf{v} \mathbf{v} + \left( P + \frac{\mathbf{B} \cdot \mathbf{B}}{2} \right) \mathbf{I} - \mathbf{B} \mathbf{B} \right) = \rho \mathbf{g},$$

$$\frac{\partial \mathbf{B}}{\partial t} + \nabla \cdot (\mathbf{v} \mathbf{B} - \mathbf{B} \mathbf{v}) = 0,$$

$$\frac{\partial (\rho e_{\text{tot}})}{\partial t} + \nabla \cdot \left( \left( \rho e_{\text{tot}} + P + \frac{\mathbf{B} \cdot \mathbf{B}}{2} \right) \mathbf{v} - (\mathbf{v} \cdot \mathbf{B}) \mathbf{B} + \mathbf{F}_{\text{rad}} \right) = \rho \mathbf{g} \cdot \mathbf{v}, \quad (2.1)$$

where  $\rho$  is the density,  $\mathbf{v}$  is the velocity field, P is gas pressure,  $\mathbf{I}$  is the identity  $3 \times 3$  matrix,  $\mathbf{B}$  is the magnetic field,  $e_{\text{tot}} = e_{\text{int}} + e_{\text{kin}} + e_{\text{mag}}$  is the total energy per unit mass including the thermal (internal), the kinetic and the magnetic contributions,  $\mathbf{g}$  is the gravitational acceleration and t is time. This equations are closed by an additional equation of state  $P = P(\rho, e_{\text{int}})$  that relates pressure to density and internal energy. We noted  $\mathbf{c} = \mathbf{ab}$  the tensor product of  $\mathbf{a}$  and  $\mathbf{b}$ , i.e.  $e_{ij} = a_i b_j$ , and the dot product generalizes, when operating between two tensors or between a derivative and a tensor, to the contraction of the last index of the first operand with the first index of the last operand: for instance,  $(\nabla \mathbf{c})_j = \sum_i \partial_i c_{ij}$ . These equations express the conservation of matter through the continuity equation, of momentum (note on the right hand side of the second equation the gravity term), of magnetic flux, and of total energy. The last equation couples the dynamics of the plasma with the transport of light through the radiative flux

$$\mathbf{F}_{\rm rad} \equiv \int_{\nu} \int_{\mathcal{S}^2} I_{\nu}(\vec{\Omega}) \hat{\mathbf{n}} \, \mathrm{d}\Omega \mathrm{d}\nu. \tag{2.2}$$

Unless this term is neglected or approximated, the MHD equations should be coupled with the radiative transfer (RT) equation

$$\frac{1}{\rho\kappa_{\nu}} \left( \hat{\mathbf{n}} \cdot \mathbf{\nabla} \right) I_{\nu} = S_{\nu} - I_{\nu}, \tag{2.3}$$

where  $\nu$  is the frequency,  $I_{\nu}$  is the intensity at the given frequency,  $\Omega$  is the surface of the solid angle  $\vec{\Omega} = \Omega \hat{\mathbf{n}}$ ,  $\hat{\mathbf{n}}$  is a unit vector normal to the surface, and  $\mathcal{S}^2$  is the ordinary sphere.

Since the absorption coefficient, the intensity, and the source function in the radiative transfer equation depend on frequency (or wavelength), discretizing the spectrum and solving the RT equation at all grid points is computationally expensive for the particular task of finding the total radiative flux. One possible simplification is to consider the monochromatic version of the equation, in which wavelength dependent opacities are replaced by Rosseland mean opacities, monochromatic intensity is considered, and the source function is the averaged Planck function over the whole spectrum.

The monochromatic approach is however in some cases an excessive simplification. This is due to the fact that in optically thin layers with respect to the continuum wavelength, the contribution to the total flux mainly comes from those lines for which monochromatic optical depth is unity on those layers, which typically represent a small fraction of the spectrum (Nordlund 1982). To solve this problem, the depth scale of the stellar atmosphere is split into ranges  $R_i$ , and the wavelength range is split into disconnected bands  $B_i$ , with the property that  $\cup_i B_i$  is the whole spectrum,  $B_i$  are disjoint, and for any wavelength  $\lambda \in B_i$ , the layer at which the optical depth  $\tau_{\lambda}$  of that particular

wavelength is unity resides inside  $R_i$ . Schematically, each wavelength band maps a different depth of the atmosphere. In the same way as Rosseland mean opacity is defined, the mean opacity of any given band is defined by restricting integration over the wavelength band. This collection of mean opacities in different bands are called *opacity bands*. Similarly, intensity bands  $I_i$  are defined, as well as bands for the source function. The RT equation is then solved for a small number of opacity bands, and the radiative flux is then rewritten as a sum instead of an integral,

$$\mathbf{F}_{\rm rad} \simeq \sum_{i} \int_{\mathcal{S}^2} I_i(\vec{\Omega}) \hat{\mathbf{n}} \, d\Omega d\nu,$$
 (2.4)

and the accuracy of the method can be adjusted by increasing the number of bands. This approximate method is called the *Opacity Binning Method (OBM)*. We only gave here the general idea introduced in Nordlund (1982). More details and later improvements can also be found in Ludwig (1992), Ludwig et al. (1994) and Vögler (2004).

In order to solve the coupled system of equations (2.1) to (2.3), we use the COnservative COde for the COmputation of COmpressible COnvection in a BOx of L Dimensions with l=2,3, known as the CO<sup>5</sup>BOLD code (Freytag et al. 2010).

#### 2.1.3 Radiative MHD applied to the Sun

It is tempting to compare the simulations of the solar atmosphere with the simulations of the terrestrial atmosphere carried out by meteorologists. Solar simulations still have a quite modest spatial resolution when compared to the size of possible features in the solar atmosphere. With every increase of resolution as a consequence of increasing computational power of computers, smaller scale structure became visible, suggesting that substructures that might play a crucial role in the overall dynamics are not yet resolved. This seems to be specifically true for the turbulent magnetic field, which is possibly structured in form of strong (kG) fluxtubes on scales smaller than 50 km (Stenflo 2011). Terrestrial and solar simulations are however very different. Simulations of the solar atmosphere cover only a small part of the Sun, and more importantly the initial conditions are not the result of observations at any particular time, as is the case with meteorological simulations. The fundamental difference between these two kind of simulations is that solar simulations are not forecasting the state of the solar atmosphere at any given time (but see Riethmüller et al. 2017, for an attempt of a forecast). Only statistical quantities should be compared to observations: averaged spectra, intensity contrast, size of granules, frequency of appearance and average size of some given feature... are some usual examples.

When simulating stellar atmospheres, two different types of star envelopes should be considered. Main-sequence stars with a mass  $M \lesssim 1.5 M_{\odot}$  (the exact value also depends on metallicity), like the Sun, have a steep enough temperature gradient in the outer envelope that makes heat transfer more efficient by convection than by radiation. The outer envelope is hence unstable to convection. Instead, stars with a mass  $M \gtrsim 1.5 M_{\odot}$  have a radiative envelope. Away of the main-sequence, massive stars like red giants and supergiants also have a convective envelope, but the convective cells are much bigger; their size is of the order of the radius of the star. In some sense, convective envelopes are more complicated, since convection in a ionized plasma produces both magnetic field and a small-scale granulation pattern. These two features play a fundamental role in the global dynamics. For solar-like stars, resolving these structures while simulating the whole star would require computational resources that even now are orders of magnitude greater than what is available. For this reason, simulations of the solar atmosphere are carried out on small volumes, with periodic boundary conditions in the horizontal direction. Topologically, the simulated Sun is hence a torus. This kind of simulations are referred to as "box in a star" simulations. More importantly, the boundary conditions at the top of the solar atmosphere are only partially realistic, since the physical quantities can only be fixed at infinity.

Massive stars are more homogeneous, either they have a radiative envelope, or granules with sizes comparable to the stellar radius, allowing realistic simulations at a significantly lower resolution (see e.g. Freytag et al. 2002; Chiavassa et al. 2011). With a reasonably small mesh it is hence possible to simulate the entire star, producing "star in a box" simulations.

#### 2.1.4 The CO<sup>5</sup>BOLD code

The CO<sup>5</sup>BOLD code and a history of magnetohydrodynamic simulations is extensively discussed in Freytag et al. (2012). In present days, the CO<sup>5</sup>BOLD code is used for the simulation of a variety of stellar atmospheres, among which the Sun, solar-type stars, red giants and white and brown dwarfs are the main examples (Straus et al. 2017). This large spectrum of simulations is permitted by a modular construction of the code, allowing to choose among different solvers: a hydrodynamic module or a magnetohydrodynamic module, and radiative transfer schemes with short or long characteristics with specific boundary conditions. In this section we will give a brief description of the modules we actually use for the simulation of the surface layers of the Sun.

As stated in Sect. 2.1.1, our simulations are essentially parameter-free. There is for instance no micro- or macroturbulence parameters, since spatial and temporal averages of spectral line profiles calculated from simulations properly reproduce the shape of observed spectral lines, thanks to the presence of a self-consistent velocity field evolving with the simulations. The usual pa-

rameters characterising stars (effective temperature, surface gravity and chemical composition) must however be set, as well as the many numerical parameters (solvers, boundary conditions, numerical viscosity and time stepping are a few examples). For this purpose, a "parameter file" is provided to CO<sup>5</sup>BOLD, together with a file with opacities (possibly providing a few opacity bands) and a file with interpolation coefficients for the equation of state. Again, we will focus here our discussion on the main parameters we use in our simulations. A complete list is available in the CO<sup>5</sup>BOLD user manual (see e.g. Freytag et al. 2010).

Global parameters and boundary conditions: The surface gravity is set to the solar value,  $q = 27500 \,\mathrm{cm \, s^{-2}}$ , or  $\log_{10}(q \,[\mathrm{cm \, s^{-2}}]) = 4.44$ . The chemical composition is set through the opacity bands and the equation of state and is discussed in the next paragraph. The effective temperature is set indirectly through the boundary conditions. The boundary conditions at the sides of the box perpendicular to the horizontal axes are set periodic both for the magnetohydrodynamic solver and for the radiative transfer module. The boundary conditions at the bottom are set to "inoutflow2". The implementation is non-trivial, but it describes an open lower boundary for which the entropy inflow is specified and the adjustment rate of entropy and pressure in this lower layer is fixed in order to damp out possible oscillations. The entropy inflow parameter must be determined by trial and error untill the desired effective temperature is reached. The top boundary condition is set to "transmitting", for which density is extrapolated out of the box by assuming it to be exponentially decreasing. This is achieved by assuming the density scale height to be proportional to the pressure scale height for some provided constant. Temperature is also adjusted towards a specified fraction of the effective temperature at a given rate. The scale height of the optical depth at the upper boundary is also adjusted by a parameter for the radiative transfer module.

The magnetic boundary conditions are also periodic at the sides. At the bottom they depend on the model; we tried two different kinds, either "vertical", which is a constant extrapolation of the vertical component while the transversal components are fixed to zero, or "inoutflow", which allows to fix a strength of the (horizontally) advected magnetic field by ascending material. The magnetic boundary conditions at the top are set to "vertical". We also implemented the "mixed" boundary conditions, which are equivalent to "vertical" in regions of down-flows, or make a constant extrapolation of the magnetic field in regions of up-flows. With the "mixed" boundary conditions, we aimed at preventing a numerical instability that we encountered, but after the problem was sorted out two parallel runs with "vertical" and "mixed" conditions stayed stable.

Opacities and equation of state: Opacities are given in a separate file as a function of gas pressure P and temperature T, for a number of values of  $\log_{10}(P)$  and T. These tables are interpolated in CO<sup>5</sup>BOLD. They contain monochromatic Rosseland mean opacities, as well as five additional bands. They are based on a 1D MARCS model atmosphere from the Montpellier-Uppsala group (Gustafsson et al. 2008) and are extensively discussed in Ludwig & Steffen (2013), together with the particular CO<sup>5</sup>BOLD implementation of the opacity binning method. Interpolation coefficients for the equation of state are also provided in a separate file by the CIFIST (Cosmological Impact of the First STars) group.

Time management: CO<sup>5</sup>BOLD provides adaptive time stepping. The time step is re-evaluated at each iteration and at each cell both for the (M-)HD module and the RT module, and the minimal value is chosen as the final time step. For the (M-)HD module, the time step is fixed by the Courant condition, which states that a magnetosonic wave (or sound wave in the non-magnetic case) should cross at most one computing cell during a single time step. In practice a parameter is fixed to limit the time step to a fraction of the Courant upper bound, that is taken as a recommendation for the next step. This value might be revised and the time step recomputed if the next upper bound is below the recommended value. For some simple linear problems, without radiative transport, this procedure is guaranteed to be stable. For radiative transport the time step that ensures numerical stability can only be estimated. It is taken to be a fraction of the characteristic time scale of a small sinusoidal disturbance with a wavelength of the grid size in a homogeneous background and grey radiative energy exchange (Freytag et al. 2010).

Parallelization: The CO<sup>5</sup>BOLD code is OpenMP parallel. This means that OpenMP tasks run concurrently and share memory. The code is hence suitable for running on (single) big nodes with limited NUMA (Non-Uniform Memory Access) effects. On recent hardware, we found that the code can run efficiently on nodes of at most 16-18 CPUs; on bigger nodes the NUMA effects are responsible for a slow-down of the code. OpenMP being a directive-oriented programming model, the implementation is almost transparent. The drawback is that the code cannot run on multiple nodes, so that the enormous resources provided by supercomputers are underused.

Numerical solvers and schemes: For our simulations we used both the Roe hydrodynamic solver and the HLLMHD magnetohydrodynamic solver, together with the MSRad radiative transport scheme (see following paragraphs for a more detailed description of the Roe, HLL-MHD and MSRad schemes). Both (M-)HD solvers use finite volume methods, meaning that the Gauss theo-

rem is applied in order to evaluate divergences as surface integrals, so that the relevant physical quantities are handled as fluxes through cell boundaries and these methods are conservative. For our runs we used a directional operator splitting scheme, reducing the 3D problem to a sequence of one-dimensional sweeps. Other non-split schemes are available as well. We also used in all of our runs the Hancock time integration scheme, so that terms in second order in time are approximated by a Hancock predictor step. The various operators ((M-)HD, RT, tensor viscosity) are separated by using operator splitting.

The Roe and the HLLMHD solvers: The Roe solver is described in Roe (1986). The solver used in CO<sup>5</sup>BOLD is however a modified version of it. It is an approximate 1D Riemann solver of Roe type that accounts for a realistic equation of state, a non-equidistant grid (even though all of our models are equidistant), and the presence of source terms due to the gravity field. The main characteristic of the implementation of the HLL solver in CO<sup>5</sup>BOLD is its ability to both ensure positivity of the gas pressure and use a constrained transport method that guarantees that  $\nabla \cdot \mathbf{B}$  is kept constant up to quantization (round-off) errors. For  $\nabla \cdot \mathbf{B}$ , no error arises from the discretization. The HLL scheme is described in Harten et al. (1983), and its specific implementation to the CO<sup>5</sup>BOLD code is described by Schaffenberger et al. (2005, 2006).

The MSrad radiative transport scheme: The MSrad RT scheme uses long characteristics to solve the RT equation with the Feautrier method for each opacity band, assuming Local Thermodynamic Equilibrium (LTE). The implementation of the Feautrier method in CO<sup>5</sup>BOLD is described by Freytag et al. (2012). The relevant quantity that the RT module should provide to the MHD module is the divergence of the radiative flux, see Eq. (2.1). In CO<sup>5</sup>BOLD, the exchanged quantities between the two modules is the heat source due to radiation,

$$Q_{\text{rad}} \equiv -\nabla \cdot \mathbf{F}_{\text{rad}}$$

$$\stackrel{(2.2)}{=} - \int_{\nu} \int_{\mathcal{S}^{2}} (\hat{\mathbf{n}} \cdot \nabla) I_{\nu}(\vec{\Omega}) d\Omega d\nu$$

$$\stackrel{(2.3)}{=} \int_{\nu} \rho \kappa_{\nu} \int_{\mathcal{S}^{2}} \left( I_{\nu}(\vec{\Omega}) - S_{\nu} \right) d\Omega d\nu$$

$$= \int_{\nu} 4\pi \rho \kappa_{\nu} (J_{\nu} - S_{\nu}) d\nu,$$
(2.5)

where  $J_{\nu}$  has been defined by the solid angle averaged mean intensity,

$$J_{\nu} \equiv \frac{1}{4\pi} \int_{S^2} I_{\nu}(\vec{\Omega}) \, d\Omega. \tag{2.6}$$

The main numerical difficulty comes from the fact that the simulated region encompasses the transition between optically thin and optically thick medium. Indeed, determining first  $\mathbf{F}_{\mathrm{rad}}$  and then numerically computing the divergence is not suitable in optically thin media where the radiative flux stays almost constant from cell to cell. Instead, computing  $J_{\nu} - S_{\nu}$  in order to use Eq. (2.5) is numerically unstable in extremely thick medium, where  $J_{\nu}$  is almost equal to the source function. Besides, this method does not necessarily guarantee conservation of energy, in the sense that the difference between the total flux at the top of the box and the total flux at the bottom of the box is not guaranteed to be equal to the integrated  $Q_{\rm rad}$  over the whole box. The MSrad RT scheme overcomes both of these problems by solving the RT equation using its own implementation of the Feautrier method with long characteristics for the new variable  $p_{\nu}(\vec{\Omega}) \equiv \frac{1}{2} \left( I_{\nu}(+\vec{\Omega}) + I_{\nu}(-\vec{\Omega}) \right) - S_{\nu}$ . Here, the index  $\nu$  does not refer any more to a specific frequency, but to a given opacity band, as discussed at the end of Sect. 2.1.2. The RT equation is hence solved for all bands along straight long rays (characteristics) crossing the computational box from top to bottom, at different azimuthal and inclination angles. Integrals over the sphere are numerically performed using a Lobatto quadrature, see Sect. 2.B.2.

#### 2.1.5 The numerical simulation runs

A number of numerical simulation runs are used throughout the projects of the following chapters. We describe here the models we synthesized ourselves by using the (magneto-)hydrodynamic CO<sup>5</sup>BOLD code with a variety of initial and boundary conditions.

The naming of the CO<sup>5</sup>BOLD models usually follows a precise pattern. All of our models are of the form "d3gt57g44....fc", in which "d3" stands for "three-dimensional model", "g" stands for the spectral type of the simulated star, G for the sun, "t57" is the truncated effective temperature of the star and it stands here for all temperatures in the range  $5700\,\mathrm{K} \leq T < 5800\,\mathrm{K}$ , "g44" is ten times the logarithm in base 10 of the surface gravity in cgs units, truncated to the two first digits, here we have the solar value  $g=10^{4.44}\,\mathrm{m\,s^{-2}}$ , the "...." give information on the initial/boundary conditions, and the last two letters are the initials of the person who ran the model.

All of our models have an equidistant grid spacing of  $10 \times 10 \times 10 \,\mathrm{km^3}$  and 960 grid cells, which represent a total size of  $9.6 \times 9.6 \times 2.8 \,\mathrm{Mm^3}$ . They were all computed with five opacity bands and the MSrad radiative transfer scheme was used. The boundary conditions on the sides are periodic, and the hydrodynamic boundary conditions at the top of the box are transmitting where as they are open in the bottom of the box. In the following we specify the (magneto-)hydrodynamic solver, and the initial and the boundary conditions for the magnetic field, for each model:

Run	Cell size [km <sup>3</sup> ]	Box size [Mm <sup>3</sup> ]	Height range [km]	$n_{ m opbds}$	$t_{ m run}$
d3gt57g44v50fc	$10\times10\times10$	$9.6\times9.6\times2.8$	-1240 < z < 1560	5	2.1 h
$\rm d3gt57g44v200fc$	$10\times10\times10$	$9.6\times9.6\times2.8$	-1240 < z < 1560	5	$3.6\mathrm{h}$
$\rm d3gt57g44p200fc$	$10\times10\times10$	$9.6\times9.6\times2.8$	-1240 < z < 1560	5	$0.6\mathrm{h}$
$\rm d3gt57g44h50vfc$	$10\times10\times10$	$9.6\times9.6\times2.8$	-1240 < z < 1560	5	$4.1\mathrm{h}$
$\rm d3gt57g44h50mfc$	$10\times10\times10$	$9.6\times9.6\times2.8$	-1240 < z < 1560	5	$4.1\mathrm{h}$
$\rm d3gt57g44b0fc$	$10\times10\times10$	$9.6\times9.6\times2.8$	-1240 < z < 1560	5	$6.0\mathrm{h}$
d3gt57g44roefc	$10\times10\times10$	$9.6\times9.6\times2.8$	-1240 < z < 1560	5	$6.9\mathrm{h}$
d3t57g44b0bfn025	$7 \times 7 \times 7$	$5.6 \times 5.6 \times 2.8$	-2540 < z < 260	1	1.5 h
$\rm d3gt57g44v50os$	$40\times40\times20-50$	$9.6\times9.6\times2.8$	-1425 < z < 1340	2	$1.7\mathrm{h}$
$\rm d3gt57g44h50os$	$40\times40\times20-50$	$9.6\times9.6\times2.8$	-1425 < z < 1340	2	$3.3\mathrm{h}$
$\rm d3gt57g44v50rs$	$14\times14\times12$	$5.6\times5.6\times2.256$	-1362 < z < 894	2	$11.1\mathrm{h}$
$\rm d3gt57g44v100rs$	$14\times14\times12$	$5.6\times5.6\times2.256$	-1362 < z < 894	2	$11.1\mathrm{h}$

**Table 2.1.** Box and cell sizes, number of opacity bands,  $n_{\text{opbds}}$ , and run duration,  $t_{\text{run}}$ , for all simulation runs considered in the following projects.

**Notes.** z = 0 refers to the mean optical depth one. The models d3gt57g44v50os and d3gt57g44h50os have a non-uniform grid-spacing in the vertical direction.

d3gt57g44v50fc (v50): the HLLMHD solver was used, with an initial vertical and homogeneous magnetic field of 50 G; vertical magnetic field was enforced in the top and bottom of the box.

d3gt57g44v200fc (v200): same as v50, but with an initial vertical and homogeneous magnetic field of 200 G.

d3gt57g44p200fc (p200): the HLLMHD solver was used, the magnetic field is enforced to be vertical in the bottom boundary and in downflow regions of the upper boundary, and it is constantly extrapolated in upflow regions of the upper boundary. The initial configuration of the magnetic field is described later in Sect. 3.6.2.

d3gt57g44h50vfc (h50v): the HLLMHD solver is used, the initial magnetic field is zero everywhere, it is enforced to be vertical in the top boundary, and it is advected into the box with the incoming plasma through the bottom boundary

d3gt57g44h50mfc (h50m): same as the h50v model, but in upflow regions of the top boundary the magnetic field is instead constantly extrapolated

d3gt57g44b0fc (B0): the HLLMHD solver is used and the magnetic field is everywhere zero

d3gt57g44roefc (Roe<sub>10</sub>): the Roe solver is used and there is no magnetic field

All of our simulation runs provide, at least, one full output of the box every 4 min and one output file with averaged quantities and emerging intensity maps for each opacity band every 30 s.

In addition to our own numerical simulations, we have used data from the following simulations:

d3t57g44b0bfn025 (Roe<sub>7</sub>): this non-magnetic model is described in Freytag (2013). The Roe solver was used.

d3gt57g44v50os and d3gt57g44h50os: these models are described in Steiner & Rezaei (2012).

d3gt57g44v50rs and d3gt57g44v100rs: these models are described in Salhab et al. (2018).

The main characteristics of all the simulation runs we used are summarized in Table 2.1.

#### 2.2 The physics of the polarized continuum

In a general enough framework, there is no clear distinction between "continuum" and "spectral lines" for the description of radiation-matter interactions. Since we will adhere to the formalism of Landi Degl'Innocenti & Landolfi (2004) for the rest of this thesis, we will introduce it here and we will clarify the concepts of "continuum" and "non-resonant scattering" in this general framework.

## 2.2.1 Scattering processes in the context of the formalism of Landi Degl'Innocenti & Landolfi

Landi Degl'Innocenti & Landolfi (2004) start from first principles to develop a formalism for the modelling of spectral lines in (mainly) stellar atmospheres, including both intensity and polarization. The starting point is quantum electrodynamics (QED). Successive derivations with appropriate approximations lead to the statistical equilibrium equations, describing how the radiations field modifies the state of the atomic system, and to the radiative transfer equations, describing how the atomic system affects the radiation field.

In the context of QED, the unperturbed Hamiltonians for matter and radiation are derived, as well as an interaction Hamiltonian. A first approximation is made by assuming the interaction Hamiltonian to be non-relativistic, which

is a reasonable assumption for the solar atmosphere, since the energy of photons  $(h\nu)$  is much smaller than the energy of the interacting particles. The equations of motion of any observable O with quantum operator  $\hat{O}$  and with a given density matrix of the system  $\rho$  are derived:

$$O(t) = \operatorname{Tr}\left\{\hat{O}\rho\right\} \implies \frac{\mathrm{d}}{\mathrm{d}t}O(t) = \operatorname{Tr}\left\{\frac{\mathrm{d}\hat{O}}{\mathrm{d}t}\rho\right\} + \operatorname{Tr}\left\{\hat{O}\frac{\mathrm{d}\rho}{\mathrm{d}t}\right\}.$$
 (2.7)

The density matrix is introduced to account for the effects of the coherence properties of the incident light, and is required for the description of polarized light. The total Hamiltonian then enters into the previous equation through the time evolution of the density operator in the Schrödinger representation.

$$\frac{\mathrm{d}}{\mathrm{d}t}\rho = \frac{2\pi}{\mathrm{i}h} \left[ H, \rho \right]. \tag{2.8}$$

Formally, the density matrix at time t can be written as

$$\rho(t) = \rho(t_0) + \frac{1}{i\hbar} \int_{t_0}^t [H(t'), \rho(t')] dt', \qquad (2.9)$$

but this alone is not helpful, since the density matrix at time t now depends on the same density matrix at all times previous to t. The crucial assumption done in the formalism of Landi Degl'Innocenti & Landolfi (2004) is that the total density matrix can be factorized as the direct product of the density matrices of each of the two systems,

$$\rho(t) \simeq \rho^{(R)}(t) \otimes \rho^{(A)}(t), \tag{2.10}$$

where  $\rho^{(R)}$  and  $\rho^{(A)}$  respectively refer to the density matrix of the radiation and atomic system. This is equivalent to assuming that the density functions of the radiation field and of the atomic system are uncorrelated. It is a reasonable assumption at time  $t=t_0$ , just before the interaction. However, here it is assumed to be still valid during and after the interaction. A different approach is to recursively insert the left hand side of the previous equation into the integral on the right hand side,

$$\rho(t) = \sum_{n=1}^{\infty} \frac{1}{(i\hbar)^n} \int_{t_0}^t dt_n \int_{t_0}^{t_n} dt_{n-1} \cdots \int_{t_0}^{t_2} dt_1 \times [H(t_n), [H(t_{n-1}), \cdots [H(t_1), \rho(t_0)] \cdots]], \quad (2.11)$$

and using Eq. (2.10) only then, for  $t = t_0$ . Each substitution in the recursion will provide higher-order contributions to the equations. In fact, the evolution

operator U of the density matrix, defined by

$$\rho(t) = U(t, t_0)\rho(t_0)U^{\dagger}(t, t_0), \tag{2.12}$$

can be expanded into a sum in which each term is represented by a Feynman diagram. First-order terms are single absorptions and emissions. Scattering events appear only as second-order terms. Using (2.10) directly into (2.9) leads to the lowest-order approximation to the equation of motion, which is expected to be valid whenever the relaxation time of the density matrix is longer than the time-scale over which the observables vary. In the presence of high collisional rates, the atomic system "forgets" the state of the absorbed photon before a new photon is re-emitted (the atomic system is thermalized), in which case the out-going radiation is a black-body radiation without polarization. When collisions are less frequent, the *flat spectrum approximation*, states that the radiation field has no structure in a spectral range of the order of the difference in energy between magnetic sub-levels between which coherence is taken into account. This approximation appears later as necessary to maintain consistency with the lowest-order approximation of the equation of motion. The flat-spectrum approximation is known in the context of unpolarized radiative transfer as the *complete redistribution* approximation.

There are a few consequences to these successive approximations. One of these is the absence of memory of scattered photons regarding the state of the incoming photons. This is often not a problem in the context of resonant scattering, i.e. when the frequency of the incoming photon is close to a resonant frequency of the atomic system. Instead, the contribution to the far wings of lines, corresponding to non-resonant coherent scattering (Rayleigh scattering), is missing in this formalism. It would appear only when considering the next-to-lowest-order contribution to the equations of motion, as shown by Bommier (1997) in a similar framework but not relying on the same approximations, or by Loudon (1973) in a framework disregarding coherence properties of the incident light. For the scattering of light from a weak incident beam by a two-level atom, neglecting collisional broadening and in the dipole approximation (requiring incident photons to have a wavelength significantly larger than the size of the atomic system), the total cross-section is given by

$$\sigma(\nu) = \sigma_{\rm T} f \frac{\nu^4}{(\nu^2 - \nu_0^2)^2 + 4\Gamma^2 \nu^2}, \tag{2.13}$$

where f and  $\nu_0$  are respectively the oscillator strength and the resonant frequency of the transition and  $\Gamma = \gamma/(4\pi)$ ,  $\gamma$  being the damping coefficient, corresponding to the inverse lifetime of the transition. The Thomson cross-section  $\sigma_T$  is defined by

$$\sigma_{\rm T} = \frac{8\pi}{3} \frac{e_0^4}{m^2 c^4}.\tag{2.14}$$

The total cross-section (2.13) can be found as a special case of the Kramers-Heisenberg formula, which is obtained when 2nd-order processes are taken into account. It was derived from quantum-mechanical grounds by Loudon (1973) in Sect. 8.8, and with modern formalism in Sect. 15.2 of Landi Degl'Innocenti (2014). It can also be found in Sect. 4.5 of Mihalas (1978), where it is derived from classical grounds. Instead, we shall see that with the formalism of Landi Degl'Innocenti & Landolfi (2004), a calculation of the cross-section for a 1st-order process from a J=0 level to a J=1 level in a two-level atom will give the result

$$\sigma(\nu) = \sigma_{\rm T} f \frac{3mc^3}{8e^2} \phi(\nu - \nu_0), \tag{2.15}$$

where  $\phi(\nu - \nu_0)$  should be the delta distribution  $\delta(\nu - \nu_0)$ , as a consequence of the 1st-order approach. It is however replaced, in a phenomenological way, by the Lorentz line profile

$$\phi(\nu - \nu_0) = \frac{1}{\pi} \frac{\Gamma}{(\nu - \nu_0)^2 + \Gamma^2}.$$
 (2.16)

It is straight forward to check that in the limit  $\nu \approx \nu_0$ , the two expressions (2.13) and (2.15) are the same, which confirms that the formalism is appropriate for modelling the core of spectral line. Far from the resonant frequency (in the wings of extended lines), the cross-section (2.15) drops quickly to zero. In the limit  $\nu \ll \nu_0$ , Eq. (2.13) has however a non-zero contribution,

$$\sigma_{\rm R}(\nu) = \sigma_{\rm T} f \frac{\nu^4}{(\nu^2 - \nu_0^2)^2},$$
(2.17)

which is known as Rayleigh scattering. In the limit  $\nu \gg \nu_0$ , the cross-section becomes independent of the frequency  $\nu$ , with a constant value of  $\sigma_T f$ . For transitions taking place from the ground level of Hydrogen (the most abundant element),  $\nu_0$  is already located in the ultra-violet, so that this limit does not concern optical wavelengths for the spectral lines of the Lyman series. At optical wavelengths Rayleigh scattering is in fact dominated by the red wings of the Lyman series lines, and the blue wings of spectral lines of the Balmer (and further) series play a negligible role.

Besides Rayleigh scattering of light at atomic systems, the scattering of light at free electrons is also taken into account, in the limit of low energy of the incoming photon (elastic limit), which is valid in solar atmospheric conditions. The cross-section of the interaction is the Thomson cross-section  $\sigma_{\rm T}$ , which value is derived classically in Loudon (1973) and corresponds to the limit in which f=1,  $\Gamma=0$  and  $\nu_0=0$  in Eq. (2.13).

Both Rayleigh and Thomson scattering are included in the formalism of Landi Degl'Innocenti & Landolfi (2004) as an additional "continuum" contri-

bution in the propagation matrix to the already-present coefficients arising from the core of spectral lines. Here we are solely concerned about this ad-hoc "continuum" contribution, but since the present formalism also uses a powerful language and tools that are very well suited in a broader context, we will adopt it here. In particular, the classical description of Rayleigh and Thomson scattering of polarized light requires, in addition to the scattering cross-section, a geometrical scattering matrix describing how polarized light redistributes among the polarization components after a scattering event. Interestingly, the corresponding classical equations reformulated within the formalism of Landi Degl'Innocenti & Landolfi (2004) are identical to the general 1st-order equations of statistical equilibrium specialized to the two-level atom with a 0-1 transition, but with a well-chosen cross-section, either the one of Eq. (2.17) for Rayleigh scattering or the Thomson cross-section. These scattering processes are conveniently borrowed from a second-order formalism and added into the first-order formalism a posteriori, providing a flexible and much simpler framework than any possible higher-order framework. Hence, between resonant and non-resonant scattering there is a purely formal distinction. As we shall see (and expect), this distinction is not always clearly revealed in the modelled spectrum, since many spectral lines can be crowded in such a way that these two regions totally overlap, as it is the case in the UV spectrum of the Sun.

#### 2.2.2 Non-scattering processes

The distinction between scattering processes (typically the processes responsible for the formation of spectral lines in non-local thermodynamic equilibrium) and non-scattering processes is also, to some extent, arbitrary (see the discussion of Mihalas 1978, in Sect. 2.1). By non-scattering processes, we mean absorption of photons followed by collisions, in such a way that the system has (some) time to thermalize before the emission of a new photon. Under the assumption that collisions are frequent enough, such processes are reasonably treated under local thermodynamical equilibrium (LTE) conditions.

This category hence includes all processes that we decide to treat in local thermodynamic equilibrium (LTE); these could include bound-bound transitions (ie. spectral lines), free-free transitions in the presence of an electric field (ie. inverse bremsstrahlung, in the vicinity of an atom or ion) or bound-free transitions (i.e. photoionizations).

#### 2.2.3 The emergence of linear polarization

Linear polarization in the continuum is closely related to coherent scattering. In this paragraph we aim at giving an intuitive picture; the formal mathematical picture is given in the next section.

The plasma in the solar atmosphere is in a good approximation locally

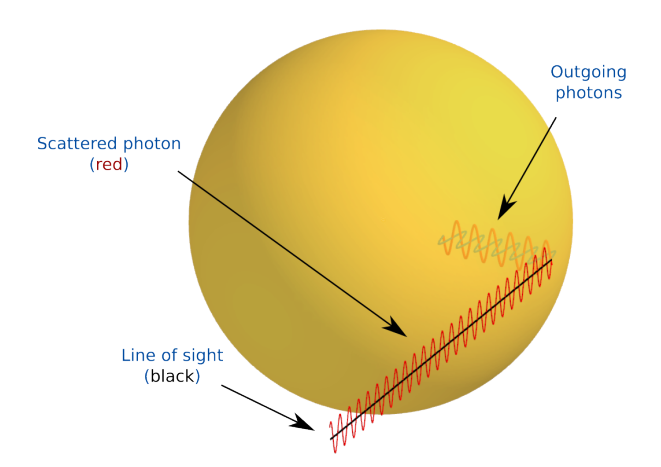


**Figure 2.1.** Two photons travelling radially out of the Sun interact with matter. Only the one which is perpendicularly polarized with respect to the line of sight is scattered in that direction.

homogeneous and isotropic. If a volume element of it was illuminated by unpolarized, isotropic radiation, the scattered light would stay unpolarized, and the black-body radiation due to LTE processes would also be isotropic and unpolarized. Linear polarization is introduced through scattering processes when the incoming radiation is not isotropic. Once these two ingredients are present (scattering and anisotropic radiation), many other factors can modulate the linearly polarized light, but scattering processes and anisotropy of the incoming radiation are sine qua non conditions for polarized radiation in the continuum. In the context of stellar atmospheres, the temperature gradient is responsible for anisotropic radiation (most radiation is directed outwards, from hotter layers to cooler ones), which leads to both emergence of linear polarization and limb darkening.

The vertical temperature gradient in the solar atmosphere is responsible for an anisotropic radiation field, which is at the origin of the limb-darkening effect, and it also breaks cylindrical symmetry along a line-of-sight, away from disc centre. The emergence of polarized light from unpolarized radiation after a (coherent) scattering event is illustrated on Fig. 2.1. The figure displays one single scattering event, but it properly illustrates the situation, since statistically most of the radiation travels radially out of the Sun, mainly perpendicularly to the line-of-sight when the observer points at the limb, and breaking the cylindrical symmetry in that direction. In the figure, the observer sees polarization along an axis parallel to the limb because that is the only axis along which the scattering centre must oscillate after absorbing a photon that travels radially out. Instead, if he was pointing to the disc centre, the argument would not hold. Indeed, in that case there would be a cylindrically symmetric

distribution of incoming photons travelling towards the scattering centre, and no preferred direction.

#### 2.2.4 Radiation-matter interactions

Here we list radiation-matter interactions involved in the formation of the continuum under solar conditions and at optical wavelengths. Such a list can also be found in Sect. 14.6 of Landi Degl'Innocenti (2014); we repeat it here with some additional comments. Since the most abundant element in the photosphere is hydrogen, we expect it to be involved in a number of the following processes. Indeed, the non-scattering contributions are:

- Photoionization of the negative hydrogen ion:  $H^- + h\nu \to H + e^-$ . This is the most important contribution to the non-scattering absorption coefficient at optical wavelengths,
- Photoionization of the hydrogen atom:  $H + h\nu \rightarrow H^+ + e^-$ ,
- Inverse bremsstrahlung near a hydrogen atom:  $H^+ + e^- + h\nu \rightarrow H^+ + e^-$ ,
- Inverse bremsstrahlung near a negative hydrogen ion:  $H^+ + 2e^- + h\nu \rightarrow H^+ + 2e^-$ ,
- Photoionizations of metals (other elements than Hydrogen)
- Photoionizations of the Hydroxide and the carbon-hydrogen molecules,
- $\bullet$  Inverse bremsstrahlung near the  $H_2^+$  and  $H_2^-$  molecules,

and the scattering contributions are:

- Rayleigh scattering at neutral hydrogen,
- Rayleigh scattering at neutral helium,
- Rayleigh scattering at metals,
- Thomson scattering at free electrons,
- Rayleigh scattering at molecular hydrogen.

The continuum intensity forms at a depth that justifies the assumption of LTE for the non-scattering contributions. Hence, we treat only the coherent scattering in nLTE. It should however be noted that the populations of the elements responsible for coherent scattering are set to the LTE populations by using the Boltzmann distribution.

# 2.3 Polarized radiative transport in the continuum

In this section we couple the general statistical equilibrium equations to the radiative transfer equations, making the relevant simplifications for the transport of light at optical wavelengths in the continuous spectrum.

#### 2.3.1 Simplifications and approximations

As stated in the previous section, we assume all populations to be given in LTE, we also assume LTE conditions for non-scattering contributions, and we formally treat coherent scattering contributions as emerging from 0-1 transitions. In addition, we assume that the magnetic field does not play any role in the solar continuum. In particular, the Hanle effect vanishes in the far wings of spectral lines (Rayleigh scattering), as shown in the context of the present formalism in Sect. 10.4 of Landi Degl'Innocenti & Landolfi (2004). An intuitive way of understanding this consists in pointing that, in a coherent scattering processes, the magnetic field has no time to depolarize the atomic system.

Dichroism and anomalous dispersion (see Eq. (2.37)) are also neglected. In an isotropic plasma they are absent. However, the lower level of an atomic bound-free transition can harbour polarization. Since, in the visible, the major contribution to photoionization processes is H<sup>-</sup> and its only bound state, having J=0, cannot be polarized. Furthermore, the only sublevel of the Hydrogen n=2 level that can harbour polarization,  $P_{3/2}$ , is very weakly populated. Neglecting dichroism and anomalous dispersion is hence justified.

Finally, stimulated emission is also neglected. This is justified since, according to Eq. (2.38),

$$\frac{\eta_i^{\rm S}}{\eta_i^{\rm A}} \sim \frac{\rho_0^0(\alpha_u J_u)}{\rho_0^0(\alpha_\ell J_\ell)} \ll 1. \tag{2.18}$$

## 2.3.2 Derivation of the equations for the polarized transport of light in the continuum

The radiative transfer equations are given in Eq. (8.2) of Landi Degl'Innocenti & Landolfi (2004) and repeated in Eq. (2.36) of Appendix 2.A.1. A specialization of these equations for the polarized transport of light in the continuum is found in Trujillo Bueno & Shchukina (2009). We give here a detailed derivation of it. Owing to the absence of dichroism and anomalous dispersion, the radiative transfer equation (2.36) decouples:

$$\frac{\mathrm{d}}{\mathrm{d}s}I(s) = -\eta_I(s)I(s) + \varepsilon_I(s),$$

$$\frac{\mathrm{d}}{\mathrm{d}s}Q(s) = -\eta_I(s)Q(s) + \varepsilon_Q(s),$$

$$\frac{\mathrm{d}}{\mathrm{d}s}U(s) = -\eta_I(s)U(s) + \varepsilon_U(s). \tag{2.19}$$

We do not make any assumption for V, but we omit to write the corresponding equations and we shall see later that this quantity always stays zero. The radiative transfer equations are rewritten after a change of variable:

$$\frac{\mathrm{d}}{\mathrm{d}\tau}I = I - S_I,\tag{2.20}$$

and similarly for Q and U. We have defined the optical depth and the source functions to be

$$d\tau \equiv -\eta_I ds, \quad S_I \equiv \frac{\varepsilon_I}{\eta_I}, \quad S_Q \equiv \frac{\varepsilon_Q}{\eta_I}, \quad S_U \equiv \frac{\varepsilon_U}{\eta_I}.$$
 (2.21)

We now differentiate emission and absorption for scattering and non-scattering processes, which we will label, respectively, as  $\varepsilon_i^{\rm s}$  and  $\eta_i^{\rm s}$  for scattering processes, and  $\varepsilon_i^{\rm ns}$  and  $\eta_i^{\rm ns}$  for non-scattering processes. The index i now stands for I, Q, U, V, or equivalently for 0, 1, 2, 3. For non-scattering processes under LTE conditions, we define the non-scattering source function:

$$S_i^{ns} \equiv \frac{\varepsilon_i^{\text{ns}}}{\eta_0^{\text{ns}}} = B_{\nu}(T). \tag{2.22}$$

The total source function can then be rewritten as

$$S_{i} \equiv \frac{\varepsilon_{i}^{\text{ns}} + \varepsilon_{i}^{\text{s}}}{\eta_{0}^{\text{ns}} + \eta_{0}^{\text{s}}} = \frac{\eta_{0}^{\text{ns}}}{\eta_{0}^{\text{ns}} + \eta_{0}^{\text{s}}} B_{\nu}(T) + \frac{\varepsilon_{i}^{\text{s}}}{\eta_{0}^{\text{ns}} + \eta_{0}^{\text{s}}}$$
$$= \frac{\eta_{0}^{\text{ns}}}{\eta_{0}^{\text{ns}} + \eta_{0}^{\text{s}}} B_{\nu}(T) + \frac{\eta_{0}^{\text{s}}}{\eta_{0}^{\text{ns}} + \eta_{0}^{\text{s}}} S_{i}^{s}, \tag{2.23}$$

in which we have also defined the source function for scattering processes

$$S_i^s \equiv \frac{\varepsilon_i^s}{\eta_0^s}.\tag{2.24}$$

The non-scattering absorption coefficient in LTE conditions is simply given by adding contributions from all species,

$$\eta_0^{\rm ns}(\nu) = \sum_j \mathcal{N}_j \sigma_j(\nu), \qquad (2.25)$$

where  $\mathcal{N}_j$  is the density of the j-th specie and  $\sigma_j$  is the corresponding cross-section.

The calculation of the scattering emission and absorption coefficients are more involved since they require nLTE calculations. For notational simplicity we drop the index s, and henceforth all emission and absorption coefficients

refer to coherent scattering. As discussed in Sect. 2.2.1, the formalism of Landi Degl'Innocenti & Landolfi (2004) is inappropriate for the description of coherent scattering. However, Thomson scattering can be accurately treated classically, and Rayleigh scattering primarily emerges from 0-1 transitions in the Hydrogen atom, for which quantum and classical computations describe the same scattering physics. With our approach we disregard the limitations of the formalism, and for this reason the final justification of these calculations resides in the fact that the emerging equations are compatible with the (classical) scattering physics of Chandrasekhar (1960). The cross-sections need to be appropriately substituted as discussed in Sect. 2.2.1. Our starting point is Eq. (2.38) in Appendix 2.A.2. We specialize it for a two-level atom and introduce the symbol  $w_{J_uJ_\ell}^{(K)}$  of Eq. (2.46), obtaining the absorption and emission coefficients

$$\eta_{i}^{A}(\nu,\vec{\Omega}) = \frac{h\nu}{4\pi} \mathcal{N} \left(2J_{\ell} + 1\right) B\left(\alpha_{\ell}J_{\ell} \to \alpha_{u}J_{u}\right) \\
\times \sum_{KQ} \frac{\left(-1\right)^{K} w_{J_{\ell}J_{u}}^{(K)}}{\sqrt{2J_{\ell} + 1}} \mathcal{T}_{Q}^{K}(i,\vec{\Omega}) \rho_{Q}^{K}(\alpha_{\ell}J_{\ell}) \\
\times \phi(\nu_{0} - \nu), \\
\eta_{i}^{S}(\nu,\vec{\Omega}) = \frac{h\nu}{4\pi} \mathcal{N} \left(2J_{u} + 1\right) B\left(\alpha_{u}J_{u} \to \alpha_{\ell}J_{\ell}\right) \\
\times \sum_{KQ} \frac{w_{J_{u}J_{\ell}}^{(K)}}{\sqrt{2J_{u} + 1}} \mathcal{T}_{Q}^{K}(i,\vec{\Omega}) \rho_{Q}^{K}(\alpha_{u}J_{u}) \\
\times \phi(\nu_{0} - \nu), \\
\varepsilon_{i}(\nu,\vec{\Omega}) = \frac{2h\nu^{3}}{c^{2}} \eta_{i}^{S}(\nu,\vec{\Omega}). \tag{2.26}$$

For a J=1 level, the only components of the spherical tensors that enter the computations are those with K=0, 1, 2 and  $Q=-K, \ldots, K$ . Since  $w_{J_{\ell}=0; J_{u}=1}^{(K)} = \delta_{K0}$ , one then finds by using the Einstein coefficients of Appendix 2.A.4 in Eq. (2.43):

$$S_{i} \equiv \frac{\varepsilon_{i}}{\eta_{0}} = \frac{2h\nu^{3}}{c^{2}} \sqrt{\frac{2J_{\ell} + 1}{2J_{u} + 1}} \sum_{KQ} (-1)^{K} w_{J_{u}J_{\ell}}^{(K)} \mathcal{T}_{Q}^{K}(i, \vec{\Omega}) \frac{\rho_{Q}^{K}(\alpha_{u}J_{u})}{\rho_{0}^{0}(\alpha_{\ell}J_{\ell})}$$
$$= \sum_{KQ} (-1)^{K} w_{J_{u}J_{\ell}}^{(K)} \mathcal{T}_{Q}^{K}(i, \vec{\Omega}) S_{Q}^{K}, \tag{2.27}$$

in which we have defined

$$S_Q^K \equiv \frac{2h\nu^3}{c^2} \sqrt{\frac{2J_\ell + 1}{2J_u + 1}} \frac{\rho_Q^K(\alpha_u J_u)}{\rho_0^0(\alpha_\ell J_\ell)}.$$
 (2.28)

By using Eq. (2.47) of Appendix 2.A.4 we deduce the following relation for  $S_O^K$ :

$$S_Q^K = w_{J_u J_\ell}^{(K)} (-1)^Q J_{-Q}^K (\nu_0) = w_{J_u J_\ell}^{(K)} J_Q^K (\nu_0)^*.$$
 (2.29)

Denoting real parts of complex quantities with a tilde and imaginary parts with a hat, we can further simplify the expression of the source function by using the symmetric properties of Eqs. (2.39) and (2.40) for the radiation field tensor and the density matrix:

$$S_{i} = \sum_{KQ} (-1)^{K} w_{J_{u}J_{\ell}}^{(K)} \mathcal{T}_{Q}^{K}(i,\vec{\Omega}) S_{Q}^{K}$$

$$= w_{J_{u}J_{\ell}}^{(0)} \mathcal{T}_{0}^{0}(i,\vec{\Omega}) S_{0}^{0} + w_{J_{u}J_{\ell}}^{(2)} \mathcal{T}_{0}^{2}(i,\vec{\Omega}) S_{0}^{2}$$

$$+ 2w_{J_{u}J_{\ell}}^{(2)} \sum_{Q>0} \left( \tilde{\mathcal{T}}_{Q}^{2}(i,\vec{\Omega}) \tilde{S}_{Q}^{2} + \hat{\mathcal{T}}_{Q}^{2}(i,\vec{\Omega}) \tilde{S}_{Q}^{2} \right)$$

$$+ w_{J_{u}J_{\ell}}^{(1)} \left( \mathcal{T}_{0}^{1}(i,\vec{\Omega}) S_{0}^{1} + 2 \left( \tilde{\mathcal{T}}_{1}^{1}(i,\vec{\Omega}) \tilde{S}_{1}^{1} + \hat{\mathcal{T}}_{1}^{1}(i,\vec{\Omega}) \tilde{S}_{1}^{1} \right) \right)$$

$$= \left( w_{J_{u}J_{\ell}}^{(0)} \right)^{2} \mathcal{T}_{0}^{0}(i,\vec{\Omega}) J_{0}^{0} + \left( w_{J_{u}J_{\ell}}^{(2)} \right)^{2} \mathcal{T}_{0}^{2}(i,\vec{\Omega}) J_{0}^{2}$$

$$+ 2 \left( w_{J_{u}J_{\ell}}^{(2)} \right)^{2} \sum_{Q>0} \left( \tilde{\mathcal{T}}_{Q}^{2}(i,\vec{\Omega}) \tilde{J}_{Q}^{2} - \hat{\mathcal{T}}_{Q}^{2}(i,\vec{\Omega}) \tilde{J}_{Q}^{2} \right)$$

$$+ \left( w_{J_{u}J_{\ell}}^{(1)} \right)^{2} \left( \mathcal{T}_{0}^{1}(i,\vec{\Omega}) J_{0}^{1} + 2 \left( \tilde{\mathcal{T}}_{1}^{1}(i,\vec{\Omega}) \tilde{J}_{1}^{1} + \hat{\mathcal{T}}_{1}^{1}(i,\vec{\Omega}) \hat{J}_{1}^{1} \right) \right). \tag{2.30}$$

The relevant non-zero components of the tensor  $\mathcal{T}_Q^K$  are:

$$\mathcal{T}_{0}^{2}(0,\vec{\Omega}) = \frac{1}{2\sqrt{2}} \left( 3\cos^{2}(\theta) - 1 \right) = \frac{1}{2\sqrt{2}} \left( 3\mu^{2} - 1 \right), 
\mathcal{T}_{1}^{2}(0,\vec{\Omega}) = -\frac{\sqrt{3}}{2} \sin(\theta) \cos(\theta) \exp(i\chi) = -\frac{\sqrt{3}}{2} \mu \sqrt{1 - \mu^{2}} \exp(i\chi), 
\mathcal{T}_{2}^{2}(0,\vec{\Omega}) = \frac{\sqrt{3}}{4} \sin^{2}(\theta) \exp(2i\chi) = \frac{\sqrt{3}}{4} \left( 1 - \mu^{2} \right) \exp(2i\chi), 
\mathcal{T}_{0}^{2}(1,\vec{\Omega}) = -\frac{3}{2\sqrt{2}} \sin^{2}(\theta) = -\frac{3}{2\sqrt{2}} \left( 1 - \mu^{2} \right), 
\mathcal{T}_{1}^{2}(1,\vec{\Omega}) = -\frac{\sqrt{3}}{2} \sin(\theta) \cos(\theta) \exp(i\chi) = -\frac{\sqrt{3}}{2} \mu \sqrt{1 - \mu^{2}} \exp(i\chi), 
\mathcal{T}_{2}^{2}(1,\vec{\Omega}) = -\frac{\sqrt{3}}{4} \left( 1 + \cos^{2}(\theta) \right) \exp(2i\chi) = -\frac{\sqrt{3}}{4} \left( 1 + \mu^{2} \right) \exp(2i\chi), \quad (2.31)$$

where we have chosen the reference frame with  $\gamma=0$  so that the Stokes U components vanish (after averaging over  $\chi$ , if the medium has an overall cylindrical symmetry) and Q is negative for linear polarization parallel to the limb (with the usual convention that Q is positive when linear polarization is parallel to the limb). Now we set  $J_{\ell}=0$  and  $J_{u}=1$ , for which  $w_{J_{u}J_{\ell}}^{(0)}=w_{J_{u}J_{\ell}}^{(2)}=1$ . As it will be shown below, we can assume the components  $J_{Q}^{1}$  of the radiation field tensor to be zero. We then get the scattering contribution to the source function:

$$S_{I}^{s} = J_{0}^{0} + \frac{1}{2\sqrt{2}} \left(3\mu^{2} - 1\right) J_{0}^{2} - \sqrt{3}\mu\sqrt{1 - \mu^{2}} \left(\cos\left(\chi\right) \tilde{J}_{1}^{2} + \sin\left(\chi\right) \hat{J}_{1}^{2}\right)$$

$$+ \frac{\sqrt{3}}{2} \left(1 - \mu^{2}\right) \left(\cos\left(2\chi\right) \tilde{J}_{2}^{2} + \sin\left(2\chi\right) \hat{J}_{2}^{2}\right)$$

$$S_{Q}^{s} = \frac{3}{2\sqrt{2}} \left(\mu^{2} - 1\right) J_{0}^{2} - \sqrt{3}\mu\sqrt{1 - \mu^{2}} \left(\cos\left(\chi\right) \tilde{J}_{1}^{2} + \sin\left(\chi\right) \hat{J}_{1}^{2}\right)$$

$$- \frac{\sqrt{3}}{2} \left(1 + \mu^{2}\right) \left(\cos\left(2\chi\right) \tilde{J}_{2}^{2} + \sin\left(2\chi\right) \hat{J}_{2}^{2}\right),$$

$$S_{U}^{s} = \sqrt{3}\sqrt{1 - \mu^{2}} \left(\sin\left(\chi\right) \tilde{J}_{1}^{2} + \cos\left(\chi\right) \hat{J}_{1}^{2}\right) + \sqrt{3}\mu \left(\sin\left(2\chi\right) \tilde{J}_{2}^{2} + \cos\left(2\chi\right) \hat{J}_{2}^{2}\right)$$

$$(2.32)$$

We can now rewrite the total source function of Eq. (2.23) in terms of scattering and non-scattering contributions:

$$S_{I} = \frac{\eta_{I}^{ns}}{\eta_{I}^{ns} + \eta_{I}^{s}} B_{\nu}(T) + \frac{\eta_{I}^{s}}{\eta_{I}^{ns} + \eta_{I}^{s}} \left[ J_{0}^{0} + \frac{1}{2\sqrt{2}} \left( 3\mu^{2} - 1 \right) J_{0}^{2} - \sqrt{3}\mu\sqrt{1 - \mu^{2}} \left( \cos\left(\chi\right) \tilde{J}_{1}^{2} + \sin\left(\chi\right) \hat{J}_{1}^{2} \right) + \frac{\sqrt{3}}{2} \left( 1 - \mu^{2} \right) \left( \cos\left(2\chi\right) \tilde{J}_{2}^{2} + \sin\left(2\chi\right) \hat{J}_{2}^{2} \right) \right],$$

$$S_{Q} = \frac{\eta_{I}^{s}}{\eta_{I}^{ns} + \eta_{I}^{s}} \left[ \frac{3}{2\sqrt{2}} \left( \mu^{2} - 1 \right) J_{0}^{2} - \sqrt{3}\mu\sqrt{1 - \mu^{2}} \left( \cos\left(\chi\right) \tilde{J}_{1}^{2} + \sin\left(\chi\right) \hat{J}_{1}^{2} \right) - \frac{\sqrt{3}}{2} \left( 1 + \mu^{2} \right) \left( \cos\left(2\chi\right) \tilde{J}_{2}^{2} + \sin\left(2\chi\right) \hat{J}_{2}^{2} \right) \right],$$

$$S_{U} = \frac{\eta_{I}^{s}}{\eta_{I}^{ns} + \eta_{I}^{s}} \left[ \sqrt{3}\sqrt{1 - \mu^{2}} \left( \sin\left(\chi\right) \tilde{J}_{1}^{2} + \cos\left(\chi\right) \hat{J}_{1}^{2} \right) + \sqrt{3}\mu \left( \sin\left(2\chi\right) \tilde{J}_{2}^{2} + \cos\left(2\chi\right) \hat{J}_{2}^{2} \right) \right]. \tag{2.33}$$

In the context of the continuum spectrum, these are referred as the *statistical* equilibrium equations. They were initially derived in Eq. (5) of Trujillo Bueno & Shchukina (2009). We note that the correct operand between the trigonometric

functions in the equation for Stokes U is the sum (there was a typographic error in the cited reference). The description of the polarized continuum spectrum is then completed with the addition of the radiative transfer equations

$$\frac{\mathrm{d}}{\mathrm{d}\tau}I = I - S_I,$$

$$\frac{\mathrm{d}}{\mathrm{d}\tau}Q = Q - S_Q,$$

$$\frac{\mathrm{d}}{\mathrm{d}\tau}U = U - S_U.$$
(2.34)

and by Eq. (2.42) expressing the radiation field tensor in terms of the Stokes parameters. By inserting the components of the tensor  $\mathcal{T}_Q^K$  into Eq. (2.42) we find

$$J_{0}^{0} = \oint \frac{d\Omega}{4\pi} I_{\nu\vec{\Omega}},$$

$$J_{0}^{2} = \oint \frac{d\Omega}{4\pi} \frac{1}{2\sqrt{2}} \left[ \left( 3\mu^{2} - 1 \right) I_{\nu\vec{\Omega}} + 3 \left( \mu^{2} - 1 \right) Q_{\nu\vec{\Omega}} \right],$$

$$J_{1}^{2} = \oint \frac{d\Omega}{4\pi} \frac{\sqrt{3}}{2} \sqrt{1 - \mu^{2}} \exp\left( i\chi \right) \left[ -\mu \left( I_{\nu\vec{\Omega}} + Q_{\nu\vec{\Omega}} \right) - iU_{\nu\vec{\Omega}} \right],$$

$$J_{2}^{2} = \oint \frac{d\Omega}{4\pi} \frac{\sqrt{3}}{4} \exp\left( 2i\chi \right) \left[ \left( 1 - \mu^{2} \right) I_{\nu\vec{\Omega}} - \left( 1 + \mu^{2} \right) Q_{\nu\vec{\Omega}} - 2i\mu U_{\nu\vec{\Omega}} \right]. \quad (2.35)$$

We now need to justify the assumption that the components  $J_Q^1$  of the radiation field tensor are zero, and show that V=0. Strictly speaking, we should show that the non-linear system of Eqs. (2.33), (2.34) and (2.35) without the assumption  $J_Q^1=0$  and completed with the corresponding equations for V admit one single solution in which V=0 and  $J_Q^1=0$  for all possible boundary conditions that can be found in the solar plasma.

We will tackle an easier problem, and assume here the existence of a unique solution to the coupled equations, as well as periodic boundary conditions in the horizontal planes. In the bottom layer, radiation is assumed to be unpolarized (V=0). The component  $\mathcal{T}_Q^1\left(i,\vec{\Omega}\right)$  is non-zero only when i=2, so that the product  $\mathcal{T}_Q^1\left(i,\vec{\Omega}\right)S_i\left(\nu,\vec{\Omega}\right)$  of Eq. (2.42) is zero whenever Stokes  $V=S_2=0$ , which is the case at the bottom boundary. Then  $J_Q^1=0$  and the source function  $S_V$  is also zero at the bottom boundary, according to the statistical equilibrium equation (2.30). The radiative transfer equation (2.34) guarantees that the boundary condition V=0 is transported to the next layers, in which, for the same reason,  $S_V$  is again zero, and hence also V=0 on the next layer. This is of course not a formal proof, but it outlines the idea of a proof.

In order to solve the coupled system of non-linear Eqs. (2.33), (2.34)

and (2.35), we wrote the *Polarized RAdiative Transfer In the Continuum* (PRATIC) module for the *Polarized Radiative TrAnsfer* (PORTA) code of Štěpán & Trujillo Bueno (2013).

#### 2.A Details on the formalism of Landi Degl'Innocenti & Landolfi (2004)

In the following appendix, equations of the book of Landi Degl'Innocenti & Landolfi (2004) will be labelled with the additional prefix "LL04-".

#### 2.A.1 Radiative transfer equation for polarized radiation

The radiative transfer equation for polarized radiation is given by Eq. (LL04-8.2):

$$\frac{\mathrm{d}}{\mathrm{d}s}I(s) = -K(s)I(s) + \varepsilon(s), \tag{2.36}$$

where s is the coordinate along the line of sight,  $\varepsilon$  is the emissivity vector, and the propagation matrix K is given in Eqs. (LL04-8.3) and (LL04-5.27):

$$K = \underbrace{\begin{pmatrix} \eta_{I} & 0 & 0 & 0 \\ 0 & \eta_{I} & 0 & 0 \\ 0 & 0 & \eta_{I} & 0 \\ 0 & 0 & 0 & \eta_{I} \end{pmatrix}}_{\text{Absorption}} + \underbrace{\begin{pmatrix} 0 & \eta_{Q} & \eta_{U} & \eta_{V} \\ \eta_{Q} & 0 & 0 & 0 \\ \eta_{U} & 0 & 0 & 0 \\ \eta_{V} & 0 & 0 & 0 \end{pmatrix}}_{\text{Dichroism}} + \underbrace{\begin{pmatrix} 0 & 0 & 0 & 0 \\ 0 & 0 & \rho_{V} & -\rho_{U} \\ 0 & -\rho_{V} & 0 & \rho_{Q} \\ 0 & \rho_{U} & -\rho_{Q} & 0 \end{pmatrix}}_{\text{Anomalous dispersion}}. (2.37)$$

The components of the absorption matrix and of the emissivity are called the radiative transfer coefficients.

#### 2.A.2 Radiative transfer coefficients

Each coefficient of the propagation matrix is a sum of two contributions, one due to absorption and the other due to stimulated emission (taken as negative, so that in this notation  $\eta_I = \eta_I^{\text{A}} - \eta_I^{\text{S}}$ ). These contributions are explicitly stated in Eq. (LL04-7.16) for a multi-level atom, where i = 0, 1, 2, 3 correspond to

I, Q, U, V:

$$\eta_{i}^{A}(\nu,\vec{\Omega}) = \frac{h\nu}{4\pi} \mathcal{N} \sum_{\alpha_{\ell}J_{\ell}} \sum_{\alpha_{u}J_{u}} (2J_{\ell} + 1) B \left(\alpha_{\ell}J_{\ell} \rightarrow \alpha_{u}J_{u}\right) \\
\times \sum_{KQ} \sqrt{3} \left(-1\right)^{1+J_{\ell}+J_{u}+K} \left\{ \begin{array}{cc} 1 & 1 & K \\ J_{\ell} & J_{\ell} & J_{u} \end{array} \right\} \mathcal{T}_{Q}^{K}(i,\vec{\Omega}) \rho_{Q}^{K}(\alpha_{\ell}J_{\ell}) \\
\times \phi(\nu_{\alpha_{u}J_{u},\alpha_{\ell}J_{\ell}} - \nu), \\
\eta_{i}^{S}(\nu,\vec{\Omega}) = \frac{h\nu}{4\pi} \mathcal{N} \sum_{\alpha_{\ell}J_{\ell}} \sum_{\alpha_{u}J_{u}} (2J_{u} + 1) B \left(\alpha_{u}J_{u} \rightarrow \alpha_{\ell}J_{\ell}\right) \\
\times \sum_{KQ} \sqrt{3} \left(-1\right)^{1+J_{\ell}+J_{u}} \left\{ \begin{array}{cc} 1 & 1 & K \\ J_{u} & J_{u} & J_{\ell} \end{array} \right\} \mathcal{T}_{Q}^{K}(i,\vec{\Omega}) \rho_{Q}^{K}(\alpha_{u}J_{u}) \\
\times \phi(\nu_{\alpha_{u}J_{u},\alpha_{\ell}J_{\ell}} - \nu), \\
\rho_{i}^{A}(\nu,\vec{\Omega}) = \eta_{i}^{A}(\nu,\vec{\Omega}) \left\{ \phi(\nu_{\alpha_{u}J_{u},\alpha_{\ell}J_{\ell}} - \nu) \rightarrow \psi(\nu_{\alpha_{u}J_{u},\alpha_{\ell}J_{\ell}} - \nu) \right\}, \\
\rho_{i}^{S}(\nu,\vec{\Omega}) = \eta_{i}^{S}(\nu,\vec{\Omega}) \left\{ \phi(\nu_{\alpha_{u}J_{u},\alpha_{\ell}J_{\ell}} - \nu) \rightarrow \psi(\nu_{\alpha_{u}J_{u},\alpha_{\ell}J_{\ell}} - \nu) \right\}, \\
\varepsilon_{i}(\nu,\vec{\Omega}) = \frac{2h\nu^{3}}{c^{2}} \eta_{i}^{S}(\nu,\vec{\Omega}). \tag{2.38}$$

The two profiles  $\phi$  and  $\psi$  are defined in Eq. (LL04-6.59a).  $\rho_Q^K$  are the multipole moments of the atomic density matrix that appears in Eq. (LL04-3.101) and it satisfies the symmetry relation given in Table LL04-3.6:

$$\rho_{-Q}^{K}(\alpha J) = (-1)^{Q} \rho_{Q}^{K}(\alpha J)^{*}. \tag{2.39}$$

 $\mathcal{T}_Q^K$  is a spherical tensor whose components are listed in Table LL04-5.6, together with an analogous symmetry relation

$$\mathcal{T}_{-Q}^{K}(i,\vec{\Omega}) = (-1)^{Q} \mathcal{T}_{Q}^{K}(i,\vec{\Omega})^{*}.$$
 (2.40)

Notice that such a relation also holds for the radiation field tensor, according to Table LL04-5.7:

$$J_{-Q}^{K}(\nu) = (-1)^{Q} J_{Q}^{K}(\nu)^{*}. \tag{2.41}$$

Moreover,  $B(\alpha_{\ell}J_{\ell} \to \alpha_{u}J_{u})$  and  $B(\alpha_{u}J_{u} \to \alpha_{\ell}J_{\ell})$  are the Einstein coefficients for absorption and stimulated emission, respectively. They are connected to the line strength in Eq. (LL04-7.7).

#### 2.A.3 The radiation field tensor

Eq. (2.41) relates the components of the radiation field tensor among each other. Those are defined from the Stokes vector  $S_i$  in Eq. (LL04-5.157):

$$J_Q^K(\nu) = \oint \frac{\mathrm{d}\Omega}{4\pi} \sum_{i=0}^3 \mathcal{T}_Q^K(i, \vec{\Omega}) S_i(\nu, \vec{\Omega}). \tag{2.42}$$

#### 2.A.4 Einstein coefficients

The Einstein coefficients are related to the line strength in Eq. (LL04-7.7). They are related to each other in Eq. LL04-(7.8):

$$A(\alpha_u J_u \to \alpha_\ell J_\ell) = \frac{2h}{c^2} \nu_{\alpha_u J_u, \alpha_\ell J_\ell}^3 B(\alpha_u J_u \to \alpha_\ell J_\ell),$$

$$(2J_\ell + 1) B(\alpha_\ell J_\ell \to \alpha_u J_u) = (2J_u + 1) B(\alpha_u J_u \to \alpha_\ell J_\ell)$$
(2.43)

#### 2.A.5 6-j symbols

The 6-j Symbols appear in the coupling of three angular momenta. The only property that we need here is:

$$\begin{cases} a & b & 0 \\ d & e & f \end{cases} = \delta_{ab}\delta_{ed} (-1)^{a+e+f} \frac{1}{\sqrt{(2a+1)(2d+1)}}, \tag{2.44}$$

which can be found in Eq. (LL04-2.36a).

#### 2.A.6 The density matrix

The density matrix provides a complete and compact description of the state of the atoms. This has to be calculated by solving the statistical equilibrium equations, which in general can only be done numerically. For the particular case of two-level atoms with unpolarized lower level, the statistical equilibrium equations can be solved analytically. In the absence of collisions, the spherical components of the statistical tensor of the upper level are given by Eq. (LL04-10.27),

$$\rho_{Q}^{K}(\alpha_{u}J_{u}) = \sqrt{\frac{2J_{\ell}+1}{2J_{u}+1}} \frac{B(\alpha_{\ell}J_{\ell} \to \alpha_{u}J_{u})}{A(\alpha_{u}J_{u} \to \alpha_{\ell}J_{\ell}) + 2\pi i \nu_{L} g_{\alpha_{u}J_{u}}Q} \times w_{J_{u}J_{\ell}}^{(K)}(-1)^{Q} J_{-Q}^{K}(\nu_{0}) \rho_{0}^{0}(\alpha_{\ell}J_{\ell}), \qquad (2.45)$$

where the symbols  $w_{J_uJ_\ell}^{(K)}$  are defined in Eqs. (LL04-10.11) and (LL04-10.12) by

$$w_{J_{u}J_{\ell}}^{(K)} \equiv \frac{\left\{\begin{array}{ccc} 1 & 1 & K \\ J_{u} & J_{u} & J_{\ell} \end{array}\right\}}{\left\{\begin{array}{ccc} 1 & 1 & 0 \\ J_{u} & J_{u} & J_{\ell} \end{array}\right\}} = (-1)^{1+J_{\ell}+J_{u}} \sqrt{3(2J_{u}+1)} \left\{\begin{array}{ccc} 1 & 1 & K \\ J_{u} & J_{u} & J_{\ell} \end{array}\right\}.$$

$$(2.46)$$

The last equality follows from Eq. (2.44). A list of values of this symbol may be found in Table LL04-10.1. If we neglect the Hanle contribution (the term  $2\pi i \nu_L g_{\alpha_u J_u} Q$  in the denominator of Eq. (2.45)), the expression simplifies further using Eq. (2.43):

$$\frac{\rho_Q^K(\alpha_u J_u)}{\rho_0^0 \left(\alpha_\ell J_\ell\right)} = \frac{c^2}{2h\nu_0^3} \sqrt{\frac{2J_u + 1}{2J_\ell + 1}} w_{J_u J_\ell}^{(K)} \left(-1\right)^Q J_{-Q}^K \left(\nu_0\right). \tag{2.47}$$

## 2.B Quadrature formulas for numerical integration on the sphere

The calculation of the spherical components of the radiation field tensor of Eq. (2.35) requires an integration over the sphere. To this aim, numerical integration schemes require a partition of the sphere into a finite set of regions, and a selection of corresponding directions (nodes). The integral is then approximated by the sum of the integrands over each chosen direction, pondered by the area of the corresponding region (the weight).

A given set of nodes with the corresponding weights is called a *quadrature* over the sphere. The accuracy of the quadrature depends on the problem. As a general rule, quadratures with a greater number of nodes will be more accurate, but they will also be computationally more expensive. The difficulty resides in choosing, for a specific problem, both a good thread-off between accuracy and computing time and an optimal quadrature for the given number of nodes.

Some of the quadratures listed below can be found in the chapter of numerical interpolation, differentiation, and integration in Abramowitz & Stegun (1964).

### 2.B.1 The product quadrature with Gauss-Legendre nodes

The product quadrature with Gauss-Legendre nodes is the traditional Gauss quadrature. The following discussion is base on the review of Atkinson (1982). If the integrand is expressed in spherical coordinates, this is the easiest quadrature, since the partition of the sphere is expressed as the Cartesian product of

partitions over the declination angle  $\theta$  and the azimuthal angle  $\phi$ :

$$I[f] \equiv \oint_{\mathbb{S}^2} f(\Omega) d\Omega$$

$$= \int_0^{2\pi} \int_0^{\pi} f(\theta, \phi) \sin(\theta) d\theta d\phi$$

$$\approx \sum_{j=0}^{2N_{\phi}} \sum_{i=1}^{N_{\theta}} w_i w_j f(\theta_i, \phi_j). \tag{2.48}$$

A convenient choice for the angles is  $\phi_j = \frac{j\pi}{N_{\phi}}$  and  $\mu_i \equiv \cos(\theta_i)$  the Gauss-Legendre nodes on [-1;1], with the corresponding weights

$$w_i = \frac{2}{(1 - \mu_i^2) P_n'(\mu_i)^2}, \quad w_j = \frac{\pi}{N_\phi}.$$
 (2.49)

This specific choice is optimized in such a way that polynomials of a given degree are integrated exactly with a minimal number of nodes. More precisely, for  $M \equiv N_{\phi} = N_{\theta}$ , polynomials of degree  $n \equiv 2M$  are solved exactly with a total of  $N \equiv 2M^2$  nodes, so that asymptotically  $n = \sqrt{2N} \sim \mathcal{O}\left(\sqrt{N}\right)$ .

#### 2.B.2 Lobatto's quadrature

This quadrature is similar to the previous one: it is also a product quadrature and hence the integral over the sphere also factorizes into an integral over the declination angles and an integral over the azimuthal angles. The azimuthal part stays identical, whereas on the declination part we add the vertical direction:

$$\int_{-1}^{1} f(\mu) d\mu \approx \frac{2}{n(n-1)} (f(1) + f(-1)) + \sum_{i=2}^{n-1} w_i f(\mu_i), \qquad (2.50)$$

with the weights given by

$$w_i = \frac{2}{n(n-1)P'_{n-1}(\mu_i)^2}. (2.51)$$

In some situations such as radiation transfer problems the vertical direction plays an important role. This quadrature is hence more appropriate in these cases.

#### 2.B.3 The double-Gauss quadrature

A different possible issue of the traditional Gauss quadrature with a small number of nodes, when applied to radiative transfer problems, is the sharp variation of intensity at inclined angles. A simple strategy consists in splitting the declination part of the integral into two parts,

$$\int_{-1}^{1} f(\mu) d\mu = \int_{0}^{1} f(+\mu) d\mu + \int_{0}^{1} f(-\mu) d\mu$$
$$= \frac{1}{2} \int_{-1}^{1} f\left(+\frac{\mu+1}{2}\right) d\mu + \frac{1}{2} \int_{-1}^{1} f\left(-\frac{1+\mu}{2}\right) d\mu, \qquad (2.52)$$

for which each part can now be approximated with the traditional Gauss quadrature. This quadrature was initially proposed and compared with other quadratures in Sykes (1951), within the context of transfer problems. At this point, a natural idea would be to additionally include the vertical direction to the double-Gauss quadrature, similarly as it was done with the Lobatto's quadrature, but we leave this idea for a future work.

#### 2.B.4 Lebedev's quadrature

Lebedev's quadratures are based on symmetry considerations. They are described in detail in Lebedev (1976). Since the Cartesian grid broadly used in numerical simulations has octahedral symmetry, the nodes of Lobatto's quadrature are chosen with exactly the same symmetry.

The considered symmetry group contains all transformations that map the origin-centred cube into itself (rotations by an angle multiple of  $\pi/2$ , reflections in the x-y, y-z and z-x planes, and all compositions of those transformations).

Lebedev's quadrature is no more a product quadrature. Nodes are now specified as pairs of declination and azimuthal angles,

$$I[f] \equiv \oint_{\mathbb{S}^2} f(\Omega) d\Omega$$

$$\approx \sum_{i}^{N} w_i f(\theta_i, \phi_i). \tag{2.53}$$

For a given order n of the method, there are in principle many possible quadratures with different values of N that have the proper symmetry. The ones that have the minimal N are called Lebedev's quadratures. For  $0 \le n \le 17$ , all possible quadratures with the appropriate symmetry are explicitly computed in Lebedev (1975). Lebedev's quadratures exist only for some values of N.

Number of nodes	$n_{ m Gauss-Legendre}$	$n_{ m Lebedev}$	$\eta_{ m Gauss-Legendre}$	$\eta_{ m Lebedev}$	
2	1	_	1.00	_	
6	_	3	_	0.89	
8	4	_	1.56	_	
14	_	5	_	0.86	
18	6	_	1.36	_	
26	_	7	_	0.82	
32	8	_	1.27	_	
38	_	9	_	0.87	
50	10	11	1.21	0.96	
4802	98	119	1.02	0.99	
:	:	:	:	:	
N	$\sqrt{2N}$	$\sqrt{3}N$	1	1	

**Table 2.2.** The quality is compared for quadratures with different number of nodes.

**Notes.** The quality should not be used to compare Lebedev's quadratures with Gauss-Legendre quadratures, but only quadratures of the same kind, but with different number of nodes, among each other.

The order n of Lebedev's quadratures is related to the number of nodes N,

$$N = \frac{1}{3} (n^2 + \mathcal{O}(n)), \qquad (2.54)$$

and hence the Lebedev quadratures are of order  $n \sim \sqrt{3N} \sim \mathcal{O}(\sqrt{N})$ . In order to compare Lebedev's quadratures among each other, the quality is defined as the number of Laplace spherical harmonics exactly integrable, divided by 3N (so that the quality asymptotes to 1),

$$\eta = \frac{(n+1)^2}{3N}. (2.55)$$

The quality can be defined in the same way for Gauss-Legendre quadratures, in which case the normalization is 2N. The quality is compared among quadratures with different number of nodes in Table 2.2. There are other means of comparing the quadratures. For instance, according to Lebedev (1976), the distribution of nodes in the sphere is very regular when  $n \equiv 5$  (12) and when  $n \equiv 11$  (12). In particular, the quadrature with N = 50 has both an excellent quality and a regular distribution of the nodes on the sphere.

Bibliography 35

#### **Bibliography**

Abramowitz, M. & Stegun, I. 1964, Handbook of Mathematical Functions: With Formulas, Graphs, and Mathematical Tables, Applied mathematics series (Dover Publications)

- Alfvén, H. 1946, "On the cosmogony of the solar system III", Stockholms Observatoriums Annaler, 14, 9.1
- Atkinson, K. 1982, "Numerical integration on the sphere", J. Austral. Math. Soc. (Series B.), 23, 332
- Auer, L. H., Heasley, J. N., & Milkey, R. W. 1972, "A computational program for the solution of non-LTE transfer problems by the complete linearization method", Contributions from the Kitt Peak National Observatory, 555
- Auer, L. H. & Mihalas, D. 1969, "Non-LTE Model Atmospheres. I. Radiative Equilibrium Models with Lyman-α", ApJ, 156, 157
- Bommier, V. 1997, "Master equation theory applied to the redistribution of polarized radiation, in the weak radiation field limit. I. Zero magnetic field case", A&A, **328**, 706
- Buscher, D. F., Baldwin, J. E., Warner, P. J., & Haniff, C. A. 1990, "Detection of a bright feature on the surface of Betelgeuse", MNRAS, **245**, 7P
- Carlsson, M. 1986, "A computer program for solving multi-level non-LTE radiative transferproblems in moving or static atmospheres.", Uppsala Astronomical Observatory Reports, 33
- Chandrasekhar, S. 1960, Radiative transfer (Dover Publications)
- Chiavassa, A., Pasquato, E., Jorissen, A., et al. 2011, "Radiative hydrodynamic simulations of red supergiant stars. III. Spectro-photocentric variability, photometric variability, and consequences on Gaia measurements", A&A, 528, A120 [arXiv:1012.5234]
- Feautrier, P. 1964, "A Method for Improving the T(x) Law", SAO Special Report, 167, 108
- Fontenla, J. M., Avrett, E. H., & Loeser, R. 1993, "Energy balance in the solar transition region. III - Helium emission in hydrostatic, constant-abundance models with diffusion", ApJ, 406, 319
- Freytag, B. 2013, "Advances in the hydrodynamics solver of CO5BOLD", Mem. S.A.It. Suppl., **24**, 26

Freytag, B., Steffen, M., & Dorch, B. 2002, "Spots on the surface of Betelgeuse – Results from new 3D stellar convection models", Astron. Nachr., 323, 213

- Freytag, B., Steffen, M., Ludwig, H.-G., et al. 2012, "Simulations of stellar convection with CO5BOLD", J. Comput. Phys., 231, 919 [arXiv:1110.6844]
- Freytag, B., Steffen, M., Wedemeyer-Böhm, S., et al. 2010, "CO5BOLD: COnservative COde for the COmputation of COmpressible COnvection in a BOx of L Dimensions with l=2,3", Astrophysics Source Code Library
- Gingerich, O., Noyes, R. W., Kalkofen, W., & Cuny, Y. 1971, "The Harvard-Smithsonian reference atmosphere", Sol. Phys., 18, 347
- Gustafsson, B., Edvardsson, B., Eriksson, K., et al. 2008, "A grid of MARCS model atmospheres for late-type stars. I. Methods and general properties", A&A, 486, 951 [arXiv:0805.0554]
- Harten, A., Lax, P. D., & van Leer, B. 1983, "On Upstream Differencing and Godunov-Type Schemes for Hyperbolic Conservation Laws", SIAM Rev., 25, 35
- Holweger, H. & Mueller, E. A. 1974, "The photospheric Barium spectrum
  Solar abundance and collision broadening of BA II lines by Hydrogen",
  Sol. Phys., 39, 19
- Landi Degl'Innocenti, E. 2014, Atomic Spectroscopy and Radiative Processes (Springer-Verlag)
- Landi Degl'Innocenti, E. & Landolfi, M. 2004, Astrophysics and Space Science Library, Vol. 307, *Polarization in Spectral Lines* (Kluwer Academic Publishers)
- Lebedev, V. 1975, "Values of the nodes and weights of ninth to seventeenth order gauss-markov quadrature formulae invariant under the octahedron group with inversion", Zh. vychisl. Mat. mat. Fiz., 15, 44
- Lebedev, V. 1976, "Quadratures on a sphere", Zh. vychisl. Mat. mat. Fiz., 16, 10
- Leboeuf, J. N., Tajima, T., Kennel, C. F., & Dawson, J. M. 1978, "Global simulation of the time-dependent magnetosphere", Geophys. Res. Lett., 5, 609
- Loudon, R. 1973, *The quantum theory of light*, 3rd edn. (Oxford University Press)
- Ludwig, H.-G. 1992, PhD thesis, University of Kiel

Bibliography 37

Ludwig, H.-G., Jordan, S., & Steffen, M. 1994, "Numerical simulations of convection at the surface of a ZZ Ceti white dwarf", A&A, 284, 105

- Ludwig, H.-G. & Steffen, M. 2013, "Opacities in CO $^5\!BOLD$ ", Mem. S.A.It. Suppl., **24**, 53
- Mihalas, D. 1978, *Stellar atmospheres*, 2nd edn., ed. G. Burbidge & M. Burbidge (H. W. Freeman and Company)
- Nordlund, Å. 1982, "Numerical simulations of the solar granulation. I Basic equations and methods", A&A, **107**, 1
- Nordlund, Å. 1983, "Numerical 3-D simulations of the collapse of photospheric flux tubes", in IAU Symposium, Vol. 102, Solar and Stellar Magnetic Fields: Origins and Coronal Effects, ed. J. O. Stenflo, 79–83
- Nordlund, Å. 1984, "Magnetoconvection: The interaction of convection and small scale magnetic fields", in ESA Special Publication, Vol. 220, ESA Special Publication, ed. P. Hoyng & M. Kuperus
- Nordlund, Å. 1985a, "Solar convection", Sol. Phys., 100, 209
- Nordlund, Å. 1985b, "The 3-D Structure of the Magnetic Field and its Interaction with Granulation", in *Theo. Prob. High Resolution Solar Physics*, ed. H. U. Schmidt, 101
- Nordlund, Å. 1986, "3-D Model Calculations", in Small Scale Magnetic Flux Concentrations in the Solar Photosphere, 83
- Paladini, C., Baron, F., Jorissen, A., et al. 2017, "Large granulation cells on the surface of the giant star  $\pi 1$  Gruis", Nature, **553**, 310
- Peckover, R. S. & Weiss, N. O. 1978, "On the dynamic interaction between magnetic fields and convection", MNRAS, 182, 189
- Riethmüller, T. L., Solanki, S. K., Barthol, P., et al. 2017, "A New MHD-assisted Stokes Inversion Technique", ApJS, 229, 16 [arXiv:1611.05175]
- Roe, P. L. 1986, "Characteristic-based schemes for the Euler equations", Ann. Rev. Fluid Mech., 18, 337
- Salhab, R., Steiner, O., Berdyugina, S., et al. 2018, "Simulation of the small-scale magnetism in main sequence stellar atmospheres (in press)", A&A
- Schaffenberger, W., Wedemeyer-Böhm, S., Steiner, O., & Freytag, B. 2005, "Magnetohydrodynamic Simulation from the Convection Zone to the Chromosphere", in ESA Special Publication, Vol. 596, Chromospheric and Coronal Magnetic Fields, 65.1

38 Bibliography

Schaffenberger, W., Wedemeyer-Böhm, S., Steiner, O., & Freytag, B. 2006, "Holistic MHD-Simulation from the Convection Zone to the Chromosphere", in ASP Conf. Ser., Vol. 354, Solar MHD Theory and Observations: A High Spatial Resolution Perspective, 345

- Shibata, K. 1983, "Nonlinear MHD wave propagation in the solar chromosphere. I The case of a uniform vertical magnetic field", PASJ, **35**, 263
- Stein, R. F. & Nordlund, Å. 2000, "Realistic Solar Convection Simulations", Sol. Phys., 192, 91
- Steiner, O. & Rezaei, R. 2012, "Recent Advances in the Exploration of the Small-Scale Structure of the Quiet Solar Atmosphere: Vortex Flows, the Horizontal Magnetic Field, and the Stokes- V Line-Ratio Method", in Astronomical Society of the Pacific Conference Series, Vol. 456, Fifth Hinode Science Meeting, ed. L. Golub, I. De Moortel, & T. Shimizu, 3
- Stenflo, J. O. 2011, "Magnetic fields on the quiet Sun", Central European Astrophysical Bulletin, **35**, 1
- Straus, T., Marconi, M., & Alcalà, J. M. 2017, "The third CO5BOLD workshop", Mem. S.A.It., 88, 5
- Sykes, J. B. 1951, "Approximate integration of the equation of transger", MN-RAS, 111, 377
- Trujillo Bueno, J. & Shchukina, N. 2009, "Three-dimensional Radiative Transfer Modeling of the Polarization of the Sun's Continuous Spectrum", ApJ, 694, 1364 [arXiv:0812.3494]
- Štěpán, J. & Trujillo Bueno, J. 2013, "PORTA: A three-dimensional multilevel radiative transfer code for modeling the intensity and polarization of spectral lines with massively parallel computers", A&A, 557, A143 [arXiv:1307.4217]
- Vögler, A. 2004, "Effects of non-grey radiative transfer on 3D simulations of solar magneto-convection", A&A, 421, 755
- Wittmann, A. 1972, "Magnetooptische Effekte in Fraunhoferlinien mit Zeeman-Aufspaltung", Mitteilungen der Astronomischen Gesellschaft Hamburg, **31**, 150

# Constraints on the magnetic field in numerical simulations

#### Contents

3.1	Overvi	iew	9
3.2	Constrained transport with the ${\rm CO^5BOLD}$ code		
3.3	Other	methods for ensuring $\nabla \mathbf{B} = 0$ 43	3
	3.3.1	Advection of magnetic monopoles 4	3
	3.3.2	Divergency cleaning	4
3.4	A code	e for divergency cleaning	4
	3.4.1	Magnetic monopoles associated to numerical errors 4	5
	3.4.2	The Hodge projection scheme	5
	3.4.3	Implementation of the BiCGSTAB method 4	6
	3.4.4	Boundary conditions and ghost cells 4	7
3.5	Magne	etic monopoles in CO <sup>5</sup> BOLD simulations 48	8
3.6	A pote	ential magnetic field	9
	3.6.1	General construction	9
	3.6.2	The p200 magnetic configuration 5	1
Bibl	iography	y	<b>2</b>

#### 3.1 Overview

An additional physical constraint to the MHD equations (2.1) is the divergencefree condition for the magnetic field.  $\nabla \cdot \mathbf{B} = 0$  is not an evolution equation, and is in principle not required since initial divergence-free fields are guaranteed to stay so by the induction equation, the third of the MHD Eqs. (2.1),

$$\frac{\partial \mathbf{B}}{\partial t} + \nabla \cdot (\mathbf{v}\mathbf{B} - \mathbf{B}\mathbf{v}) = 0, \tag{3.1}$$

as long as the boundary conditions also guarantee the divergence-free field condition. However, a discrete formulation of the induction equation must not necessarily fulfil this condition and solenoidality must be enforced, in addition to updating **B** according to the numerical scheme.

In addition, there are different ways of numerically discretizing the derivation operator, and for a given numerical scheme evolving the induction equation, the existence of a discretization that preserves  $\nabla \cdot \mathbf{B}$  in the course of the simulation is not guaranteed, and if such a discretization exists for that specific scheme, it will be the only one having that property. In practice, our concern is about spurious forces that might be introduced into the simulations because of non-vanishing magnetic field divergency, that would lead to unphysical magnetic monopoles and plasma acceleration parallel to the magnetic field lines.

To avoid this situation, we need to carefully choose an appropriate numerical method for evolving the induction equation, identify how derivatives should be discretized, and check if  $\nabla \cdot \mathbf{B}$  stays reasonably small (in principle exactly zero) with that specific discretization. Depending on the scheme and the type of grid, there are many different ways of achieving this, in some cases with a precision of the order of round-off errors, as is the case with the CO<sup>5</sup>BOLD code (Freytag et al. 2012). In this chapter we describe the technique used by CO<sup>5</sup>BOLD, and we empirically test its performance in maintaining  $\nabla \cdot \mathbf{B}$  low with some of our magnetic models. We also give a brief description of other techniques and present in detail a divergency-cleaning technique that we implemented in a computer code.

An additional issue arising in magnetic simulations is the initial condition for the magnetic field. The typical way of constructing high-resolution models is to start with a low-resolution hydrodynamic (non-magnetic) model, refine it and evolve it. After relaxation, a magnetic field is added into the box, and the new magnetic box is again evolved. The added magnetic field must also satisfy  $\nabla \cdot \mathbf{B} = 0$  in the sense of the previous paragraph. However, any such magnetic configuration will typically introduce a sudden additional Lorentz force, leading to potential numerical difficulties. A magnetic field that avoids sudden introduction of additional Lorentz forces is called a *force-free* field. A specific case of it is the *potential field*. In the second part of this chapter we present a possible construction of a general potential field, and present one of our models that was evolved with such an initial field.

## 3.2 Constrained transport with the CO<sup>5</sup>BOLD code

The HLLMHD solver implemented in CO<sup>5</sup>BOLD uses the constrainedtransport method of Evans & Hawley (1988) within a Godunov-type finitevolume scheme described in Freytag et al. (2012). The constrained transport method is based on a finite volume scheme, where the magnetic field is defined on computation cell (volume) faces and the electric current is defined on computational cell edges.

The idea behind this technique is to discretize scalar fields with cell-averages and vector fields as surface averages on the faces of the cells. We index cell boundaries with half-integer indices  $(i \pm 1/2, j \pm 1/2, k \pm 1/2)$  and cell-centres with integer indices (i, j, k) as depicted in Fig. 3.1. For the sake of simplicity, we will assume the grid to be equidistant. The average magnetic field over a cell surface can hence be written

$$\mathbf{B}_{i+\frac{1}{2},j,k} = \frac{1}{\Delta y \Delta z} \int_{z_{k-\frac{1}{2}}}^{z_{k+\frac{1}{2}}} \int_{y_{j-\frac{1}{2}}}^{y_{j+\frac{1}{2}}} \mathbf{B}(x,y,z) \, \mathrm{d}y \, \mathrm{d}z.$$
 (3.2)

In this example we have chosen a cell surface normal to the x axis the red

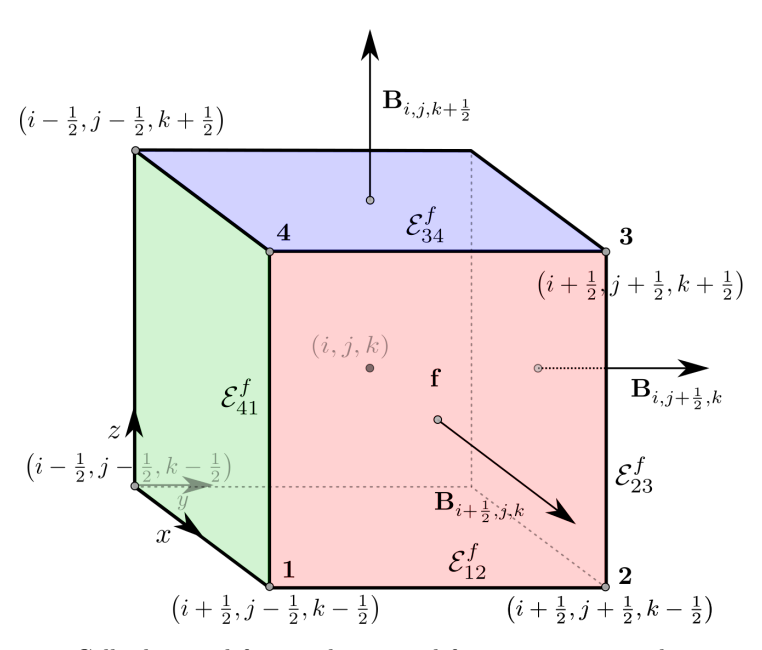


Figure 3.1. Cell edges and faces indexing and face-centre averaged magnetic field. The red face f has its edges labelled with the integers 1, 2, 3, 4 and the electro-motive between these edges is shown

surface in Fig. 3.1. With this method, we are actually discretizing the averaged magnetic flux densities instead of the magnetic field. In the limit of infinitely small cell-sizes, both quantities are however identical. The divergency free

condition can now be rewritten using the Gauss theorem:

$$\int_{z_{k-\frac{1}{2}}}^{z_{k+\frac{1}{2}}} \int_{y_{j-\frac{1}{2}}}^{y_{j+\frac{1}{2}}} \int_{x_{i-\frac{1}{2}}}^{x_{i+\frac{1}{2}}} \nabla \cdot \mathbf{B}(x, y, z) \, \mathrm{d}x \mathrm{d}y \mathrm{d}z = \oint_{\text{cell}} \mathbf{B}(x, y, z) \hat{\mathbf{n}} \, \mathrm{d}S, \qquad (3.3)$$

where the second integral is taken over the cell faces and "cell" designs the cell with centre i, j, k, and  $\hat{\mathbf{n}}$  is a unit vector normal to  $\mathrm{d}S$  and pointing out of the cell. Writing the components of the magnetic field  $\mathbf{B} = (B^x, B^y, B^z)$  we obtain

$$\oint_{\text{cell}} \mathbf{B}(x, y, z) \hat{\mathbf{n}} \, dS = \Delta y \Delta z \left( -B_{i - \frac{1}{2}, j, k}^x + B_{i + \frac{1}{2}, j, k}^x \right) 
+ \Delta x \Delta z \left( -B_{i, j - \frac{1}{2}, k}^y + B_{i, j + \frac{1}{2}, k}^y \right) 
+ \Delta x \Delta y \left( -B_{i, j, k - \frac{1}{2}}^z + B_{i, j, k + \frac{1}{2}}^z \right) 
= \sum_{\text{cell faces } f} \Phi_f,$$
(3.4)

where  $\Phi_f$  is the magnetic flux through each of the cell faces indexed by f. With this constrained transport method, the magnetic flux is evolved on cell faces, rather than evolving the magnetic field on discrete points. The magnetic flux is then evolved from the flux rule for motional electro-motive force (Faraday's law),

$$-\frac{d\Phi_f}{dt} = \mathcal{E}_{12}^f + \mathcal{E}_{23}^f + \mathcal{E}_{34}^f + \mathcal{E}_{41}^f, \tag{3.5}$$

in which the vertices of face f are labelled with integers 1, 2, 3, 4, and  $\mathcal{E}_{ij}^f$  is the emf from vertex i to vertex j. Fig. 3.1 shows these labels for the red face. If we now introduce the notation

$$\mathbf{B}_{i,j,k} = \frac{1}{\Delta x \Delta y \Delta z} \int_{z_{k-\frac{1}{2}}}^{z_{k+\frac{1}{2}}} \int_{y_{j-\frac{1}{2}}}^{y_{j+\frac{1}{2}}} \int_{x_{i-\frac{1}{2}}}^{x_{i+\frac{1}{2}}} \mathbf{B}(x,y,z) \, \mathrm{d}x \, \mathrm{d}y \, \mathrm{d}z, \tag{3.6}$$

we find from Eqs. (3.2) to (3.4)

$$\frac{\mathrm{d}}{\mathrm{d}t} \nabla \cdot \mathbf{B}_{i,j,k} = \frac{1}{\Delta x \Delta y \Delta z} \sum_{\text{cell faces } f} \frac{\mathrm{d}\Phi_f}{\mathrm{d}t}$$

$$= -\frac{1}{\Delta x \Delta y \Delta z} \sum_{\text{cell faces } f} \mathcal{E}_{12}^f + \mathcal{E}_{23}^f + \mathcal{E}_{34}^f + \mathcal{E}_{41}^f, \qquad (3.7)$$

which reduces to zero, since for each pair of vertices of a given cell, there are exactly two faces sharing the edge in between these vertices, with corresponding emf of opposite sign.

The present approach hence guarantees that the divergency of B will be

maintained constant in all cells up to round-off errors, that will add-up at each time step. It however does not guarantee that the divergency of B will be maintained zero up to round-off errors after an arbitrary number of time steps. If round-off errors were uniformly distributed on cells, uncorrelated from cell to cell and also independent from the previous and next time steps,  $\nabla \cdot B$  would be properly modelled by a random walk, and would hence grow as  $\sqrt{N}$ , with N the number of time steps performed.

## 3.3 Other methods for ensuring zero divergence of the magnetic field

There are a number of different methods to deal with the vanishing magnetic divergency requirement, and many different implementations. A detailed description of many of these methods, numerical tests, and performance analyses of them can be found in Tóth (2000). Further developments and newer methods can also be found in Christlieb et al. (2014). There is however no preferred method for all situations. The optimal method depends on many parameters: the problem to be solved, the regularity of the grid, the base scheme, the initial and boundary conditions of the problem, etc.

The constrained transport method used in CO<sup>5</sup>BOLD is a fast and accurate method, but the implementation can be more complicated as compared with other methods, especially when combined with adaptive mesh refinement techniques (which is not the case in CO<sup>5</sup>BOLD). A different but very attractive method is the central difference scheme of Tóth (2000). It is a simple finite-difference method, that also maintains the divergency of the magnetic field constant, but does not generalize to adaptive mesh refinement.

It is possible to picture the constrained transport and the central difference schemes as methods evolving an underlying vector potential (Tóth 2000), hence guaranteeing zero-divergence of the magnetic field. Actually some methods reformulate the MHD equation in terms of a vector potential, but then the base scheme is quite different from a field solver.

#### 3.3.1 Advection of magnetic monopoles

Another method to keep  $\nabla \cdot \mathbf{B}$  within bounds is the 8-wave scheme of Powell (1994), where a source term proportional to the divergence of  $\mathbf{B}$  is added to the MHD equations (this term naturally appears in the derivation of the MHD equations when one does not constrain  $\nabla \cdot \mathbf{B}$ ), making it non-conservative, but also generating an 8th wave to the equations. When the divergence of  $\mathbf{B}$  is exactly equal to zero, the usual MHD equations are found back. Instead, when small magnetic monopoles are generated by the numerical scheme, they are allowed to move, and eventually leave the box through the boundaries.

At the same time, the boundary conditions are formulated in a way that not magnetic monopoles can enter the computational domain from outside. A method with a similar mechanism for the evacuation of magnetic monopoles that is conservative and more effective is the hyperbolic cleaning of Dedner et al. (2002). In this method, a scalar field coupled to  $\nabla \cdot \mathbf{B}$  is added to the MHD equations in such a way that the magnetic monopoles are transported to the domain boundaries with the maximal admissible speed.

#### 3.3.2 Divergency cleaning

With all previous methods  $\nabla \cdot \mathbf{B}$  my become larger than admissible by the round-off precision, either because the divergence is allowed to grow at each step up to round-off errors, or because the divergence is tolerated to be non-zero in exchange of a continuous transport of magnetic monopoles outside of the box.

The divergency cleaning methods use yet another strategy, that guarantees the divergence of the magnetic field to be zero up to round-off errors at each step (or every few steps) by "cleaning" the magnetic field from its non-solenoidal part. We describe here a projection scheme that consists in rewriting the magnetic field as a sum of a gradient and a curl through the Hodge projection. The curl is retained as the divergency-free part of the magnetic field. The procedure is described e.g. in the lecture notes of Leveque (1998), and it is also revisited in Tóth (2000), addressing "many of the incorrect claims widespread about it". In particular, it is shown that the scheme can be conservative with an appropriate implementation, can be efficient (even though it is the least efficient method among those presented here), and flexible with respect to the grid geometry and boundary conditions. In an efficient implementation it is integrated in the base scheme, and no ad-hoc "cleaning" procedure is required.

#### 3.4 A code for divergency cleaning

For the purpose of preparing an initial magnetic field configuration, to compare the different numerical schemes, or simply to apply cleaning after a long time simulating, it is useful to have an independent solution for divergency cleaning available. To this aim, we use the projection scheme described in Tóth (2000). In order to solve the discretized Poisson equation, we implemented the *BiConjugate Gradient STABilized* method (BiCGSTAB) of Van der Vorst (1992), an iterative method for the solution of nonsymmetric linear systems.

#### 3.4.1 Magnetic monopoles associated to numerical errors

In analogy to the electric field case, we can define a "magnetic charge" of magnetic monopoles as

$$\rho_{\text{mon}} = \nabla \cdot \mathbf{B}^*, \tag{3.8}$$

and just as it is done for electric fields, we can invert the equation, finding

$$\mathbf{B}_{\mathrm{mon}}(r_0) = \frac{1}{4\pi} \int_{\mathbb{R}} \rho_{\mathrm{mon}} \frac{\mathbf{r}_0 - \mathbf{r}}{(r_0 - r)^3} d\tau = \frac{1}{4\pi} \int_{\mathbb{R}} \nabla \cdot \mathbf{B}^* \frac{\mathbf{r}_0 - \mathbf{r}}{(r_0 - r)^3} d\tau.$$
 (3.9)

A reasonable cleaning procedure would be to set

$$\mathbf{B} = \mathbf{B}^* - \mathbf{B}_{\text{mon}},\tag{3.10}$$

but then the difficulty of the problem still resides in the evaluation of the integral of Eq. (3.9) up to machine precision, with the appropriate boundary conditions. In this case the periodic boundary conditions in the horizontal directions complicate the problem even more.

Yet, this picture is still useful since it provides a natural and physically meaningful way of quantifying the numerical errors with the quantity

$$\mathcal{E}_{\text{mon}} = \frac{B_{\text{mon}}^2}{8\pi},\tag{3.11}$$

which is the energy density stored in the magnetic field generated by the monopoles. Since the total energy density is provided by internal, magnetic and kinetic energy density contributions

$$\mathcal{E}_{\text{tot}} = \mathcal{E}_{\text{int}} + \mathcal{E}_{\text{mag}} + \mathcal{E}_{\text{kin}},$$
 (3.12)

an indicator of accuracy loss due to a divergent magnetic field can be defined by the ratio

$$r \equiv \max_{\text{box}} \left( \frac{\mathcal{E}_{\text{mon}}}{\mathcal{E}_{\text{tot}}} \right) = \max_{\text{box}} \left( \frac{\mathcal{E}_{\text{mon}}}{\mathcal{E}_{\text{int}} + \mathcal{E}_{\text{mag}} + \mathcal{E}_{\text{kin}}} \right). \tag{3.13}$$

#### 3.4.2 The Hodge projection scheme

Let's assume a non-solenoidal magnetic field  $\mathbf{B}^*$  as typically produced by some numerical scheme. There is a unique decomposition of the field as a sum of a rotational and a gradient,

$$\mathbf{B}^* = \nabla \times \mathbf{A} + \nabla \phi, \tag{3.14}$$

even though **A** and  $\phi$  are not unique. Then the magnetic field due to the magnetic monopoles  $\mathbf{B}_{\text{mon}}$  of Eq. (3.9) is precisely given by  $\nabla \phi$ . Since the

divergence of the rotational is zero, an equation for  $\phi$  is easily obtained by taking the divergence of Eq. 3.14,

$$\nabla^2 \phi = \nabla \cdot \mathbf{B}^*, \tag{3.15}$$

and a "cleaned field" is given by

$$\mathbf{B} = \mathbf{B}^* - \nabla \phi. \tag{3.16}$$

Since  $\mathbf{B}^*$  is discretized at the centres of cell faces and the numerical divergence can be expressed as a first order finite difference calculation on the staggered grid shifted by half a cell in each direction (according to Eq. (3.4)), the scalar field  $\phi$  can be consistently defined by cell-centred values on the original grid, and the Laplace operator by second-order finite differences. Indeed, the first order differences over the scalar field  $\phi$  will give discrete values of  $\nabla \phi$  on cell-centres of the staggered mesh, in the same location where discretized magnetic field values are, and the second-order difference then also corresponds to the divergence operator of Eq. (3.4) applied on  $\nabla \phi$ . The consistent definition of the numerical Laplace operator as the composition of the numerical divergence operator used in the RHS of Eq. (3.15) with the numerical gradient operator used in the previous Eq. (3.16) is obviously critical in this algorithm.

#### 3.4.3 Implementation of the BiCGSTAB method

The BiCGSTAB method is designed for the solution of nonsymmetric linear systems, and the discretization of Eq. (3.15) provides indeed such a system of equations, that can in principle be written explicitly. For instance, the RHS of Eq. (3.15) would be explicitly written as the product of an  $N \times N$  sparse matrix with a one-dimensional vector of size N, where  $N = n_x \cdot n_y \cdot n_z$  is the size of the computational 3D box. The matrix-vector multiplication alone would involve  $\mathcal{O}(N^2)$  operations, and the majority of them would be simple multiplications by zero. This conceptual representation of the problem is interesting since it explicitly shows that the system is linear, but it is by no means an appropriate representation for the efficient solution of the system.

The evaluation of the underlying matrix-vector multiplication of the numerical Laplace operator is indeed required by the BiCGSTAB method, but it can also be done by applying the second order difference operator on each cell of the discretized scalar field. Similarly, the divergence operator will be done by applying Eq. (3.4) at each cell. So the numerical Laplace and divergence operators consist of a repeated operation applied on each cell of the domain, and this operation involves a number of neighbouring cells. The collection of the involved neighbours is pictured as a *stencil*. Applying a stencil on a cell involves a constant number of operations depending on the size of the stencil,

so that the whole evaluation requires only  $\mathcal{O}(N)$  operations.

We implemented the BiCGSTAB method in a very flexible and abstract way, allowing for any representation of the operator evaluation (explicit matrix multiplication, stencil operation), together with generic stencils. We compiled the code in a static library that we then linked with a python module we specifically wrote for the purpose of divergency cleaning. Both the BiCGSTAB library and the divergency cleaning python module are written in C99. The input magnetic field and the parameters for the BiCGSTAB library (boundary conditions, maximum number of iterations, etc.) are hence simply fed to the library from a python script or shell.

#### 3.4.4 Boundary conditions and ghost cells

The stencil method we described in the previous section for the evaluation of the Laplace operator works well when the stencil is fully within the computational domain. Near the boundaries, however, part of the stencil is out of the box. An equivalent way of depicting the problem is by pointing out that second order differences should be modified at the boundaries of the box according to the boundary conditions. A convenient way of proceeding is to add ghost cells around the computing box and set appropriate values to match the boundary conditions, keeping the very same stencil on the external shells of the computing box. This is exactly the approach we used.

This procedure then raises the question of which boundary conditions are appropriate for the problem of divergency cleaning. The natural answer is that the boundary conditions must reflect the boundary conditions for the magnetic field that was used for the simulation. Since we are imposing boundary conditions to the scalar field  $\phi$ , but only know the boundary conditions of  $\mathbf{B}^*$ , some care must be taken. To be consistent with Eq. (3.14), the boundary conditions of the scalar field  $\phi$  should be chosen so that the inherited boundary conditions of  $\nabla \phi$  match the boundary conditions of the divergent (non-solenoidal) part of  $\mathbf{B}^*$ . Along the horizontal x and y axes, the boundary conditions for  $\phi$  must simply be periodic, as are the corresponding conditions for  $\mathbf{B}^*$  in our simulations. Since with constrained transport methods the boundary conditions for  ${\bf B}^*$  are typically chosen so that the divergence vanishes on the boundaries,  $\phi$ should be set constant on these boundaries (then its gradient also vanishes), or simply zero. In the top and bottom boundaries the magnetic field is however recomputed to enforce  $\nabla \cdot \mathbf{B} = 0$ , so those boundary conditions are actually not so relevant there. Indeed, on each cell at the top and bottom boundary, there is one single face at the immediate boundary, on which the field is recomputed. In all other faces the field is kept constant.

## 3.5 Magnetic monopoles in CO<sup>5</sup>BOLD simulations

In this section we empirically test CO<sup>5</sup>BOLD's performance in maintaining  $\nabla \cdot \mathbf{B} = 0$ , for two of our simulation runs, d3gt57g44v50fc and d3gt57g44h50mfc, and for other longer simulations runs, d3gt57g44v50os, d3gt57g44v50rs and d3gt57g44v100rs. All of these models are described in Sect. 2.1.5.

Our strategy consists in computing the magnetic field of Eq. (3.9) associated to the magnetic monopoles by using the Hodge projection scheme of Sect. 3.4.2 with our implementation of the BiCGSTAB of Sect. 3.4.3. The energy associated to the magnetic monopoles is then defined in Eq. (3.11), and the performance of a scheme in maintaining  $\nabla \cdot \mathbf{B} = 0$  is estimated by the time evolution of the maximum value on the computing domain of the ratio of the magnetic monopole energy to the total energy, as defined in Eq. (3.13).

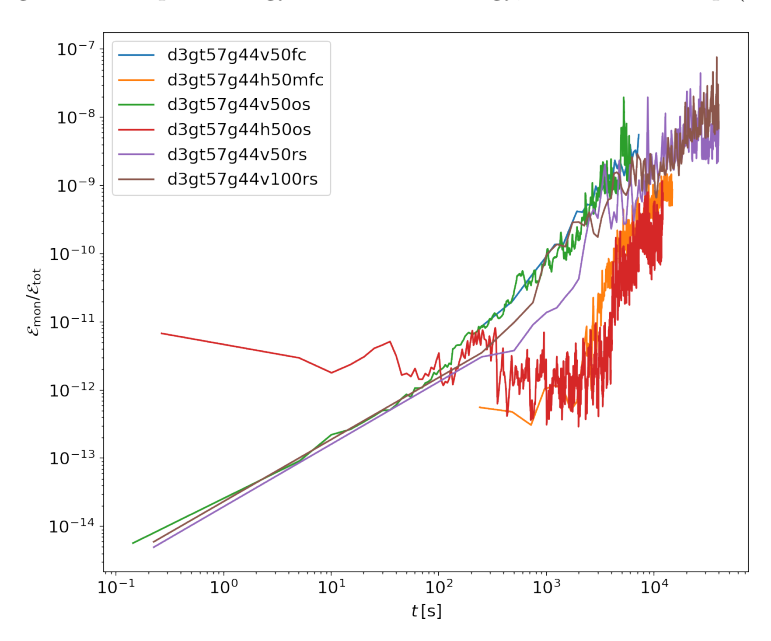


Figure 3.2. Maximum ratio of monopole energy to total energy over the computational domain, for different CO<sup>5</sup>BOLD simulations, as a function of time.

With a very rough order-of-magnitude analysis, we can estimate CO<sup>5</sup>BOLD's performance. Since CO<sup>5</sup>BOLD intrinsically avoids discretization errors in the magnetic field, only round-off errors are expected. We first assume that round-off errors on  $\nabla \cdot \mathbf{B}$  are uncorrelated, both spatially and in time. We also assume that they are given by a uniform and symmetric random distribution centred on zero. The total error at any timestep on  $\nabla \cdot \mathbf{B}$ 

is then the sum of all cumulated errors at all previous times, and it should behave as a random walk. Its standard deviation will then grow as  $\sqrt{t}$ . The monopole energy of Eq. (3.11) is then approximately expected to grow as t, i.e. as a power-law with parameter  $\alpha=1$ . Obviously, non of these assumptions is correct, but it is still reasonable to expect, in short time ranges, a power-law growth with some given parameter.

Fig. 3.2 displays the time evolution of the accuracy indicator we have defined in order to quantify  $CO^5BOLD$ 's performance in maintaining  $\nabla \cdot \mathbf{B} = 0$ . We must note that the models without magnetic field in the initial conditions, but with magnetic field advected by the plasma through the bottom boundary, have a peculiar behaviour. This is due to the fact that the numerical computation of the energy of the magnetic monopoles with the iterative BiCGSTAB scheme has also a numerical error, and in a box in which the magnetic field is still almost zero everywhere, there are also pixels with extremely low total energy. The ratio of magnetic monopole energy to total energy can hence give unpredictable results on those pixels. For this reason the models with advected magnetic field and no initial magnetic field in the box should only be considered after some significant amount of magnetic field is in the box.

From Fig. 3.2 we observe that the energy of the magnetic monopoles exhibit a growth that is reasonably similar to a power-law, with a parameter of about 2.4 for the models without advected field, and up to about 5 for the other models. In up to 11 h of simulation time, the maximum ratio of magnetic monopole energy to total energy stays reasonably small (below 10<sup>7</sup>), and exhibits no hint of an undesired exponential growth. By comparing the models with 50 G initial magnetic field with the one with 100 G initial magnetic field, we find no dependence on the initial strength of the field for the models starting with homogeneous vertically oriented magnetic field.

#### 3.6 A potential magnetic field

#### 3.6.1 General construction

As pointed out at the end of the Sec. 3.1, the introduction of a magnetic field in an initially magnetic field-free box constitutes a sudden perturbation of its dynamics, possibly leading to numerical complications. In order to minimize the impact, a force-free magnetic field should be chosen. A trivial example is an initially vertical magnetic field. During the relaxation phase, the magnetic field lines quickly concentrate in the intergranular lanes, and the field loses its force-free property. But at that point the field is already consistently evolving with the plasma and the inclusion of the field happens in a smooth way. The disadvantage of this method is that such a simple initial condition fails to reproduce realistic configurations. A different approach consists in advecting

an horizontal field with the plasma entering through the bottom boundary of the box as in Stein & Nordlund (2006) and in Steiner et al. (2008). This second approach is however slow, and the simulation has to evolve for a long time before significant magnetic field reaches the top layers of the box.

Here, we consider potential fields, which are more general configurations than simple vertical fields, but not yet general force-free fields. The Lorentz force is proportional to  $\mathbf{j} \times \mathbf{B}$ , and in a non-relativistic plasma the current density  $\mathbf{j}$  is given by  $\mathbf{j} = \nabla \times \mathbf{B}$ . A force-free magnetic field is then a divergenceless field for which  $\mathbf{j}$  is parallel to  $\mathbf{B}$ , and hence  $\nabla \times \mathbf{B} = \alpha \mathbf{B}$  for some scalar field  $\alpha$  constructed so that  $\nabla \cdot \mathbf{B} = 0$ . Such fields have been investigated by Taylor (1986), where it is shown that they describe a state of minimal energy in a perfectly conducting plasma. When we set  $\alpha$  to be the zero scalar field, the rotational of the magnetic field is also zero, and hence there exists a scalar field  $\phi$  so that  $\mathbf{B} = \nabla \phi$ . Since  $\nabla \cdot \mathbf{B} = 0$ , the problem of constructing a potential field reduces to the problem of solving the Laplace equation  $\nabla^2 \phi = 0$ .

For our simulations, the boundary conditions require periodicity in the horizontal directions, and we further require the magnetic field to vanish at infinity in the third direction, so that also  $\phi$  is required to be periodic along the horizontal directions and to become constant (say zero) when  $z\gg 0$ . The boundary conditions in the horizontal directions suggest the use of harmonic analysis by rewriting the scalar field  $\phi$  as a Fourier series. This series can be slightly modified in order to match the boundary condition also in the vertical direction. A reasonable ansatz for  $\phi$  is then a linear superposition of terms of the form

$$\phi(x, y, z) = \frac{B_{k_x, k_y}}{k_z} \sin\left(k_x x + k_y y + f_{k_x, k_y}\right) e^{-k_z (z - s_{k_x, k_y})}, \quad k_z > 0, \quad (3.17)$$

for arbitrary coefficients B, f and s and some vector  $\mathbf{k}$ . It is immediate to verify that this ansatz is a solution of the Laplace equation only when  $k_x^2 + k_y^2 - k_z^2 = 0$ , so that the coefficients B, f and s are really chosen to depend on  $k_x$  and  $k_y$  alone. We then set  $k_z = \sqrt{k_x^2 + k_y^2}$  and the magnetic field  $\nabla \phi$  is then computed and analytically integrated by using Eq. (3.2) in order to derive the magnetic flux densities required by the HLLMHD scheme of the CO<sup>5</sup>BOLD code. A more general potential field can be constructed by adding many potential fields with different choices of the values for  $k_x$ ,  $k_y$ ,  $k_x$ ,  $k_y$ ,  $k_x$ ,  $k_y$ , and  $k_x$ ,  $k_y$ . For  $k_z = 0$ , we set  $\phi(x,y,z) = z B_{k_x,k_y}$ , with  $k_x = k_y = 0$ . This is also a solution of the Laplace equation corresponding to a homogeneous vertical magnetic field.

An interesting feature of this ansatz is that the corresponding average magnetic field on the horizontal layer  $z=s_{k_x,k_y}$  is  $B_{k_x,k_y}$ . This property facilitates the choice of the free parameters for the construction of a general potential field with given pre-requisites.

#### 3.6.2 The p200 magnetic configuration

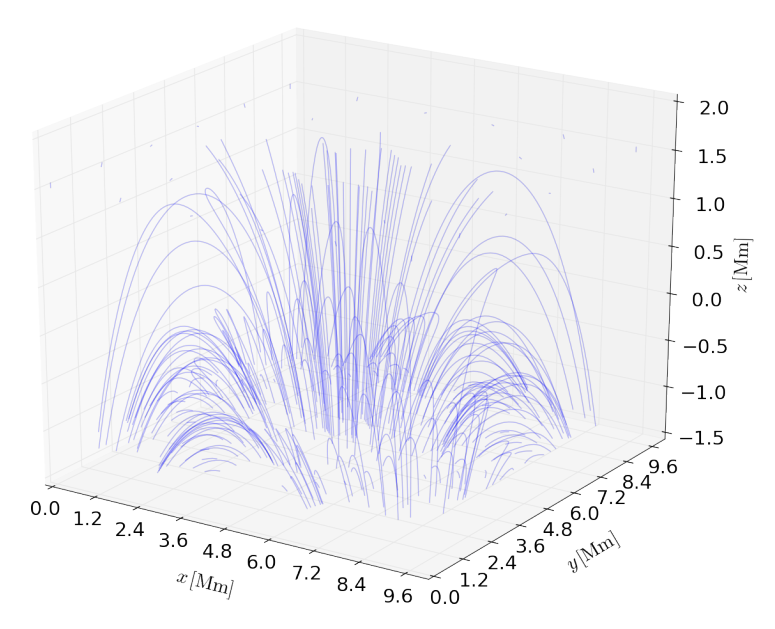


**Figure 3.3.** Magnetic field lines of the p200 configuration. Most field lines of the flux concentration at the centre of the box bend back inside it before they reach the top boundary, located at 1.3 Mm.

The p200 magnetic field configuration is constructed with three different terms of the kind of Eq. (3.17). All three terms have values  $k_x = 2\pi i/L_x$  and  $k_y = 2\pi j/L_y$  with i and j integers and with  $L_x$  and  $L_y$  the horizontal extension of the box. We can hence replace the indices  $k_x$  and  $k_y$  with the more comfortable integers i and j. We chose the three terms indexed by the pairs (i,j) = (0,0), (1,0), (0,1) with the following parameters:  $B_{0,0} = 10$  G,  $B_{1,0} = B_{0,1} = 246.4$  G,  $f_{1,0} = f_{0,1} = \pi$  and  $s_{1,0} = s_{0,1} = 0$ .

This configuration is illustrated in Fig. 3.3 displaying a cylindrical symmetric vertical structure at the centre of the box. It represents a model for two magnetic flux concentration, one with positive polarity at the centre of the box and one with negative polarity at the box boundary. Note that since the box is periodic, concentration at the box boundary is actually a single one. At the surface ( $\langle \tau \rangle = 1$ ) of the box, this configuration has an average unsigned vertical magnetic field of 200 G. This value decreases with height. Its maximal value reaches 450 G at the bottom of the box (see Fig. 3.4).

Our main motivation constructing this specific configuration is two-fold. On the one hand we aim at a non-trivial field configuration, different from the usual initial homogeneous vertical field used in photospheric MHD simulations. On the other hand we aim at a configuration with important flux concentrations 52 Bibliography

but without heavy Courant limitations. Since Alfvén waves travel faster either when density is low or when magnetic field is high, the maximum acceptable timestep is high whenever either of these situations is found. We then need to limit huge magnetic field concentrations where the plasma density is already low, which is to say, at the top of the box. We then aim at a magnetic field with strong concentration of field lines in the photosphere that bend back before they reach higher regions in the tenuous layers of the chromosphere.

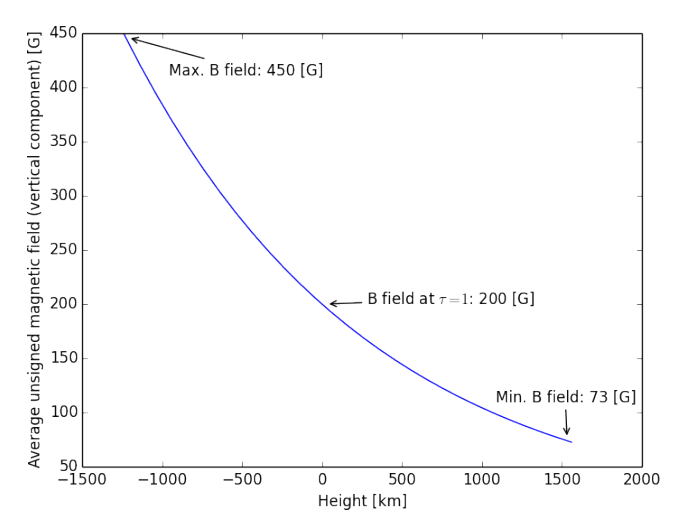


Figure 3.4. Mean unsigned vertical magnetic strength over horizontal planes of the computational box as a function of height for the initial field configuration.

Despite our efforts to produce an initial configuration that would run on times comparable to the analogous v200 configuration (same initial hydrodynamic configuration but with a homogeneous vertical 200 G magnetic field added) runtime, the new p200 model time step was soon reduced by more than two orders of magnitude. For this reason we modified the "tweak" module of the CO<sup>5</sup>BOLD code in order to incorporate the magnetic field by small amounts at each time step. This strategy was only partially successful: the p200 simulation was still running around 5-10x slower than the corresponding v200 simulation before it recovered to a time step similarly large. It was however still possible to model p200 for almost 40 minutes.

#### **Bibliography**

Christlieb, A. J., Rossmanith, J. A., & Tang, Q. 2014, "Finite difference weighted essentially non-oscillatory schemes with constrained transport for ideal magnetohydrodynamics", J. Comput. Phys., 268, 302 [arXiv:1309.3344]

Bibliography 53

Dedner, A., Kemm, F., Kröner, D., et al. 2002, "Hyperbolic Divergence Cleaning for the MHD Equations", J. Comput. Phys., 175, 645

- Evans, C. R. & Hawley, J. F. 1988, "Simulation of magnetohydrodynamic flows A constrained transport method", ApJ, 332, 659
- Freytag, B., Steffen, M., Ludwig, H.-G., et al. 2012, "Simulations of stellar convection with CO5BOLD", J. Comput. Phys., 231, 919 [arXiv:1110.6844]
- Leveque, R. J. 1998, "Nonlinear Conservation Laws and Finite Volume Methods", in Saas-Fee Advanced Course 27: Computational Methods for Astrophysical Fluid Flow., ed. O. Steiner & A. Gautschy, 1
- Powell, K. G. 1994, "Approximate Riemann solver for magnetohydrodynamics (that works in more than one dimension)", Tech. Rep. NASA-CR-194902
- Stein, R. F. & Nordlund, Å. 2006, "Solar Small-Scale Magnetoconvection", ApJ, **642**, 1246
- Steiner, O., Rezaei, R., Schaffenberger, W., & Wedemeyer-Böhm, S. 2008, "The Horizontal Internetwork Magnetic Field: Numerical Simulations in Comparison to Observations with Hinode", ApJ, 680, L85 [arXiv:0801.4915]
- Taylor, J. B. 1986, "Relaxation and magnetic reconnection in plasmas", Rev. Mod. Phys., 58, 741
- Tóth, G. 2000, "The  $\nabla \cdot B = 0$  Constraint in Shock-Capturing Magnetohydrodynamics Codes", J. Comput. Phys., **161**, 605
- Van der Vorst, H. 1992, "Bi-CGSTAB: A Fast and Smoothly Converging Variant of Bi-CG for the Solution of Nonsymmetric Linear Systems", SIAM J. Sci. Comput., 13, 631

## Non-magnetic photospheric bright points in 3D simulations of the solar atmosphere

F. Calvo, O. Steiner, and B. Freytag Published in: A&A, 596, A43 [arXiv:1612.04278]

#### Contents

4.1	Introduction	57
4.2	nMBPs from the simulations $\hdots$	<b>58</b>
4.3	From a nMBP toy-model to a recognition algorithm	62
4.4	Physical properties of nMBPs	64
4.5	nMBPs in intensity maps of virtual observations	<b>71</b>
4.6	Conclusion	<b>73</b>
Bibli	ography	<b>75</b>

#### Abstract

Context. Small-scale bright features in the photosphere of the Sun, such as faculae or G-band bright points, appear in connection with small-scale magnetic flux concentrations.

Aims. Here we report on a new class of photospheric bright points that are free of magnetic fields. So far, these are visible in numerical simulations only. We explore conditions required for their observational detection.

Methods. Numerical radiation (magneto-)hydrodynamic simulations of the near-surface layers of the Sun were carried out. The magnetic field-free simulations show tiny bright points, reminiscent of magnetic bright points, only smaller. A simple toy model for these non-magnetic bright points (nMBPs) was established that serves as a base for the development of an algorithm for their automatic detection. Basic physical properties of 357 detected nMBPs were extracted and statistically evaluated. We produced synthetic intensity maps that mimic observations with various solar telescopes to obtain hints on their detectability.

Results. The nMBPs of the simulations show a mean bolometric intensity contrast with respect to their intergranular surroundings of approximately 20%, a size of 60–80 km, and the isosurface of optical depth unity is at their location depressed by 80–100 km. They are caused by swirling downdrafts that provide, by means of the centripetal force, the necessary pressure gradient for the formation of a funnel of reduced mass density that reaches from the subsurface layers into the photosphere. Similar, frequently occurring funnels that do not reach into the photosphere, do not produce bright points.

Conclusions. Non-magnetic bright points are the observable manifestation of vertically extending vortices (vortex tubes) in the photosphere. The resolving power of 4-m-class telescopes, such as the DKIST, is needed for an unambiguous detection of them.

**Keywords.** Sun: photosphere – Sun: granulation – hydrodynamics – turbulence

4.1. Introduction 57

#### 4.1 Introduction

Brilliant minuscule features, visible in white light on the solar disk, have attracted the attention of observers from the beginning of solar physics. In the early days of solar observation, it was the faculae that were of interest, but with the advent of high resolution observation, the "solar filigree" (Dunn & Zirker 1973) or "facular points" (Mehltretter 1974) have caught the attention of observers. Later, these objects became well-known as the "G-band bright points" (Muller & Roudier 1984), which were investigated in great detail with the Swedish Solar Telescope (SST), for example by Berger & Title (1996, 2001) and Berger et al. (2004). Both faculae and G-band bright points host concentrations of magnetic fields with a strength of approximately 1000 Gauss, which are indeed at the origin of the brightenings. Utz et al. (2014) give properties of individual- and the statistics of an ensemble of 200 magnetic bright points, observed with the 1 m balloon-borne solar telescope Sunrise.

Magnetohydrodynamic simulations have been carried out to explain the brilliance, shape, and physics of faculae (e.g. Carlsson et al. 2004; Keller et al. 2004; Steiner 2005; Beeck et al. 2013, 2015), the origin of *G*-band bright points and their congruency with magnetic flux concentrations (e.g. Shelyag et al. 2004; Nordlund et al. 2009) or properties of the solar filigree (e.g. Vögler et al. 2005; Stein 2012; Moll et al. 2012). Various explanations on the extra contrast of *G*-band bright points were provided by Steiner et al. (2001), Sánchez Almeida et al. (2001), or Schüssler et al. (2003).

Non-magnetic photospheric bright points have also been reported to exist (Berger & Title 2001; Langhans et al. 2002). These features are likely parts of regular granules, or the late stage of collapsing granules, or tiny granules. Turning to numerical simulations, Moll et al. (2011) find in their simulations the formation of strong, vertically oriented vortices and they discuss a single event that gives rise to a depression in the optical depth surface  $\tau=1$  and a locally increased radiative bolometric intensity of up to 24%, confined to within an area of less than 100 km in diameter. Since this event occurs in a simulation that contains only a weak magnetic field, their bright point is essentially non-magnetic in nature. Freytag (2013, Fig. 6) shows a bolometric intensity map of the hydrodynamic (non-magnetic) high-resolution CO<sup>5</sup>BOLD run d3t57g44b0, which shows a number of brilliant tiny dots. This run contributes part of the data that is analyzed herein. The present paper focuses on the derivation of statistical properties of this type of bright point rather than on single events or their mechanism.

In this paper, we report on two magnetic field-free radiation-hydrodynamics simulations, which show tiny bright features of about 50–100 km in size, located in the intergranular space, well separated from granules, yet non-magnetic by construction. They obviously represent another class of photospheric bright feature, which we henceforth refer to as *non-magnetic bright points* (nMBPs).

From these simulation data, we extract a total of 357 nMBPs from which we derive statistical properties and we investigate conditions for the observational detection of them. In Sect. 4.2, a representative nMBP is displayed and we propose a theoretical toy model for it that provides us the basis for a recognition algorithm that is given in Sect. 4.3. The basic physical properties and statistics of the nMBPs are presented in Sect. 4.4. In Sect. 4.5 we look at synthetic intensity maps and discuss conditions for the observation of nMBPs. Conclusions are given in Sect. 4.6.

#### 4.2 nMBPs from the simulations

The magnetic field-free, three-dimensional simulations that we have carried out cover a horizontal section (field-of-view) of  $9600 \times 9600 \,\mathrm{km}^2$  of the solar atmosphere, extending from the top of the convection zone beyond the top of the photosphere over a height range of  $2800 \,\mathrm{km}$ . The optical depth surface  $\tau_{500\mathrm{nm}} = 1$  is located approximately in the middle of this height range. The spatial resolution of the computational grid is  $10 \times 10 \times 10 \,\mathrm{km}^3$  (size of a computational cell), identical in all directions. A full data cube of the simulation (full box) is stored every 4 min, whereas a two-dimensional map of the vertically directed, bolometric radiative intensity at the top boundary is produced every  $10 \,\mathrm{s}$ .

The simulations were carried out with the CO<sup>5</sup>BOLD code, a radiative magneto-hydrodynamics code described in Freytag et al. (2012). For our present study of nMBPs, we use the run carried out with the hydrodynamic Roe module, which implements an approximate Riemann solver of Roe type (Roe 1986) and a radiative transfer module based on long characteristics and the Feautrier scheme. Multi-group opacities with five opacity bands were used. The simulation started from a former relaxed simulation of lower spatial resolution, which was interpolated to the present higher resolution and relaxed for another 30 min physical time. Computations were carried out on two different machines at the Swiss National Supercomputing Center (CSCS) in Lugano and on a machine at the Geneva Observatory. The simulation was evolved for 1.5 h physical time after the relaxation phase and reproduces, with excellent fidelity, the well known granular pattern of the solar surface and magnetic bright points in the intergranular space if magnetic fields are added. We call this simulation run Roe<sub>10</sub>.

For the statistical analysis in Sect. 4.4, we also used the simulation run described in Freytag (2013), referred to as d3t57g44b0n025. It is computed with the same hydrodynamic solver as  $Roe_{10}$  but has an even finer spatial resolution with 7 km cell-size in all directions; we therefore call it  $Roe_7$  for short. This simulation covers a field-of-view of  $5600 \times 5600 \,\mathrm{km}^2$ , and was computed with one single opacity band (grey opacity) and full boxes were

**Table 4.1.** Box and cell sizes, number of opacity bands,  $n_{\text{opbds}}$ , and run duration,  $t_{\text{run}}$ , for the two simulation runs Roe<sub>10</sub> (d3t57g45b0roefc) and Roe<sub>7</sub> (d3t57g44b0).

Run	Cell size [km <sup>3</sup> ]	Box size $[\mathrm{Mm}^3]$	Height range [km]	$n_{ m opbds}$	$t_{ m run}$
$Roe_{10}$	$10\times10\times10$	$9.6\times9.6\times2.8$	-1240 < z < 1560	5	$2.6\mathrm{h}$
$Roe_7$	$7\times7\times7$	$5.6\times5.6\times2.8$	-2540 < z < 260	1	$1.5\mathrm{h}$

**Notes.** z = 0 refers to the mean optical depth one.

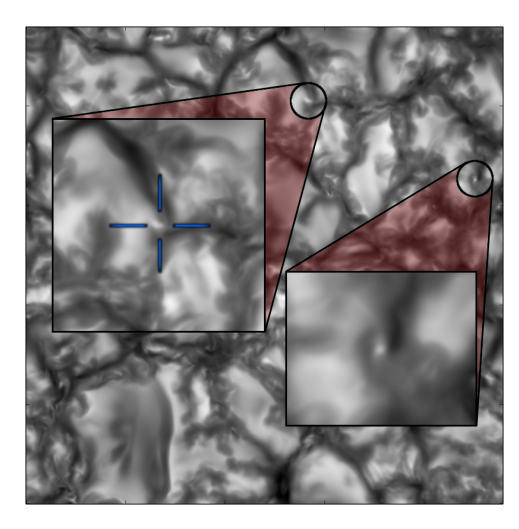


Figure 4.1. Bolometric intensity map of the non-magnetic simulation of a field of view of  $9.6 \times 9.6 \text{ Mm}^2$ . The nMBP in the close-up on the *left* has a diameter of 80 km (resolved by approximately  $8 \times 8$  computational cells). It has an intensity contrast of 35% with respect to the immediate neighbourhood but only 5% with respect to the global average intensity. A second nMBP is visible in the close-up on the *lower right*. Vertical sections along the blue lines in the close-up on the *left* are shown in Fig. 4.2. This figure is accompanied by a movie.

stored every 10 min for a time span of 3 h. The two runs are summarized in Table 4.1.

Figure 4.1 shows two nMBPs in one of the intensity maps taken at  $t=240\,\mathrm{s}$  after the relaxation phase of run Roe<sub>10</sub>. Like magnetic bright points, they are located in the intergranular space but are smaller in size. From the accompanying movie one can see that nMBPs appear in the intergranular space, often at vertices of intergranular lanes and they move with them or along intergranular lanes in a similar fashion to magnetic bright points. They often show a rotative proper motion.

Vertical sections of the density in planes along the lines of the blue cross indicated in Fig. 4.1 are shown in Fig. 4.2. In this figure, the blue curve indicates the optical depth unity for vertical lines of sight, which separates the

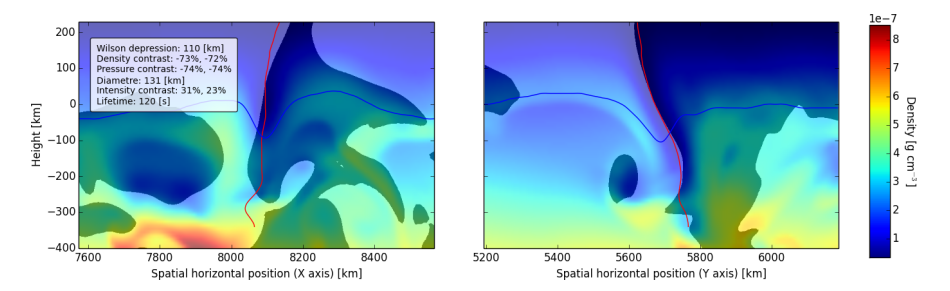


Figure 4.2. Vertical sections through the nMBP shown in Fig. 4.1. The background colour shows mass density, where the brightness encodes the sign of the velocity perpendicular to the plane of projection: bright is plasma flowing out of the plane and dark is plasma flowing into it. The red curve indicates the spine of the nMBP, a "valley" in density, found as a sequence of local density minima in horizontal planes. The blue curve indicates the Rosseland optical depth unity. The legend gives intensity, density, and gas pressure contrast, firstly with respect to the neighbourhood and secondly with respect to the global average (at  $\tau=1$  for the density and the pressure).

convection zone from the photosphere. One notices that in the location of the nMBP, there is a funnel of reduced density (colour scale) that extends from the photosphere into the convection zone. The red curve indicates the local minimum of the density in horizontal planes. Similar funnels of low density are also found in connection with magnetic bright points. However, in the context of small-scale magnetic flux-tube models (see, e.g. Spruit 1976; Zwaan 1978; Steiner et al. 1986; Fisher et al. 2000; Steiner 2007) the pressure gradient caused by this low density region is balanced by the magnetic pressure of the magnetic field concentration.

The underlying mechanism causing nMBPs is necessarily different because no magnetic pressure is available. We can get information about this mechanism by looking at the Eulerian momentum equation

$$\frac{\partial \mathbf{v}}{\partial t} + (\mathbf{v} \cdot \nabla) \mathbf{v} + \frac{1}{\rho} \nabla P + \mathbf{g} = 0, \qquad (4.1)$$

where  $\mathbf{v}$  is the velocity field, t the time,  $\rho$  the mass density, P the gas pressure, and  $\mathbf{g}$  the gravitational acceleration at the solar surface. Assuming a stationary field we can neglect the first term. In a horizontal plane, gravity does not play any role, and therefore the pressure gradient can only be balanced by a particular shape of the velocity field, which appears in the advection term. In Fig. 4.2 the sign of the velocity field is encoded by means of brighter colours (velocity is going out of the plane of projection) and darker colours (velocity is going into it). Combining the information provided by the two planes, we conclude that plasma is swirling around the funnel of low density, the minimum

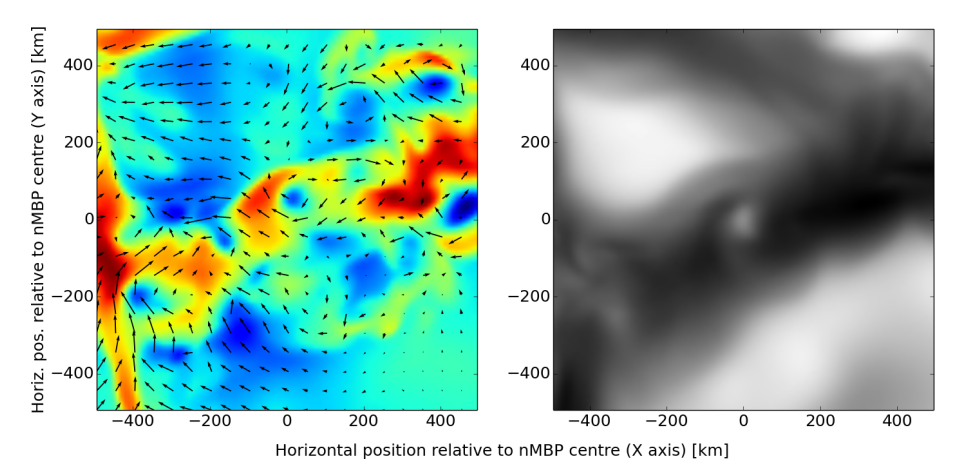


Figure 4.3. Left: low-density regions in a sub-surface layer 200 km below  $\langle \tau \rangle = 1$  sustaining swirls. The colour map extends from blue, indicating low density, to red, indicating high density, and the arrows represent the plasma velocity projected into the horizontal plane. Longest arrows correspond to a velocity of  $9.5 \,\mathrm{km\,s^{-1}}$ . Such swirling low density regions are much more abundant than nMBPs but most of them do not extend into the photosphere and therefore do not produce nMBPs. Right: corresponding bolometric intensity map. Of the several low density swirling regions in the left panel only the one at (x,y) = (0,0) produces a nMBP.

of which is marked by the red curve.

This swirling explains the stability of nMBPs only qualitatively, but it also provides insight into their formation. The plasma that rises to the photosphere by convection cools off, becomes denser, and subsequently sinks back into the convection zone in the intergranular lanes, which are smaller than the granules. Any small initial angular momentum in the plasma will lead, when downflows contract, to the generation of swirls. This effect has already been described by Nordlund (1985) in a slightly different context. There, it was referred as the "bath-tub" effect and appeared in the sub-surface layers at locations of downdrafting plumes. In our simulations we also find many locations with low densities in the sub-surface layers and corresponding swirls (see Fig. 4.3), but in general those swirls do not lead to bright points. In fact, bright points only appear if the low density funnel extends spatially from the convection zone to a significant height into the photosphere. Such an extended region of low density leads automatically to a depression of the unit optical depth isosurface (blue contour in Fig. 4.2), for which we will borrow the term "Wilson depression" in analogy to the observed depression in sunspots.

# 4.3 From a nMBP toy-model to a recognition algorithm

We now come back to the Eulerian momentum equation, Eq. (4.1). For establishing a toy model, we impose the following conditions, which derive from the properties of typical nMBPs, as the one shown in Figs. 4.1–4.3:

- 1. nMBPs are long-lived and stable so that the velocity field can be considered stationary;
- 2. they have cylindrical symmetry;
- 3. their velocity field has a non-vanishing azimuthal component;
- 4. they extend in the vertical direction and their shape does not depend on depth.

Because of the second assumption, the Euler momentum equation should be rewritten in cylindrical coordinates. The advection term is then given by

$$(\mathbf{v} \cdot \nabla)\mathbf{v} = \left[ (\mathbf{v} \cdot \nabla)v_r - \frac{v_\theta^2}{r} \right] \hat{\mathbf{r}} + \left[ (\mathbf{v} \cdot \nabla)v_\theta + \frac{v_\theta v_r}{r} \right] \hat{\theta} + (\mathbf{v} \cdot \nabla)v_z \hat{\mathbf{z}} ,$$

where the directional derivative is

$$\mathbf{v} \cdot \nabla = v_r \partial_r + \frac{v_\theta}{r} \partial_\theta + v_z \partial_z.$$

The simplest field satisfying the conditions 1–4 is

$$\mathbf{v} = v_{\theta}(r)\,\hat{\theta}\,.$$

Because of cylindrical symmetry, the pressure gradient is provided by  $(\partial_r P) \hat{\mathbf{r}} + (\partial_z P) \hat{\mathbf{z}}$ . Inserting the velocity field into the Euler momentum equation and projecting it into the horizontal plane leads to the trivial statement that the pressure gradient is in fact provided by the centripetal force

$$\frac{1}{\rho} \frac{\partial P}{\partial r} = \frac{v_{\theta}^2}{r} \,. \tag{4.2}$$

When comparing the typical nMBPs of Figs. 4.1 and 4.2 to this model, it immediately turns out that assumptions 2 and 4 are only qualitatively fulfilled. The first assumption is less straight-forward; on the one hand, the dynamical timescale for nMBPs is

$$\tau = \frac{v}{\left\| \frac{\partial \mathbf{v}}{\partial t} \right\|} = \frac{v}{\left\| (\mathbf{v} \cdot \nabla) \mathbf{v} + \frac{1}{\rho} \nabla P + \mathbf{g} \right\|},$$

and this timescale is in the order of seconds ( $6 \pm 2$  s in a  $1000 \times 1000 \,\mathrm{km}^2$  neighbourhood around the nMBP of Fig. 4.1, on the  $\tau = 1$  isosurface). On the other hand, the simulations show nMBPs to have a typical lifespan in the order of the granulation timescale. The difference between the two timescales can in fact be expected when inspecting the simulations, because even though nMBPs exist for up to five minutes, they are moving, often even rotating, and their shape is continuously changing. The model could be refined by rewriting the velocity field as  $\mathbf{v}(x,t) = \mathbf{v}_0(t) + \mathbf{v}'(x)$ , where  $\mathbf{v}_0$  is the bulk velocity of the nMBP and  $\mathbf{v}'$  is the stationary field that we have considered until now. We then get the new Euler momentum equation

$$\frac{1}{\rho} \frac{\partial P}{\partial r} = \frac{v_{\theta}^2}{r} + \frac{\partial \mathbf{v}_0}{\partial t} \,,$$

where, in general,  $\mathbf{v}_0$  should also be a non-constant coordinate-dependent field. These considerations lead to the conclusion that no simple model can fully reproduce nMBPs' behaviour. Nevertheless, the present toy model gives important insight into nMBPs and provides three correlated characteristics of them: (i) the presence of a pressure gradient, leading to a funnel of reduced density by virtue of the equation of state and therefore to a depression of the  $\tau=1$  isosurface; (ii) the presence of swirling motion and with it vorticity in the velocity field; (iii) a local intensity contrast due to a temperature contrast at the location of the depressed  $\tau=1$  isosurface. Based on this information, we have developed an algorithm by constructing an indicator (a growing function of pressure gradient, vorticity, and intensity contrast), and subsequent search of maxima of this indicator. More precisely, the steps are:

1. Compute the indicator at  $\tau = 1$ . We define  $h_{\tau=1}$  as the depth at which  $\tau = 1$ , and  $\omega_{v,z} \equiv (\nabla \times \mathbf{v})_{z,\tau=1}$  the vertical component of the vorticity, and  $T_{\tau=1}$  the temperature, all evaluated over the entire surface of  $\tau = 1$ . Then, we define  $\mathcal{N}$  as a normalization operator applied to the array of values of each physical quantity, which linearly maps each value to a new value in the [0,1] interval. More precisely, given an array  $A_{ij}$ ,

$$\mathcal{N}(A)_{ij} \equiv \frac{A_{ij} - \min_{m,n} (A_{mn})}{\max_{m,n} (A_{mn}) - \min_{m,n} (A_{mn})},$$

and the indicator function is then constructed empirically as

$$\mathcal{I} = \sqrt{\mathcal{N}\left(T_{\tau=1}\right)^2 + \mathcal{N}\left(-h_{\tau=1}\right)^2 + \mathcal{N}\left(\left|\omega_{v,\,z}\right|\right)^2} \,.$$

- 2. Find the location of maxima of the indicator using a maximum filter (with sliding window of size  $3 \times 3$ ).
- 3. For each local maximum of the indicator, search in the intensity map for

the closest intensity maximum. This defines the location of a candidate nMBP.

- 4. Select granules (which we define as regions where the vertical velocity is positive at  $\tau = 1$ ) and intergranular lanes (complementary region).
- 5. Select the intergranular, local neighbourhood in the intensity map for every candidate nMBP within an area of  $100 \times 100$  computational cells centred on the nMBP. The boundary between the nMBP and the local neighbourhood is consistently defined to separate the region of intensity  $I > \frac{1}{2} \left( I_{\text{centre}} + I_{\text{out}} \right)$ , the nMBP, from the region of intensity  $I < \frac{1}{2} \left( I_{\text{centre}} + I_{\text{out}} \right)$ , the neighbourhood.  $I_{\text{centre}}$  is the maximal intensity in the nMBP region and  $I_{\text{out}}$  is the average intensity in the neighbourhood.
- 6. Select the spine of the nMBP in three-dimensional space. To keep the computational demand low, we first extract from the full computational domain a smaller box of  $100 \times 100 \times 100$  computational cells around its centre and the  $\langle \tau \rangle = 1$  surface. Starting at the depth of  $\tau = 1$  in the centre of the nMBP and from there, layer by layer upwards and downwards, we look for local minima in the density. Exactly at  $\tau = 1$  we select the local density minimum closest to the approximate location of the nMBP as determined in step 3. For the adjacent layers, the selected local minimum is the one that is closest to that of the previous layer.
- 7. Apply step 5 to scalar physical quantities other than the bolometric intensity, on either the z=0 plane or the  $\tau=1$  isosurface. Evaluate the local and global contrast of the corresponding scalar quantity (density, gas pressure, and temperature).

This algorithm managed very well to recognize all the nMBPs that we had previously selected by eye in an arbitrary snapshot. We then applied this algorithm to the entire time sequence of the simulation, producing similar plots as shown in Figs. 4.2 and 4.3. We have examined all the selected nMBPs visually and discarded those that were not properly selected (i.e. "twin" nMBPs that were very close to each other).

# 4.4 Physical properties of nMBPs

We investigate the following physical properties of nMBPs:

**Equivalent diameter** D: computed from the area A of a nMBP as determined in step 5 of the algorithm given in the previous section. Thus,  $D \equiv 2\sqrt{A/\pi}$ .

- Wilson-depression  $W_d$ : difference in height between the deepest point on the  $\tau = 1$  isosurface of a nMBP and the average height of this surface in the neighbourhood of the nMBP as determined in step 5 of the algorithm.
- Intensity contrast  $C_I$ : computed locally and globally from  $C_I \equiv (I_p \langle I \rangle)/\langle I \rangle$ , where  $I_p$  is the average bolometric intensity of the nMBP and  $\langle I \rangle$  is either the bolometric intensity averaged over the entire intensity map (global) or in the neighbourhood (local) of the nMBP as determined in step 5 of the algorithm.
- Mass-density contrast  $C_{\rho}$ : computed locally and globally on the horizontal plane corresponding to  $\langle \tau \rangle = 1$  (i.e., z = 0) and on the  $\tau = 1$  isosurface, respectively. As determined in step 7 of the algorithm,  $C_{\rho} \equiv (\rho_0 \langle \rho \rangle)/\langle \rho \rangle$ , where  $\rho_0$  is the minimal mass density inside the nMBP at the given surface and  $\langle \rho \rangle$  is either the density averaged over the entire plane or in the neighbourhood at the given surface.
- **Pressure contrast**  $C_P$ : defined in the same way as the mass density contrast, with  $p_0$  taken at the same location as  $\rho_0$ .
- **Temperature contrast**  $C_T$ : defined in the same way as the mass density and the pressure contrast, with  $T_0$  taken at the same location as  $\rho_0$ .
- **Maximum vertical velocity**  $v_{\rm v}^{\rm max}$ : defined in the horizontal plane z=0 (corresponding to  $\langle \tau \rangle = 1$ ), inside the nMBP.
- **Maximum horizontal velocity**  $v_{\rm h}^{\rm max}$ : also defined in the horizontal plane z=0 (corresponding to  $\langle \tau \rangle =1$ ), inside the nMBP.
- **Vorticity**  $\omega_{v,z}$ : vertical component of the vorticity, defined in the horizontal plane z=0 at the same location as  $\rho_0$ .
- Lifetime: derived from a few nMBPs visually tracked on bolometric intensity maps of Roe<sub>10</sub>.

The nMBPs that enter the following statistics have been extracted from the two distinctly different magnetic field-free simulation runs  $Roe_{10}$  and  $Roe_{7}$  (see Table 4.1). The mean values and corresponding standard deviations of the physical quantities listed above (with the exception of the lifetime) are given in Table 4.2 for both simulation runs and (depending on the quantity) with respect to the plane at z=0 and/or the  $\tau=1$  surface and with respect to the local and global neighbourhood. For the lifetime, no automatic tracking of nMBPs was done because the cadence of 240 s of the full box data is not high enough. On the other hand, bolometric intensity maps are available at a high cadence of 10 s, but the tracking of nMBPs from the intensity maps alone would require involved pattern recognition techniques and criterions for the

appearance and disappearance of nMBPs. Therefore we relied on a derivation from visually tracked nMBPs on the bolometric intensity maps. Qualitatively, we found bright points existing for a duration of 30 s up to the granular time-scale of a few min.

For the first two entries in Table 4.2, the equivalent diameter D and the Wilson depression  $W_{\rm d}$ , the corresponding histograms are given in Figs. 4.4 and 4.5, respectively. From Fig. 4.4 one readily sees that the diameters of nMBPs are distinctly smaller than those of magnetic bright points, which range from 100 km to 300 km according to Wiehr et al. (2004). The median value for the diameter is 78 km and 63 km for Roe<sub>10</sub> and Roe<sub>7</sub>, respectively, while Wiehr et al. (2004) obtain 160 km for the most frequent diameter of magnetic bright points. In Fig. 4.4, one also observes that the distribution of diameters of Roe<sub>7</sub> is rather sharply limited at 30 km and 95 km, which could suggest that nMBPs are about to be resolved in this simulation. Lowering the resolution can be expected to spread this distribution, which would then explain the apparition of wings in the size distribution of Roe<sub>10</sub>. But more likely, the low end of the distribution is given by the limited spatial resolution of the simulations. On the other hand, we cannot offer a plausible explanation for the extended wide wing to larger diameters in the histogram of Roe<sub>10</sub>.

Besides the physical quantities that appear on Table 4.2, another interesting quantity is the number of nMBPs per unit area,  $n_{10}$  and  $n_{7}$ . We find  $n_{10} = 0.0712 \,\mathrm{Mm}^{-2}$  and  $n_{7} = 0.189 \,\mathrm{Mm}^{-2}$ , which indicates that at higher spatial resolution, we observe more than twice as many bright points than at lower resolution. The histograms of Figs. 4.4 and 4.5 are normalized to these respective number densities. The histogram of the equivalent diameter shown in Fig. 4.4 suggests that this surplus is due to a larger number of small bright points detected at higher spatial resolution. However, there still remains a difference of a factor of two between number densities in the two simulations when restricting statistical analyses to nMBPs larger than 60 km in diameter; a value that is significantly greater than the spatial resolution of both simulations. This suggests that the high resolution simulation not only harbours more small and tiny nMBPs but also greatly favours the formation of large nMBPs.

The distribution of the Wilson depression, given in Fig. 4.5, also shows an interesting trend: in the higher resolution model  $\mathrm{Roe}_7$ , it is globally shifted towards smaller depths compared to the distribution from  $\mathrm{Roe}_{10}$ . An intuitive explanation for this fact would be a correlation between size and Wilson depression, which, however, does not exist. There are a number of numerical parameters that differ between simulations  $\mathrm{Roe}_{10}$  and  $\mathrm{Roe}_7$  but numerous test runs confirmed that none of these seem to substantially influence the Wilson depression. We therefore found no convincing explanation why simulation  $\mathrm{Roe}_7$  shows nMBPs to have a mean Wilson depression which is approximately  $20\,\mathrm{km}$  less than that of simulation  $\mathrm{Roe}_{10}$ . In any case, the Wilson depression

**Table 4.2.** Physical quantities of nMBPs of two different simulations, Roe<sub>10</sub> with a grid size of 10 km in every spatial direction and Roe<sub>7</sub> with a grid size of 7 km in every direction.  $\mu$  is the mean value, and  $\sigma$  the standard deviation. See text for explanation of the physical quantities.

Simulation run			$Roe_{10}$		Roe <sub>7</sub>	
Mean and standard deviation			$\mu$	$\sigma$	μ	$\sigma$
D  [km]			80	21	62	15
$W_{ m d} \; [ m km]$			103	32	83	34
$C_I$	Local		21%	10%	19%	10%
	Global		2%	9%	-1%	12%
$C_{ ho}$	At $z = 0$	Local	-59%	10%	-54%	12%
		Global	-58%	10%	-57%	11%
	At $\tau = 1$	Local	-43%	14%	-39%	19%
		Global	-41%	15%	-40%	17%
	At $z = 0$	Local	-59%	10%	-54%	12%
$C_P$		Global	-61%	10%	-60%	12%
	At $\tau = 1$	Local	-38%	15%	-35%	19%
		Global	-38%	16%	-37%	18%
$C_T$	At $z = 0$	Local	-0.7%	2%	-2%	4%
		Global	-9%	4%	-8%	8%
	At $\tau = 1$	Local	8%	3%	6%	3%
		Global	5%	4%	5%	4%
$v_{\rm v}^{\rm max}  [{\rm km  s^{-1}}]$			-6.9	2.9	-5.5	4.5
$v_{\rm h}^{\rm max}  [{\rm km  s^{-1}}]$			9.5	1.3	9.2	1.1
$\sqrt{R  T_{\rm eff}  \left[1 - \left(1 + C_{\rho}\right) \left(1 + C_{T}\right)\right]}$			4.8	0.40	4.6	0.57
	$ \omega_{v,z} $	0.42	0.12	0.35	0.14	
$\omega_{v,z} \; [\mathrm{s}^{-1}]$			0.02	0.44	-0.02	0.38
$\sqrt[4]{1 + C_I} - 1 \text{ (at } \tau = 1, \text{ local)}$			5%	2%	4%	2%

**Notes.** See text for explanation of the physical quantities.

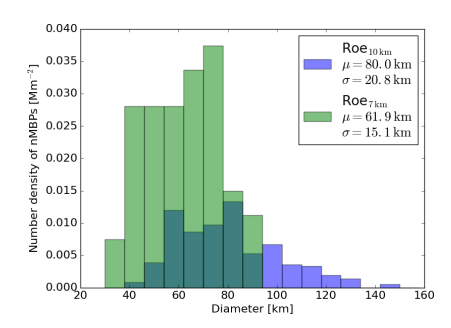


**Figure 4.4.** Size distribution of nMBPs, normalized to the average number density in the corresponding simulation.

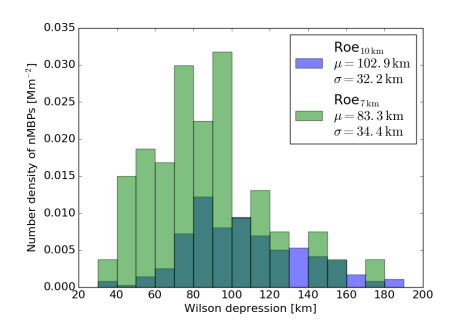


**Figure 4.5.** Distribution of the Wilson-depression of nMBPs, normalized to the average number density in the corresponding simulation.

sion of nMBPs of respectively  $103\,\mathrm{km}$  and  $83\,\mathrm{km}$  for  $\mathrm{Roe}_{10}$  and  $\mathrm{Roe}_{7}$  is again clearly smaller than corresponding values for magnetic bright points of, typically,  $150\,\mathrm{km}$  (Salhab et al., in prep.).

In Table 4.2, one can see that the average values of contrasts of intensity, mass density, pressure, and temperature do not differ substantially between the two simulations. At first, this seems to be at odds with the fact that the Wilson depression is larger in Roe<sub>10</sub> compared to Roe<sub>7</sub>. Thinking of a plane-parallel, exponentially-stratified, hydrostatic atmosphere one would expect the density contrast at  $\tau=1$  to also be larger in Roe<sub>10</sub> compared to Roe<sub>7</sub>. However, this is only partially the case. The reason is that close to  $\tau=1$ , the density runs rather constant with height due to the onset of radiative loss and a corresponding sharp drop in temperature (this is the quasi density reversal that causes the Rayleigh-Taylor instability that drives the convection). Furthermore, the funnel-shaped structure of the nMBPs accentuates this behavior; smaller radii in deeper layers go together with faster swirling motion that can sustain larger gradients in mass density and pressure, which counteracts stratification of the atmosphere inside the nMBP. The absence of exponential stratification then keeps the density contrast insensitive to the Wilson depression.

The intensity contrast (third entry in Table 4.2) is a quantity that can be directly observed. As is the case for the contrast of temperature at the  $\tau=1$  isosurface, its value drastically depends on whether it is evaluated locally (with respect to the local neighbourhood) or globally (with respect to the mean intensity/temperature). This is due to the fact that nMBPs are formed within the dark intergranular space and are, compared to granules, not so bright. Some of the nMBPs are even darker than the average intensity over the whole bolometric map, but they are still conspicuous objects within the dark intergranular lanes (see also Title & Berger 1996, for the same effect in the

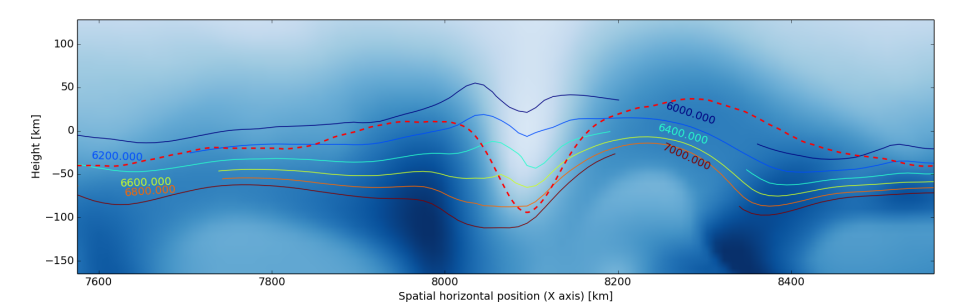


Figure 4.6. Vertical section through a typical nMBP showing isotherms (labeled coloured curves) and the mass density plotted in the background (light is low density and dark blue is high density). The  $\tau = 1$  isosurface is the dashed red curve. This surface intersects the isotherms, reaching to high temperatures where it dips deep down at the location of the nMBP at  $x \approx 8100 \,\mathrm{km}$ .

context of magnetic bright points). The contrast of the bolometric intensity of nMBPs in the order of 20% (local) and 0% (global) is again distinctively smaller than the measured global continuum contrast of magnetic bright points at 588 nm of 10% to 15% by Wiehr et al. (2004) and at 525 nm of 37% (local) and 11% (global) by Riethmüller et al. (2010). We ascribe this difference to the difference in the formation of magnetic bright points and nMBPs. Magnetic flux tubes are prone to the convective collapse instability (Spruit 1979), which leads to a high degree of evacuation and with it to a large Wilson depression and intensity contrast. No such instability and evacuation takes place in the case of nMBPs. Like Wiehr et al. (2004) for magnetic bright points, we do not find a correlation between local intensity contrast and effective diameter of nMBPs.

The temperature contrast on the isosurface of unit optical depth is positive as can be seen from Table 4.2. This can be seen in Fig. 4.6, which shows that isotherms intersect the  $\tau=1$  isosurface, similarly to magnetic bright points (see, e.g. Fig. 2 of Steiner 2007). It is interesting to note that isotherms generally also have a depression at the location of the nMBP funnel, although smaller than the depression of optical depth unity. This can be expected because of the swirling downdraft of cool photospheric material at locations of nMBPs. The temperature contrast on a horizontal plane of constant geometrical depth can therefore be negative, although it is always positive on the  $\tau=1$  isosurface, which is also the reason for the brightness of nMBPs. Pressure and density contrasts have very similar values, which is expected because both quantities are related by the equation of state, while the temperature contrast is relatively low. The nMBPs form in swirling downdrafts in the intergranular space. The maximal vertical velocity ranging from 5.5 to  $7 \, \mathrm{km \, s^{-1}}$  approaches sonic speed.

The vertical vortex event described by Moll et al. (2011) has a diameter of 80 km, a Wilson depression of 110 km, an intensity contrast of 0.24, and global density and pressure contrasts at z=0 of -0.64. This is one example observed in a simulation with a grid size of  $4\times4\times4\,\mathrm{km}^3$  as obtained with the MURaM code (Vögler et al. 2005). These values are in close agreement with the values and standard deviations given in Table 4.2 suggesting that this vortex event is of the same class of objects described herein. Correspondingly, we can consider nMBPs to be manifestations of vertically extending vortex tubes, which themselves are the manifestation of the turbulent nature of the near surface convection.

Regarding the horizontal, azimuthal velocities in nMBPs, the toy model in Sect. 4.3 provides an order of magnitude estimate. For this, we consider the relations

$$\begin{split} \frac{P_{\rm ext} - P_{\rm int}}{\rho_{\rm ext}} &\approx v_{\theta}^2 \,, \qquad \frac{\rho_{\rm int} - \rho_{\rm ext}}{\rho_{\rm ext}} \equiv C_{\rho} \,, \quad \frac{T_{\rm int} - T_{\rm ext}}{T_{\rm ext}} \equiv C_{T} \,, \\ \frac{P_{\rm ext}}{\rho_{\rm ext}} &\approx R_{\rm s} \, T_{\rm ext} \,, \qquad T_{\rm ext} \approx T_{\rm eff} \,, \end{split}$$

where P,  $\rho$ ,  $C_{\rho}$ , T,  $C_{T}$ ,  $T_{\rm eff}$  and  $v_{\theta}$  stand for gas pressure, mass density, density contrast, temperature, temperature contrast, effective temperature, and tangential velocity respectively, and  $R_{\rm s}$  is the specific gas constant for which we choose the mean molecular weight  $\mu=1.224$ . The indices "int" and "ext" refer to the centre of the nMBP funnel and to its close surrounding, respectively, always in the horizontal plane of  $\langle \tau \rangle = 1$ . The first equation is derived from Eq. (4.2). One can then express the tangential velocity as a function of density contrast, temperature contrast, and effective temperature as

$$v_{\theta} = \sqrt{R_{\rm s} T_{\rm eff} \left[1 - (1 + C_{\rho})(1 + C_T)\right]} \approx \sqrt{\frac{R_{\rm s} T_{\rm eff}}{2}} = 4.4 \,{\rm km \, s^{-1}} \,.$$

Here, we used  $C_{\rho} \approx -0.5$  and  $C_T \approx 0$  from Table 4.2, referring to the horizontal plane  $\langle \tau \rangle = 1$ . This value is approximately half the actual maximal horizontal velocity of nMBPs in the simulations, which is, close to nMBP centres, around 9–9.5 km s<sup>-1</sup> according to Table 4.2.

As expected, there are as many bright points rotating clockwise as there are rotating anti-clockwise. We verified that the average value of the vertical component of the vorticity  $\langle \omega_{v,z} \rangle$  is indeed close to zero.

Using both the Eddington-Barbier relation and the Stefan-Boltzmann law, the temperature contrast at  $\tau=1$  and the intensity contrast are related as

$$1 + C_I \approx (1 + C_T)^4$$
.

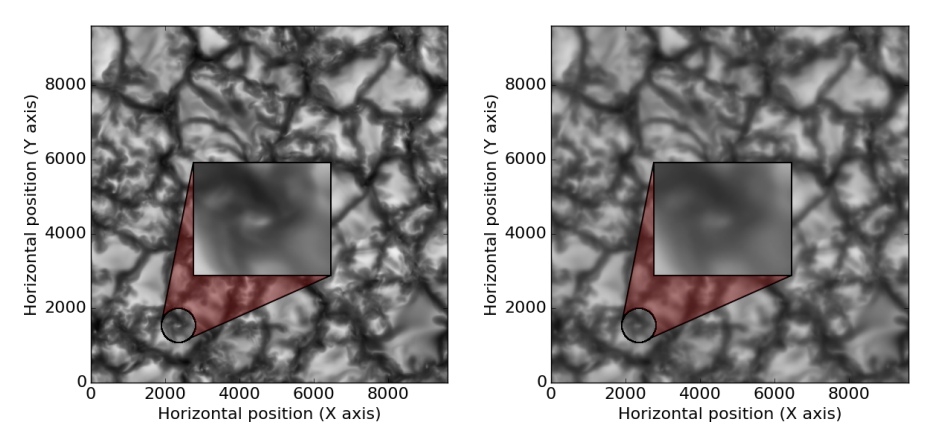


Figure 4.7. Single snapshot of the Roe<sub>10</sub> simulation showing the intensity in the continuum at 5000 Å (*left*) and the corresponding degraded image with a GREGOR-like point-spread function (right). A typical nMBP of 80 km diameter is magnified.

It is verified in the simulations that

$$\left\langle \frac{1 + C_I}{\left(1 + C_T\right)^4} \right\rangle = 1.01 \pm 0.06,$$

and the Pearson cross-correlation coefficient for these two contrasts is given by  $\rho = 0.49$  (Roe<sub>10</sub> simulation) and  $\rho = 0.35$  (Roe<sub>7</sub> simulation).

# 4.5 nMBPs in intensity maps of virtual observations

The kind of nMBPs described here have not been observed with currently operating solar telescopes, presumably because of their small size and relatively low intensity contrast. Nonmagnetic photospheric bright points have been reported to exist by Berger & Title (2001) and by Langhans et al. (2002). However, those bright points exist on the edges of certain bright, rapidly expanding granules while nMBPs are located within intergranular lanes. The objects reported by Berger & Title (2001) and by Langhans et al. (2002) are probably identical with the bright grains that often appear with the development of granular lanes (Yurchyshyn et al. 2011).

The present bright points are non-magnetic by construction, and it is therefore unclear to what extent such bright points really exist in the solar photosphere that is virtually ubiquitously occupied by magnetic fields (Lites et al. 2008). In reality, the pressure gradient that is at the origin of nMBPs is probably always provided by a combination of the centripetal force and the magnetic

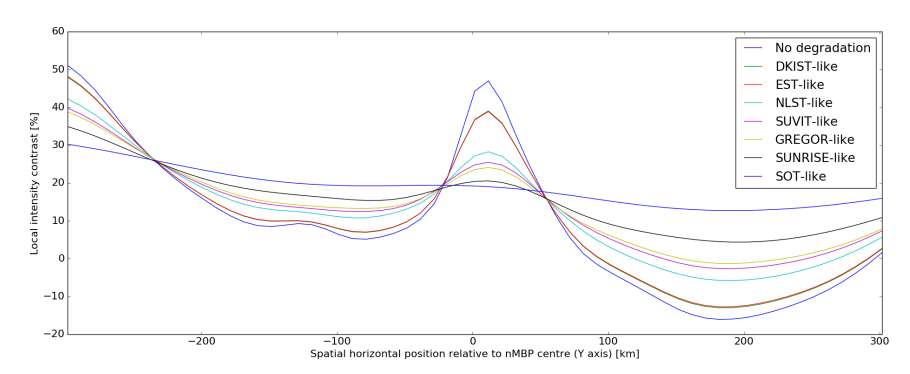


Figure 4.8. Intensity contrast in the continuum at 5000 Å across the nMBP of Fig. 4.7 (section along y-axis), using degraded images obtained with a variety of PSFs that correspond to the solar telescopes listed in the text. The legend orders the telescopes according to the simulated peak contrast, from highest to lowest. The curves with degradations corresponding to DKIST and EST are close to congruent. The coordinate x=0 corresponds to the centre of the nMBP, which is taken to be the point of lowest density in the  $\tau=1$  isosurface. Note that the peak intensity is displaced with respect to this nMBP centre because the nMBP funnel is inclined with respect to the vertical direction, as is often the case, such as that visible in the right-hand panel of Fig. 4.2.

pressure gradient, however, in regions of low magnetic flux, it may happen that the pressure gradient results mainly from the swirling motion.

In order to gain insight into the requirements for the observational detection of nMBPs, we have degraded our synthetic intensity maps to simulate observations with existing solar telescopes, such as the 50 cm Solar Optical Telescope (SOT) aboard the Hinode space observatory (Tsuneta et al. 2008), the 1 m telescope aboard the Sunrise balloon-borne solar observatory (Barthol et al. 2011), and the 1.5 m ground-based GREGOR solar telescope (Schmidt et al. 2012), as well as with future solar telescopes currently under construction, such as the 4 m Daniel K. Inouye Solar Telescope (DKIST; Keil et al. 2010), or planned solar telescopes such as the space-borne 1.5 m Solar UV-Visible-IR Telescope (SUVIT; Suematsu et al. 2014), the 2 m Indian National Large Solar Telescope (NLST; Hasan et al. 2010), and the 4 m European Solar Telescope (EST; Collados et al. 2010). The point spread functions (PSFs) that we have constructed are convolutions of the diffraction-limited PSFs, taking the entrance pupil (including secondary mirror and spider) of the various instruments into account, with Lorentz functions. The Lorentz functions are intended to account for nonideal contributions due to stray-light inside the instrument. Their  $\gamma$  parameter has been chosen to inversely scale with the telescope aperture, with the reference value for the 50 cm SOT aperture given by the greatest value deduced by Wedemeyer-Böhm (2008) from observations of the Mercury transit from 2006 and the solar eclipse from 2007. Wedemeyer-Böhm (2008) has carried

4.6. Conclusion 73

out convolutions with both Voigt and Lorentz functions in different observational situations. Unfortunately, the optimal parameters are quite sensitive to observational scenarios. We have thus decided to retain as few parameters as possible (choosing the Lorentz function over the Voigt function) and we also chose  $\gamma=9$ , when different situations suggest a range of values from  $7\pm1$  up to  $9\pm1$ . Our PSFs are therefore more realistic than simple diffraction-limited PSFs but are nonetheless not fully accurate.

According to Fig. 4.7, nMBPs could be seen using the GREGOR solar telescope. However, the spatial resolution capability of GREGOR of 0".08 at 500 nm corresponds to  $\approx 60 \,\mathrm{km}$  on the Sun, so that an 80 km nMBP would appear as a brightness enhancement in one single resolution element only. Furthermore, to be sure that the nMBP harbours no strong magnetic field, a simultaneous polarimetric measurement needs to be carried out, for which the resolution is a mere 0".3.

From Fig. 4.8 one can see that the peak intensity observed in telescopes with apertures up to 2 m is barely higher than the intensity in the immediate vicinity, and the nMBP appears larger than in the raw simulations, making it very difficult to distinguish it from other bright structures.

From this, we conclude that telescopes with large apertures, such as DKIST or EST, are needed to approach the contrast of nMBPs found in the simulations and in order to achieve sufficiently high spatial resolution in polarimetry for an unambiguous detection of nMBPs.

## 4.6 Conclusion

This paper investigates bright points that appear within integranular lanes of high-resolution, magnetic field-free, numerical simulations of the solar photosphere. The most striking properties of these features are that on the  $\tau=1$ isosurface, their temperature is, on average, 5% higher than the mean temperature (which makes them appear bright), their mass density is lower in a funnel extending from the upper convection zone to the lower photosphere, and they comprise transonic swirling motions. At the location of the bright point, the  $\tau = 1$  isosurface lies, on average,  $80 - 100 \,\mathrm{km}$  deeper than the horizontal plane z=0 (corresponding to the mean optical depth  $\langle \tau \rangle = 1$ ). At this level (z=0), their density and pressure are reduced by approximately 60% of the corresponding global average values at the same level. On average, their size (equivalent diameter) is approximately  $60 - 80 \,\mathrm{km}$ , corresponding to 0".08 -0".11, and their bolometric intensity contrast is approximately 20% with respect to their immediate intergranular surroundings. The number of nMBPs per unit area is  $0.07-0.19 \,\mathrm{Mm^{-2}}$  and their lifespan ranges from approximately 30 s up to the granular lifetime of several minutes.

Based on some of these properties an algorithm for the automatic detection

of nMBPs has been developed that enables us to derive statistics of their physical properties. Comparing the statistics of two simulations with differing spatial resolutions of 10 km and 7 km, we find nMBP equivalent diameters down to the resolution limit of the simulations. At the upper end of the size distribution, we find twice as many bright points with the higher spatial resolution as we do with the lower spatial resolution. Also, we find that in subsurface layers, swirling low density funnels are much more abundant than nMBPs. These low density funnels appear only as bright points under the condition that they extend into the photosphere. The characteristics of the nMBPs found here are in close agreement with corresponding properties of vertical vortices found by Moll et al. (2011). Thus, nMBPs are an observable manifestation of vertically directed vortex tubes, similar to bright granular lanes, which are a manifestation of horizontally directed vortex tubes (Steiner et al. 2010).

Both nMBPs and granular lanes together offer a glimpse of the elements of turbulence at work in a stratified medium, which is of basic physical interest. The nMBPs are so minuscule that they seem not to have any impact on the overall appearance of granules and the near surface convection. However, as soon as magnetic flux concentrations are attracted by and caught into the swirling down draft of a nMBP, we expect them to have a major impact on the tenuous atmosphere higher up through magnetic coupling (Shelyag et al. 2011; Steiner & Rezaei 2012). Chromospheric swirls (Wedemeyer-Böhm & Rouppe van der Voort 2009) and magnetic tornadoes (Wedemeyer-Böhm et al. 2012; Wedemeyer & Steiner 2014) would be the consequences.

Acknowledgements. This work was supported by the Swiss National Science Foundation under grant ID 200020\_157103/1 and by a grant from the Swiss National Supercomputing Centre (CSCS) in Lugano under project ID s560. The numerical simulations were carried out at CSCS on the machines named Rothorn and Piz Dora. Model d3t57g44b0 was computed at the  $P\hat{o}le$  Scientifique de Modélisation Numérique (PSMN) at the École Normale Supérieure (ENS) in Lyon. Special thanks are extended to S. Wedemeyer for help with the PSF and to the anonymous referee for very helpful comments.

# **Bibliography**

- Barthol, P., Gandorfer, A., Solanki, S. K., et al. 2011, "The Sunrise Mission", Sol. Phys., 268, 1 [arXiv:1009.2689]
- Beeck, B., Cameron, R. H., Reiners, A., & Schüssler, M. 2013, "Three-dimensional simulations of near-surface convection in main-sequence stars. II. Properties of granulation and spectral lines", A&A, 558, A49 [arXiv:1308.4873]
- Beeck, B., Schüssler, M., Cameron, R. H., & Reiners, A. 2015, "Three-dimensional simulations of near-surface convection in main-sequence stars. IV. Effect of small-scale magnetic flux concentrations on centre-to-limb variation and spectral lines", A&A, 581, A43 [arXiv:1505.04744]
- Berger, T. E., Rouppe van der Voort, L. H. M., Löfdahl, M. G., et al. 2004, "Solar magnetic elements at 0.1 arcsec resolution. General appearance and magnetic structure", A&A, 428, 613
- Berger, T. E. & Title, A. M. 1996, "On the Dynamics of Small-Scale Solar Magnetic Elements", ApJ, 463, 365
- Berger, T. E. & Title, A. M. 2001, "On the Relation of G-Band Bright Points to the Photospheric Magnetic Field", ApJ, **553**, 449
- Carlsson, M., Stein, R. F., Nordlund, Å., & Scharmer, G. B. 2004, "Observational Manifestations of Solar Magnetoconvection: Center-to-Limb Variation", ApJ, 610, L137 [astro-ph/0406160]
- Collados, M., Bettonvil, F., Cavaller, L., et al. 2010, "European Solar Telescope: Progress status", Astron. Nachr., **331**, 615
- Dunn, R. B. & Zirker, J. B. 1973, "The Solar Filigree", Sol. Phys., 33, 281
- Fisher, G. H., Fan, Y., Longcope, D. W., Linton, M. G., & Pevtsov, A. A. 2000, "The Solar Dynamo and Emerging Flux - (Invited Review)", Sol. Phys., 192, 119
- Freytag, B. 2013, "Advances in the hydrodynamics solver of CO5BOLD", Mem. Soc. Astron. Ital. Suppl., 24, 26
- Freytag, B., Steffen, M., Ludwig, H.-G., et al. 2012, "Simulations of stellar convection with CO5BOLD", J. Comput. Phys., 231, 919 [arXiv:1110.6844]
- Hasan, S. S., Soltau, D., Kärcher, H., Süss, M., & Berkefeld, T. 2010, "NLST: the Indian National Large Solar Telescope", in Proc. SPIE, Vol. 7733, Ground-based and Airborne Telescopes III, 77330I

Keil, S. L., Rimmele, T. R., Wagner, J., & ATST Team. 2010, "Advanced Technology Solar Telescope: A status report", Astron. Nachr., 331, 609

- Keller, C. U., Schüssler, M., Vögler, A., & Zakharov, V. 2004, "On the Origin of Solar Faculae", ApJ, 607, L59
- Langhans, K., Schmidt, W., & Tritschler, A. 2002, "2D-spectroscopic observations of vec G-band bright structures in the solar photosphere", A&A, 394, 1069
- Lites, B. W., Kubo, M., Socas-Navarro, H., et al. 2008, "The Horizontal Magnetic Flux of the Quiet-Sun Internetwork as Observed with the Hinode Spectro-Polarimeter", ApJ, 672, 1237
- Mehltretter, J. P. 1974, "Observations of photospheric faculae at the center of the solar disk", Sol. Phys., 38, 43
- Moll, R., Cameron, R. H., & Schüssler, M. 2011, "Vortices in simulations of solar surface convection", A&A, 533, A126 [arXiv:1108.0800]
- Moll, R., Cameron, R. H., & Schüssler, M. 2012, "Vortices, shocks, and heating in the solar photosphere: effect of a magnetic field", A&A, 541, A68 [arXiv:1201.5981]
- Muller, R. & Roudier, T. 1984, "Variability of the quiet photospheric network", Sol. Phys., 94, 33
- Nordlund, A. 1985, "Solar convection", Sol. Phys., 100, 209
- Nordlund, Å., Stein, R. F., & Asplund, M. 2009, "Solar Surface Convection", Liv. Rev. Sol. Phys., 6
- Riethmüller, T. L., Solanki, S. K., Martínez Pillet, V., et al. 2010, "Bright Points in the Quiet Sun as Observed in the Visible and Near-UV by the Balloon-borne Observatory SUNRISE", ApJ, 723, L169 [arXiv:1009.1693]
- Roe, P. L. 1986, "Characteristic-based schemes for the Euler equations", Ann. Rev. Fluid Mech., 18, 337
- Sánchez Almeida, J., Asensio Ramos, A., Trujillo Bueno, J., & Cernicharo, J. 2001, "G-Band Spectral Synthesis in Solar Magnetic Concentrations", ApJ, 555, 978 [astro-ph/0103006]
- Schmidt, W., Bell, A., Halbgewachs, C., et al. 2014, "A two-dimensional spectropolarimeter as a first-light instrument for the Daniel K. Inouye Solar Telescope", in Proc. SPIE, Vol. 9147, *Ground-based and Airborne Instrumentation for Astronomy V*, 91470E

Schmidt, W., von der Lühe, O., Volkmer, R., et al. 2012, "The 1.5 meter solar telescope GREGOR", Astron. Nachr., 333, 796

- Schüssler, M., Shelyag, S., Berdyugina, S., Vögler, A., & Solanki, S. K. 2003, "Why Solar Magnetic Flux Concentrations Are Bright in Molecular Bands", ApJ, 597, L173
- Shelyag, S., Keys, P., Mathioudakis, M., & Keenan, F. P. 2011, "Vorticity in the solar photosphere", A&A, 526, A5 [arXiv:1010.5604]
- Shelyag, S., Schüssler, M., Solanki, S. K., Berdyugina, S. V., & Vögler, A. 2004, "G-band spectral synthesis and diagnostics of simulated solar magnetoconvection", A&A, 427, 335
- Spruit, H. C. 1976, "Pressure equilibrium and energy balance of small photospheric fluxtubes", Sol. Phys., **50**, 269
- Spruit, H. C. 1979, "Convective collapse of flux tubes", Sol. Phys., 61, 363
- Stein, R. F. 2012, "Magneto-convection", Philos. Trans. Roy. Soc. London Ser., A., 370, 3070
- Steiner, O. 2005, "Radiative properties of magnetic elements. II. Center to limb variation of the appearance of photospheric faculae", A&A, 430, 691
- Steiner, O. 2007, "Photospheric processes and magnetic flux tubes", in AIP Conf. Ser., Vol. 919, *Kodai School on Solar Physics*, ed. S. S. Hasan & D. Banerjee, 74–121
- Steiner, O., Franz, M., Bello González, N., et al. 2010, "Detection of Vortex Tubes in Solar Granulation from Observations with SUNRISE", ApJ, 723, L180 [arXiv:1009.4723]
- Steiner, O., Hauschildt, P. H., & Bruls, J. 2001, "Radiative properties of magnetic elements. I. Why are vec G-band bright points bright?", A&A, 372, L13
- Steiner, O., Pneuman, G. W., & Stenflo, J. O. 1986, "Numerical models for solar magnetic fluxtubes", A&A, 170, 126
- Steiner, O. & Rezaei, R. 2012, "Recent Advances in the Exploration of the Small-Scale Structure of the Quiet Solar Atmosphere: Vortex Flows, the Horizontal Magnetic Field, and the Stokes- V Line-Ratio Method", in AJP Conf. Ser., Vol. 456, Fifth Hinode Science Meeting, ed. L. Golub, I. De Moortel, & T. Shimizu, 3

Suematsu, Y., Katsukawa, Y., Hara, H., et al. 2014, "Large aperture solar optical telescope and instruments for the SOLAR-C mission", in Proc. SPIE, Vol. 9143, Space Telescopes and Instrumentation 2014: Optical, Infrared, and Millimeter Wave, 91431P

- Title, A. M. & Berger, T. E. 1996, "Double-Gaussian Models of Bright Points or Why Bright Points Are Usually Dark", ApJ, 463, 797
- Tsuneta, S., Ichimoto, K., Katsukawa, Y., et al. 2008, "The Solar Optical Telescope for the Hinode Mission: An Overview", Sol. Phys., 249, 167 [arXiv:0711.1715]
- Utz, D., del Toro Iniesta, J. C., Bellot Rubio, L. R., et al. 2014, "The Formation and Disintegration of Magnetic Bright Points Observed by Sunrise/IMaX", ApJ, 796, 79 [arXiv:1411.3240]
- Vögler, A., Shelyag, S., Schüssler, M., et al. 2005, "Simulations of magneto-convection in the solar photosphere. Equations, methods, and results of the MURaM code", A&A, 429, 335
- Wedemeyer-Böhm, S. & Rouppe van der Voort, L. 2009, "Small-scale swirl events in the quiet Sun chromosphere", A&A, 507, L9 [arXiv:0910.2226]
- Wedemeyer, S. & Steiner, O. 2014, "On the plasma flow inside magnetic tornadoes on the Sun", PASJ, 66, S10 [arXiv:1406.7270]
- Wedemeyer-Böhm, S. 2008, "Point spread functions for the Solar optical telescope onboard Hinode", A&A, 487, 399
- Wedemeyer-Böhm, S., Scullion, E., Steiner, O., et al. 2012, "Magnetic tornadoes as energy channels into the solar corona", Nature, 486, 505
- Wiehr, E., Bovelet, B., & Hirzberger, J. 2004, "Brightness and size of small-scale solar magnetic flux concentrations", A&A, 422, L63
- Yurchyshyn, V. B., Goode, P. R., Abramenko, V. I., & Steiner, O. 2011, "On the Origin of Intergranular Jets", ApJ, 736, L35
- Zwaan, C. 1978, "On the Appearance of Magnetic Flux in the Solar Photosphere", Sol. Phys., 60, 213

# Structure of the Balmer jump

# The isolated hydrogen atom

F. Calvo, L. Belluzzi and O. Steiner Published in: A&A, 613, A55 [arXiv:1901.10241]

#### Contents

5.1	Introduction		
5.2	Absorption coefficient		
5.3	Density of quantum states		
5.4	Einstein coefficients		
	5.4.1 Reduced matrix elements		
	5.4.2 Radial wavefunctions		
5.5	Total absorption coefficient at the Balmer limit 89		
	5.5.1 Continuity of the total absorption coefficient 89		
	5.5.2 Analytic expression for the total absorption coefficient 90		
5.6	Numerical modelling of the total cross-section $\dots \dots 91$		
5.7	Conclusion		
5.A	Reduced matrix elements of the dipole operator 97		
5.B	Asymptotic properties of the Whittaker $M$ function 98		
Bibliography			

### Abstract

Context. The spectrum of the hydrogen atom was explained by Bohr more than one century ago. We revisit here some of the aspects of the underlying quantum structure, with a modern formalism, focusing on the limit of the Balmer series.

Aims. We investigate the behaviour of the absorption coefficient of the isolated hydrogen atom in the neighbourhood of the Balmer limit.

Methods. We analytically computed the total cross-section arising from bound-bound and bound-free transitions in the isolated hydrogen atom at the Balmer limit, and established a simplified semi-analytical model for the surroundings of that limit. We worked within the framework of the formalism of Landi Degl'Innocenti & Landolfi (2004, Astrophys. Space Sci. Lib., 307), which permits an almost straight-forward generalization of our results to other atoms and molecules, and which is perfectly suitable for including polarization phenomena in the problem.

Results. We analytically show that there is no discontinuity at the Balmer limit, even though the concept of a "Balmer jump" is still meaningful. Furthermore, we give a possible definition of the location of the Balmer jump, and we check that this location is dependent on the broadening mechanisms. At the Balmer limit, we compute the cross-section in a fully analytical way. Conclusions. The Balmer jump is produced by a rapid drop of the total Balmer cross-section, yet this variation is smooth and continuous when both bound-bound and bound-free processes are taken into account, and its shape and location is dependent on the broadening mechanisms.

**Keywords.** atomic processes – opacity

5.1. Introduction 81

#### 5.1 Introduction

This paper contains the first step of a work whose final goal is the numerical modelling of the Balmer jump in both the intensity and the linearly polarized spectrum of the solar radiation. Here, we investigate the behaviour of the absorption coefficient around the limit of the Balmer series, under the assumption of an isolated hydrogen atom (i.e., an atom that does not interact with any other particle) and in the absence of magnetic fields.

A numerical calculation of the absorption coefficient of the hydrogen atom near the Balmer limit, including both bound-bound and bound-free processes, was carried out by Stenflo (2005). There, the oscillator strengths (which are directly related to the Einstein B coefficients) are computed from the Gaunt factors, which have historically been tabulated, and for which approximate formulas have been derived for quick computations. Thanks to the increased computational power available today, we have opted for a different approach in this work: we start from the analytical expression of the wavefunctions of electrons and compute oscillator strengths by evaluating the radial integrals numerically. With this approach, we are no longer bound to existing tables or approximate formulas.

It must be observed that the radial integrals for the hydrogen atom have also been computed analytically, and the result expressed in a closed form (Gordon 1929). A generalized expression for hydrogenic atoms was later proposed by Menzel & Pekeris (1935), although without any proof. Almost thirty years later, Menzel (1964) provided the proof, in a simpler and more elegant way than in Gordon (1929). A closed formula for the evaluation of the oscillator strengths has therefore long been available. It requires the evaluation of hypergeometric functions, however, which can be troublesome near the series limits. As we show below, difficulties near the series limits are also met with the numerical integration methods that are developed in this work, but these methods have the advantage of being directly applicable to more complex electron wavefunctions.

The most exhaustive study of the hydrogen atom we found was performed in Bethe & Salpeter (1957), but we prefer to refer, whenever possible, to Landi Degl'Innocenti & Landolfi (2004) and more recent textbooks in order to keep a standard and more recent notation and formalism.

The structure of this contribution is as follows. In Sect. 5.2 we provide the explicit expression of the bound-bound and bound-free absorption coefficients in terms of the density of quantum states and the Einstein B coefficients. Sect. 5.3 is devoted to the computation of the density of quantum states, whereas Sect. 5.4 is dedicated to the formal computation of the Einstein coefficients from the analytic expression of the wavefunctions of the free and bound electrons. In Sect. 5.5 we match the absorption bound-bound and bound-free coefficients below and above the Balmer limit, respectively, and we analytically

show that there is no discontinuity. In addition, we analytically compute the cross-section at that precise point. Sect. 5.6 is a preliminary numerical calculation of the total cross-section (bound-bound and bound-free processes from the n=2 level) around the Balmer limit, taking only natural and thermal broadening into account.

# 5.2 Absorption coefficient

We consider a multi-level atom, and we work within the framework of the formalism of Landi Degl'Innocenti & Landolfi (2004). Each energy level is specified by the quantum numbers  $(\alpha J)$ , with J the total angular momentum, and  $\alpha$  a set of inner quantum numbers. In the absence of magnetic fields and neglecting stimulated emission, the absorption coefficient due to bound-bound transitions is given by Eq. (7.16a) of Landi Degl'Innocenti & Landolfi (2004):

$$[\eta_{i}(\nu, \mathbf{\Omega})]_{bb} = \frac{h\nu}{4\pi} \mathcal{N} \sum_{\alpha_{\ell} J_{\ell}} \sum_{\alpha_{u} J_{u}} (2J_{\ell} + 1) B(\alpha_{\ell} J_{\ell} \to \alpha_{u} J_{u})$$

$$\times \sum_{KQ} \sqrt{3} (-1)^{1+J_{\ell} + J_{u} + K} \left\{ \begin{array}{cc} 1 & 1 & K \\ J_{\ell} & J_{\ell} & J_{u} \end{array} \right\}$$

$$\times \mathcal{T}_{Q}^{K}(i, \mathbf{\Omega}) \rho_{Q}^{K}(\alpha_{\ell} J_{\ell}) \phi_{bb}(\nu_{u\ell} - \nu), \tag{5.1}$$

where  $\nu$  is the frequency of the radiation,  $\Omega$  is the propagation direction, and where the index i can take values 0, 1, 2, and 3, standing for Stokes I, Q, U, and V, respectively. The quantity h is the Planck constant,  $\mathcal{N}$  is the number density of atoms,  $B(\alpha_\ell J_\ell \to \alpha_u J_u)$  is the Einstein coefficient for absorption from a lower level  $(\alpha_\ell J_\ell)$  to an upper level  $(\alpha_u J_u)$ ,  $\mathcal{T}_Q^K(i, \Omega)$  is the polarization tensor (see Table 5.6 in Landi Degl'Innocenti & Landolfi 2004), and  $\rho_Q^K(\alpha_\ell J_\ell)$  are the multipolar components of the density matrix (or spherical statistical tensors) of the lower level. In the atomic reference frame, the absorption profile  $\phi_{\mathrm{bb}}(\nu_{u\ell} - \nu)$  is a Lorentzian, with  $\nu_{u\ell}$  the transition frequency defined by

$$\nu_{u\ell} = \frac{E_u - E_\ell}{h},\tag{5.2}$$

with  $E_u$  and  $E_\ell$  the energies of levels  $(\alpha_u J_u)$  and  $(\alpha_\ell J_\ell)$ , respectively. The threshold frequency for photoionization from a given lower level is

$$\nu_{\rm th}(\alpha_{\ell}J_{\ell}) = \frac{E_{\alpha_{+}J_{+}} - E_{\ell}}{h},\tag{5.3}$$

with  $E_{\alpha_+J_+}$  the energy of the level  $(\alpha_+J_+)$  in which the ion is left after photoionization. Indicating with  $\varepsilon_u$  the (negative) energy of the upper level  $(\alpha_uJ_u)$  in a energy scale in which  $E_{\alpha_+J_+}=0$ , the transition frequency  $\nu_{u\ell}$  can be writ-

ten as

$$\nu_{u\ell} = \nu_{\rm th}(\alpha_\ell J_\ell) + \frac{\varepsilon_u}{h} \,. \tag{5.4}$$

If the lower level is not polarized, then (see Eqs. (10.6) and (10.7) in Landi Degl'Innocenti & Landolfi 2004 for more details)

$$\rho_Q^K(\alpha_\ell J_\ell) = \delta_{K0} \, \delta_{Q0} \frac{1}{\sqrt{2J_\ell + 1}} \frac{\mathcal{N}_{\alpha_\ell J_\ell}}{\mathcal{N}},\tag{5.5}$$

with  $\mathcal{N}_{\alpha_{\ell}J_{\ell}}$  the number density of atoms in the lower level. Substituting Eq. (5.5) into Eq. (5.1), observing that  $\mathcal{T}_{0}^{0}(i,\vec{\Omega}) = \delta_{i0}$ , and using the analytical expression of the 6-j symbols when one of the arguments is zero (see Eq. (2.36a) in Landi Degl'Innocenti & Landolfi 2004), we obtain the familiar expression

$$[\eta_{i}(\nu)]_{bb} = \delta_{i0} \frac{h\nu}{4\pi} \sum_{\alpha_{\ell}J_{\ell}} \mathcal{N}_{\alpha_{\ell}J_{\ell}} \times \sum_{\alpha_{u}J_{u}} B(\alpha_{\ell}J_{\ell} \to \alpha_{u}J_{u}) \phi_{bb} \left(\nu_{th}(\alpha_{\ell}J_{\ell}) + \frac{\varepsilon_{u}}{h} - \nu\right).$$
 (5.6)

As expected, in the absence of magnetic fields, and assuming that the lower level is unpolarized, only the absorption coefficient for the intensity (i = 0) is non-zero, and it does not depend on the propagation direction of the radiation.

The absorption coefficient for bound-free transitions (in the absence of atomic polarization in the lower level) can be easily obtained in a similar way as Eq. (5.6):

$$[\eta_{i}(\nu)]_{\mathrm{bf}} = \delta_{i0} \frac{h\nu}{4\pi} \sum_{\alpha_{\ell}J_{\ell}} \mathcal{N}_{\alpha_{\ell}J_{\ell}} \times \int_{0}^{\infty} d\varepsilon \mathcal{N}_{\mathrm{f}}(\varepsilon) \sum_{ljJ'} B(\alpha_{\ell}J_{\ell} \to \alpha_{+}J_{+}, \varepsilon lj, J') \times \phi_{\mathrm{bf}} \left(\nu_{\mathrm{th}}(\alpha_{\ell}J_{\ell}) + \frac{\varepsilon}{h} - \nu\right), \tag{5.7}$$

where  $(\alpha_{\ell}J_{\ell})$  is the bound level of the atom from which photoionization takes place,  $(\alpha_{+}J_{+})$  is the level at which the ion is left,  $\varepsilon$  is the (positive) energy of the released electron, l and j are its orbital and total angular momentum, respectively, and J' is the total angular momentum of the final state  $(\vec{J'} = \vec{J_+} + \vec{j})$ . The quantity  $\mathcal{N}_f(\varepsilon)$  is the number density of quantum states of the free electron with energy  $\varepsilon$ . The profile  $\phi_{\rm bf}$  can be defined similarly as the line profile  $\phi_{\rm bb}$ , but its exact shape is irrelevant in the following derivations.

We now particularize our formalism to the case of the hydrogen atom, which we describe neglecting the spin and relativistic corrections. In this case, the atomic states are specified by the quantum numbers (nl), with n the principal quantum number  $(n \ge 1)$ , and l the orbital angular momentum (or azimuthal quantum number,  $0 \le l \le n-1$ ). The energies of the levels depend on the principal quantum number n alone. The degeneracy of the levels is  $g(n) = n^2$ . Indicating with (nl) the initial bound state, with  $(n_u l_u)$  a given upper bound state, and with  $(\varepsilon l_f)$  an arbitrary free state with positive energy  $\varepsilon$ , we have

$$[\eta(\nu)]_{bb} = \frac{h\nu}{4\pi} \sum_{nl} \mathcal{N}_{nl}$$

$$\times \sum_{n_u l_u} B(nl \to n_u l_u) \,\phi_{bb} \left(\nu_{th}(n) + \frac{\varepsilon_u}{h} - \nu\right), \tag{5.8}$$

and

$$[\eta(\nu)]_{\rm bf} = \frac{h\nu}{4\pi} \sum_{nl} \mathcal{N}_{nl}$$

$$\times \sum_{l_f} \int d\varepsilon \, \mathcal{N}_{\rm f}(\varepsilon) \, B(nl \to \varepsilon l_f) \, \phi_{\rm bf} \left( \nu_{\rm th}(n) + \frac{\varepsilon}{h} - \nu \right), \tag{5.9}$$

where we have dropped the index i, since only the absorption coefficient for the intensity is non-zero.

Near the photoionization limit, the bound states asymptotically approach the limit forming a quasi-continuum, so that the sum over the upper levels  $(n_u)$  in Eq. (5.8) can be formally substituted with an integral

$$\sum_{n_u} B(nl \to n_u l_u) \, \phi_{\rm bb} \left( \nu_{\rm th} + \frac{\varepsilon_u}{h} - \nu \right)$$

$$\to \int d\varepsilon \, \mathcal{N}_{\rm b}(\varepsilon) \, \bar{B}(nl \to \varepsilon l_u) \, \phi_{\rm bb} \left( \nu_{\rm th} + \frac{\varepsilon}{h} - \nu \right), \tag{5.10}$$

where  $\mathcal{N}_b(\varepsilon)$  is the number density of bound states with energy  $\varepsilon$ , and  $\bar{B}(nl \to \varepsilon l_u)$  is the Einstein coefficient, defined over continuous values of the energy, for the bound-bound transition between the initial level (nl) and the final level with orbital angular momentum  $l_u$  and energy  $\varepsilon$ . This Einstein coefficient could be formally obtained by interpolating the Einstein coefficient for the discrete spectrum of upper bound states, but a meaningful continuation of it will later appear in a natural way.

We now focus on the spectral region close to the photoionization threshold from a given lower level n. Close to the photoionization limit, in the frequency interval where the absorption profiles  $\phi_{\rm bb}$  and  $\phi_{\rm bf}$  significantly contribute to the integral of Eq. (5.10), the integrand is practically constant. Anticipating the numerical calculations of Sect. 5.6, we note here that the variation of  $\mathcal{N}_{\rm b}(\varepsilon) \bar{B}(nl \to \varepsilon l_u)$  across the wavelength range 3600–3700 Å is linear and

as small as 10.5 %. This variation is negligible as compared to the width of the profile, also in a realistic plasma, where due to electron-collisional broadening and other broadening mechanisms (Doppler broadening), the profile is expected to be significantly broader than that of the isolated hydrogen atom. The quantity  $\mathcal{N}_{\rm b}(\varepsilon) \bar{B}(nl \to \varepsilon l_u)$  can then be evaluated at the wavelength corresponding to the maximum of the absorption profile  $\phi_{\rm bb}$  and factorized out of the integral. We then obtain the following expressions for  $[\eta(\nu)]_{\rm bb}$  and  $[\eta(\nu)]_{\rm bf}$ :

$$[\eta(\nu)]_{\rm bb} = \frac{h^2 \nu}{4\pi} \sum_{l.l.} \mathcal{N}_{nl} \, \mathcal{N}_{\rm b}(\varepsilon_0) \, \bar{B}(nl \to \varepsilon_0 l_u), \tag{5.11}$$

with  $\varepsilon_0 = h(\nu - \nu_{\rm th}) < 0$ , and

$$[\eta(\nu)]_{\rm bf} = \frac{h^2 \nu}{4\pi} \sum_{l \, l_f} \mathcal{N}_{nl} \, \mathcal{N}_{\rm f}(\varepsilon_0) \, B(nl \to \varepsilon_0 l_f), \tag{5.12}$$

with  $\varepsilon_0 = h(\nu - \nu_{\rm th}) > 0$ .

Comparing Eqs. (5.11) and (5.12), we see that close to the photoionization limit, the absorption coefficients for bound-bound and bound-free transitions have the same formal expression. The next step is to derive and compare the explicit forms of the density of bound and free states ( $\mathcal{N}_b(\varepsilon)$  and  $\mathcal{N}_f(\varepsilon)$ ), and of the Einstein coefficients for bound-bound and bound-free transitions.

## 5.3 Density of quantum states

On the one hand, the exact form of the density of bound states  $\mathcal{N}_b$  depends on the way the discrete spectrum of upper states is treated in a continuous manner. On the other hand, as we show below, the density of free states  $\mathcal{N}_f$  is related to the normalization of the wavefunction of the free electron. To calculate these quantities, as well as the Einstein coefficients, we work in Rydberg units. Then, the energy of the nth bound level of the hydrogen atom is given by

$$\varepsilon_n = -\frac{1}{n^2},\tag{5.13}$$

leading to

$$\mathrm{d}\varepsilon = \frac{2}{n^3} \,\mathrm{d}n,\tag{5.14}$$

and therefore

$$\mathcal{N}_{\rm b}(\varepsilon) \equiv \frac{\mathrm{d}n}{\mathrm{d}\varepsilon} = \frac{n^3}{2}.$$
 (5.15)

The determination of the density of quantum states in the free "levels" is more involved, in the sense that the present formalism was developed for

transitions to discrete levels, and we are treating a continuous spectrum as a collection of discrete levels in order to stick to the same mathematical tools. Schematically, if we had split the energy range into smaller intervals and picked an approximative wavefunction of the free electron in each interval in order to compute the corresponding Einstein coefficient, the density of quantum states would depend on our splitting. In the limit where those intervals are infinitely small, the density of quantum states will depend on the way the wavefunction of the free electron is normalized. We later choose a normalization for which the density of quantum states is simply

$$\mathcal{N}_{\mathbf{f}}(\varepsilon) = 1. \tag{5.16}$$

#### 5.4 Einstein coefficients

The computation of the Einstein B coefficients is split into two steps. First we express these coefficients as an integral over the wavefunctions of the bound and free electrons. Then we rewrite the wavefunctions of the bound and free electrons in a way that facilitates an analytical integration.

#### 5.4.1 Reduced matrix elements

The Einstein coefficient for absorption from a lower state specified by the set of quantum numbers  $(\beta_{\ell})$  to an upper state specified by the set  $(\beta_u)$  is given by (e.g. combine Eqs. (7.6) and (7.7) in Landi Degl'Innocenti & Landolfi 2004)

$$B(\beta_{\ell} \to \beta_{u}) = \frac{32\pi^{4}}{3h^{2}c} \left| \left\langle \beta_{\ell} \parallel \vec{d} \parallel \beta_{u} \right\rangle \right|^{2}, \tag{5.17}$$

where  $\vec{d} = -e_0 \vec{r}$  is the dipole operator, and  $\langle \cdot \parallel \vec{d} \parallel \cdot \rangle$  is the corresponding reduced matrix element. In our case, the bottom line of the problem restricts to the evaluation of the reduced matrix elements  $\langle nl \parallel \vec{d} \parallel n_u l_u \rangle$  (for bound-bound transitions), and  $\langle nl \parallel \vec{d} \parallel \varepsilon l_f \rangle$  (for bound-free transitions). As shown in detail in Appendix 5.A, the reduced matrix element for bound-bound transitions is given by

$$\left\langle nl \parallel \vec{d} \parallel n_u l_u \right\rangle = e_0 (-1)^{l_u + 1} \sqrt{(2l_u + 1)}$$

$$\times \begin{pmatrix} l & l_u & 1 \\ 0 & 0 & 0 \end{pmatrix} \mathcal{I}(nl, n_u l_u),$$
(5.18)

where  $\mathcal{I}$  is the radial integral defined by

$$\mathcal{I}(nl, n_u l_u) = \int_0^\infty P_{nl}(r) \, r \, P_{n_u l_u}(r) \, dr, \tag{5.19}$$

with  $P_{nl}$  the reduced radial wavefunction of the bound electron. Similarly, for the bound-free transitions, we have

$$\left\langle nl \parallel \vec{d} \parallel \varepsilon l_f \right\rangle = e_0 (-1)^{l_f + 1} \sqrt{(2l_f + 1)} \times \begin{pmatrix} l & l_f & 1 \\ 0 & 0 & 0 \end{pmatrix} \mathcal{I}(nl, \varepsilon l_f), \tag{5.20}$$

with

$$\mathcal{I}(nl, \varepsilon l_f) = \int_0^\infty P_{nl}(r) \, r \, \chi_{\varepsilon l_f}(r) \, \mathrm{d}r, \qquad (5.21)$$

where  $\chi_{\varepsilon l_f}(r)$  is the reduced radial wavefunction of the free electron.

#### 5.4.2 Radial wavefunctions

The normalized radial wavefunctions are found by solving the radial Schrödinger equation for the potential  $V(\xi) = -\frac{2}{\xi}$ ,

$$\left(\frac{\mathrm{d}^2}{\mathrm{d}\xi^2} - \frac{l(l+1)}{\xi^2} - V(\xi) + \varepsilon\right) y = 0, \tag{5.22}$$

which has been nondimensionalized (or rewritten in Rydberg units) using the substitutions  $r = a_0 \xi$  and  $\varepsilon = e_0^2 \varepsilon/(2a_0)$  with  $a_0 = h^2/(4\pi^2 m_e e_0^2)$  the Bohr radius. Taking into account the normalization

$$\int_{\xi=0}^{\infty} |y(\xi)|^2 d\xi = \int_{r=0}^{\infty} |\tilde{y}(r)|^2 dr = 1,$$
(5.23)

we obtain the transformation law of the wavefunction y under change of variables,

$$y(\xi) = \sqrt{a_0}\tilde{y}(r). \tag{5.24}$$

Hence the radial integrals (5.19) and (5.21) are related to the radial integral in Rydberg units

$$\mathcal{J}(nl, n_u l_u) \equiv \int_0^\infty P_{nl}(\xi) \, \xi \, P_{n_u l_u}(\xi) \, \mathrm{d}\xi, 
\mathcal{J}(nl, \varepsilon l_f) \equiv \int_0^\infty P_{nl}(\xi) \, \xi \, \chi_{\varepsilon l_f}(\xi) \, \mathrm{d}\xi,$$
(5.25)

by the transformations

$$\mathcal{I}(nl, n_u l_u) = a_0 \, \mathcal{J}(nl, n_u l_u), 
\mathcal{I}(nl, \varepsilon l_f) = a_0 \, \mathcal{J}(nl, \varepsilon l_f).$$
(5.26)

For  $\varepsilon = -1/n^2 < 0$ , the solutions of the radial Schrödinger Eq. (5.22) can be found in Burgess & Seaton (1960) or in Griffiths (1995):

$$P_{nl}(\xi) = \frac{1}{n} \frac{(-1)^{n+l+1}}{\sqrt{\Gamma(n+l+1)\Gamma(n-l)}} W_{n,l+\frac{1}{2}} \left(\frac{2\xi}{n}\right)$$

$$= \frac{1}{n} \sqrt{\frac{\Gamma(n-l)}{\Gamma(n+l+1)}} \left(\frac{2\xi}{n}\right)^{l+1} \exp\left(-\frac{\xi}{n}\right) L_{n-l-1}^{(2l+1)} \left(\frac{2\xi}{n}\right),$$
(5.27)

which are either expressed in terms of the Whittaker W function or in terms of the generalized Laguerre polynomial (whose normalization differs in the literature),

$$L_n^{(\alpha)}(z) = \frac{\Gamma(n+\alpha+1)}{\Gamma(\alpha+1)\Gamma(n+1)} {}_{1}F_1(-n,\alpha+1,z), \tag{5.28}$$

(see e.g. Abramowitz & Stegun 1964). In turn, the confluent hypergeometric function  $_1F_1$  can be expressed through the Whittaker M function:

$$M_{\kappa,\mu}(z) = \exp\left(-\frac{z}{2}\right) z^{\mu + \frac{1}{2}} {}_{1}F_{1}\left(\mu - \kappa + \frac{1}{2}, 1 + 2\mu; z\right),$$
 (5.29)

allowing us to rewrite  $P_{nl}$  in terms of the Whittaker M function:

$$P_{nl}(\xi) = \sqrt{\frac{\Gamma(n+l+1)}{n^{2l+1}\Gamma(n-l)}} \frac{\sqrt{n^{2l-1}} M_{n,l+\frac{1}{2}} \left(\frac{2\xi}{n}\right)}{\Gamma(2l+2)}$$

$$\equiv g_{nl} \frac{\sqrt{n^{2l-1}} M_{n,l+\frac{1}{2}} \left(\frac{2\xi}{n}\right)}{\Gamma(2l+2)}.$$
(5.30)

We note that the dependence of the Einstein coefficient  $B(nl \to n_u l_u)$  for bound-bound transitions on the  $n_u$  quantum number of the upper state appears only through the Whittaker M function, hence providing a natural analytical continuation over non-integer values of  $n_u$  that we have previously introduced as  $\bar{B}(nl \to n_u l_u)$ .

For  $\varepsilon > 0$ , the solutions of the radial Schrödinger Eq. (5.22) are listed in Seaton (1958). A unique combination of these functions with the appropriate boundary conditions for the present problem, namely that the wavefunction reduces to zero in the origin and its asymptotic form at large r behaves as the

wavefunction of a free electron, is presented here:

$$\chi_{\varepsilon l}(\xi) = \frac{1}{\kappa^{l+1}} \sqrt{\frac{\Gamma(l+1+i\kappa)\Gamma(l+1-i\kappa)}{\Gamma(i\kappa)\Gamma(-i\kappa)(1-\exp(2\pi\kappa))}} \frac{(i\kappa)^{l+1} M_{i\kappa,l+\frac{1}{2}} \left(-\frac{2i\xi}{\kappa}\right)}{\sqrt{2}\Gamma(2l+2)}$$

$$\equiv h_{\kappa l} \frac{(i\kappa)^{l+1} M_{i\kappa,l+\frac{1}{2}} \left(-\frac{2i\xi}{\kappa}\right)}{\sqrt{2}\Gamma(2l+2)},$$
(5.31)

where  $\kappa \equiv 1/\sqrt{\varepsilon}$ .

# 5.5 Total absorption coefficient at the Balmer limit

#### 5.5.1 Continuity of the total absorption coefficient

Using the properties of the Euler gamma function, it is straightforward to check that

$$\lim_{n_u \to \infty} g_{n_u l_u} = \lim_{\kappa \to \infty} h_{\kappa l_f} = 1 \quad \forall l_u = l_f \in \mathbb{Z}_{\geq 0}.$$
 (5.32)

In Sect. 5.4.2 we have noted that the Einstein coefficient  $B(nl \to n_u l_u)$  is also well defined for non-integer values of  $n_u$ , and in particular, that it is a continuous function of  $n_u$ . Hence

$$\lim_{\varepsilon \to 0^{-}} \mathcal{N}_{b}(\varepsilon) \bar{B}(nl \to n_{u}(\varepsilon)l_{u}) = \lim_{n_{u} \to \infty} \mathcal{N}_{b}(\varepsilon(n_{u})) B(nl \to n_{u}l_{u}). \tag{5.33}$$

Now recalling the relation (5.54), namely

$$\lim_{\kappa \to \infty} \kappa^{\mu + \frac{1}{2}} M_{\kappa,\mu} \left( \frac{z}{\kappa} \right) = \lim_{\kappa \to \infty} (i\kappa)^{\mu + \frac{1}{2}} M_{i\kappa,\mu} \left( -\frac{iz}{\kappa} \right), \tag{5.34}$$

which is demonstrated in Appendix 5.B, and using Eq. (5.30) for the wavefunction of the bound electron  $P_{nl}$  and Eq. (5.31) for the wavefunction of the free electron  $\chi_{\varepsilon\ell}$ , we find that

$$\lim_{\varepsilon \to 0^{-}} \mathcal{N}_{b}(\varepsilon) \bar{B}(nl \to n_{u}l_{u}) = \lim_{\varepsilon \to 0^{+}} \mathcal{N}_{f}(\varepsilon) B(nl \to \varepsilon l_{f}), \tag{5.35}$$

provided that the density of quantum states are taken to be the ones obtained in Eqs. (5.15) and (5.16). The equality of Eq. (5.35) further implies the interchange of the limits with the radial integrals contained in the Einstein B coefficients, whose justification is similar to the proof of Eq. (5.54). For brevity, we do not repeat all the computations here. Some additional details are provided in the final note of Appendix 5.B, however.

After summing the bound-bound contributions to Eq. (5.11) over l and  $l_u$ 

and the bound-free contributions to Eq. (5.12) over l and  $l_f$ , we obtain our final result,

$$\lim_{\nu \to \nu_{\rm th}^-} [\eta(\nu)]_{\rm bb} = \lim_{\nu \to \nu_{\rm th}^+} [\eta(\nu)]_{\rm bf} , \qquad (5.36)$$

with the threshold frequency for the Balmer series given by

$$\nu_{\rm th} = \frac{m_e e_0^4}{16\pi\hbar^3}.\tag{5.37}$$

Thus, we have proven that there is no discontinuity at the Balmer limit.

# 5.5.2 Analytic expression for the total absorption coefficient

The wavefunction of the free electron with zero kinetic energy can be calculated combining Eqs. (5.31) and (5.54):

$$\chi_{\varepsilon=0,\ell}(r) = \frac{(2r)^{\ell+1} {}_{0}F_{1}(2\ell+2;-2r)}{\sqrt{2}\Gamma(2\ell+2)}.$$
(5.38)

The integrals of Eqs. (5.19) and (5.21) can be computed analytically. If we take the limiting wavefunction for the free electron, Eq. (5.38), and we consider the bound electron to be in the level n = 2, we find the nondimensional expressions of Eq. (5.25):

$$\mathcal{J}(n=2, L_{\ell}=0; \varepsilon=0, \ell=1) = \frac{2^{8}}{e^{4}}, 
\mathcal{J}(n=2, L_{\ell}=1; \varepsilon=0, \ell=0) = \frac{2^{7}}{\sqrt{3}e^{4}}, 
\mathcal{J}(n=2, L_{\ell}=1; \varepsilon=0, \ell=2) = \frac{2^{9}}{\sqrt{3}e^{4}}.$$
(5.39)

These are the only non-vanishing integrals, according to the selection rule  $\Delta \ell = \pm 1$ . Now inserting the reduced matrix (5.20) into Eq. (5.17), we compute the Einstein coefficients (where we have substituted the corresponding nondimensional radial integrals  $\mathcal{J}$ ):

$$B(nL_{\ell} \to \varepsilon \ell) = \frac{2h^2}{3ce_0^2 m_e^2} (2\ell + 1) \begin{pmatrix} L_{\ell} & \ell & 1\\ 0 & 0 & 0 \end{pmatrix}^2 \mathcal{J}^2(nL_{\ell}, \varepsilon \ell).$$
 (5.40)

For n=2 we can sum over all values of all contributions from the angular momentum of the bound and free electrons, in order to obtain the absorption coefficient at the Balmer limit. Next, we note that the 3-j symbol for  $\ell=L_{\ell}\pm 1$ 

can be computed using the property

$$\begin{pmatrix} a & a+1 & 1 \\ \alpha & -\alpha & 0 \end{pmatrix} = (-1)^{a-\alpha-1} \sqrt{\frac{(a-\alpha+1)(a+\alpha+1)}{(a+1)(2a+1)(2a+3)}},$$
 (5.41)

and the fact that squares of 3-j symbols are invariant under permutation of any two columns:

$$(2\ell+1) \begin{pmatrix} L_{\ell} & \ell & 1 \\ 0 & 0 & 0 \end{pmatrix}^{2} = \frac{\max(L_{\ell}, \ell)}{2L_{\ell} + 1}.$$
 (5.42)

Making use of Eqs. (5.8) and (5.9), summing over the final states, and converting the density of quantum states into c.g.s units finally leads us to

$$\eta_0^{\rm A}(\nu_{\rm th}) = \frac{h^6 \nu_{\rm th}}{12\pi^3 c e_0^6 m_e^3} \left( \mathcal{N}_{n=2; L_\ell=0} \frac{2^{16}}{e^8} + \mathcal{N}_{n=2; L_\ell=1} \left( \frac{2^{14}}{9e^8} + \frac{2^{19}}{9e^8} \right) \right). \quad (5.43)$$

Using the Boltzmann equation, we obtain the relative populations of the n=2 level:

$$\frac{\mathcal{N}_{n=2;L_{\ell}=0}}{\mathcal{N}_{n=2}} = \frac{1}{4}, \quad \frac{\mathcal{N}_{n=2;L_{\ell}=1}}{\mathcal{N}_{n=2}} = \frac{3}{4}, \tag{5.44}$$

providing the final result:

$$\eta_0^{\mathcal{A}}(\nu_{\text{th}}) = \mathcal{N}_{n=2} \frac{h^6 \nu_{\text{th}}(n=2)}{12\pi^3 c e_0^6 m_e^3} \frac{2^{12} \times 3 \times 5}{e^8} \\
= \mathcal{N}_{n=2} \frac{4\pi^2}{3} \left(\frac{\alpha a_0^2}{n^2}\right)_{n=2} \frac{2^{12} \times 3 \times 5}{e^8} \\
\approx \mathcal{N}_{n=2} \times 1.386 \times 10^{-17} \text{ [cm}^2\text{]},$$
(5.45)

in which we have introduced the frequency at the Balmer limit given in Eq. (5.37), and where  $a_0$  is the Bohr radius and  $\alpha = e_0^2/(\hbar c) \approx 1/137$  is the fine structure constant.

# 5.6 Numerical modelling of the total crosssection around the Balmer limit

At some point near the Balmer limit, the distance between consecutive spectral lines becomes smaller than the width of the lines (FWHM). The exact location of this wavelength  $\lambda_t$  representing the transition between these two regimes depends on the broadening of the spectral lines. At wavelengths longer than  $\lambda_t$ , we still observe distinct spectral lines, but at shorter wavelengths, we no longer resolve spectral lines, but observe a quasi-continuum.

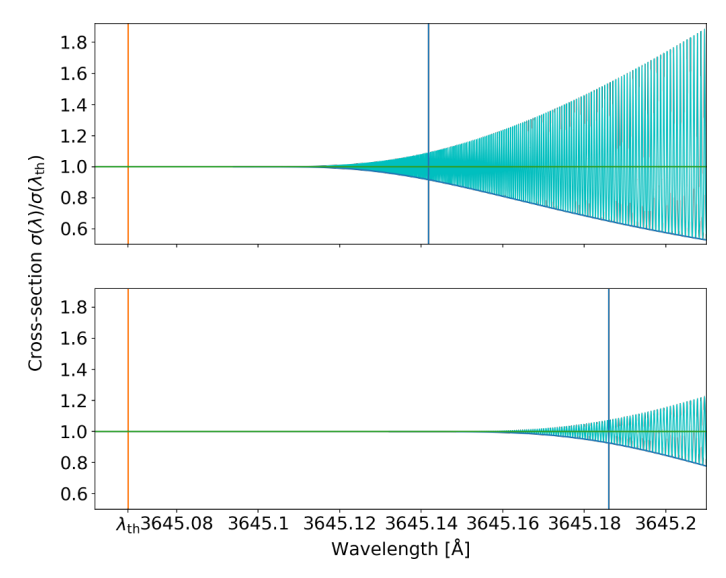


Figure 5.1. Total cross-section (cyan) due to bound-bound and bound-free transitions in the isolated hydrogen atom around the Balmer limit  $\lambda_{\rm th}$ , considering natural broadening (top), or including both natural broadening and Gaussian broadening for a thermal velocity of  $15\,\mathrm{m\,s^{-1}}$  (bottom). The cross-section is normalized to its analytic value at the Balmer limit  $\lambda_{\rm th}$ . At longer wavelengths, the actual continuum (blue curve), defined as the lower envelope of the bound-bound cross-section, deviates from the nominal quasi-continuum (almost-horizontal green curve that was computed by assuming the approximation of Eq. (5.10) to be valid at all wavelengths  $\lambda > \lambda_{\rm th}$ ). The orange vertical solid lines show the location of the Balmer limit  $\lambda_{\rm th}$ . The blue vertical lines show the location at which the FWHM of spectral lines and the separation between consecutive spectral lines are equal ( $\lambda_t$ ). In the bottom plot, this line is displaced to longer wavelength due to the additional broadening caused by the thermal velocity.

In the following paragraphs we describe the procedure we used to numerically compute the total cross-section in the vicinity of the Balmer limit (Fig. 5.1). The total Balmer cross-section is defined by

$$\sigma_{\text{Bal.}}(\nu) = \frac{h^2 \nu}{4\pi} \sum_{\ell} \left( \frac{\mathcal{N}_{n=2; l=0}}{\mathcal{N}_{n=2}} \bar{B}(n=2; l=0 \to \varepsilon_0 \ell) + \frac{\mathcal{N}_{n=2; l=1}}{\mathcal{N}_{n=2}} \bar{B}(n=2; l=1 \to \varepsilon_0 \ell) \right),$$

$$(5.46)$$

where  $\ell$  stands here for either  $l_u$  or  $l_f$ , and the relative populations of the n=2 level are taken to be the same as in Eq. (5.44), with l being a shorthand notation for the angular momentum of the lower lever  $L_{\ell}$ . The procedure to compute this cross-section is non-trivial because the wavefunctions of both the free and

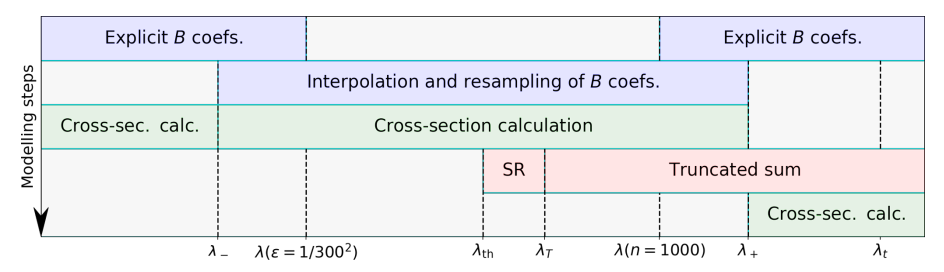


Figure 5.2. Steps involved in the modelling of the total cross-section around the Balmer limit. The Einstein B coefficients are first calculated, either explicitly or by interpolation (blue). The cross-section is then computed for  $\lambda < \lambda_+$  (upper green region) using either Eq. (5.11) or Eq. (5.12). For  $\lambda > \lambda_+$ , the distance between lines is comparable to the line's FWHM, so that the approximation of Eq. (5.10) is no longer valid, and lines have to be computed individually, considering both a finite truncated sum and its sum remainder (SR; red). The opacity of the lines is finally summed at wavelengths  $\lambda > \lambda_+$  (lower green region).

bound electrons have singularities at the Balmer limit, leading to numerical difficulties around this region. Moreover, the number of spectral lines to be considered is in principle infinite. The total cross-section at wavelengths larger than the wavelength of the Balmer limit ( $\lambda_{\rm th}$ ) is given as an infinite sum of cross-sections due to each transition from the second level to any higher level. Approaching (from larger wavelengths) the specific point where the line width and the spacing between neighbouring lines are comparable ( $\lambda = \lambda_t$ ), this sum cannot be truncated because the remaining terms are non-negligible and their sum decreases extremely slowly when the truncation threshold increases. However, it is possible to split the sum into two terms, one containing a sum over a finite number of spectral lines located at wavelengths longer than some threshold,  $\lambda_T$ , and one containing an infinite sum over spectral lines located at shorter wavelengths (between  $\lambda_{\rm th}$  and  $\lambda_T$ ). The infinite sum can then be approximated by an integral, with the same approach as used in Eq. (5.10).

The choice of  $\lambda_T$  is quite empirical, but  $\lambda_T \ll \lambda_t$  is always required and  $\lambda_T$  has therefore to be adjusted according to the line broadening. In the limit  $\lambda_T \to \lambda_{\rm th}$ , where the chosen threshold approaches the Balmer limit, the error arising from the approximation in Eq. (5.10) drops to zero, but the number of lines for which the Einstein coefficient has to be explicitly computed increases drastically. Moreover, close to the limit  $\lambda_{\rm th}$ , both below and above it, numerical evaluation at finite precision of the Einstein B coefficients is troublesome (see e.g. Morabito et al. 2014). For simplicity, in the present work, we explicitly compute the Einstein B coefficients inside a safe range (for 1000 bound-bound transitions and 300 bound-free transitions) and interpolate its values for transitions closer to the limit. More precisely, we interpolate the values of  $\mathcal{N}_{\rm b}(\varepsilon)B(nl \to n_u l_u)$  together with those of  $\mathcal{N}_{\rm f}(\varepsilon)B(nl \to \varepsilon l_f)$ , since

we know, according to Eq. (5.35), that they match at the Balmer limit. The evaluation of the Einstein B coefficients is illustrated in blue in Fig. 5.2.

The wavelength range in which we perform the numerical calculation of the total cross-section is finally split into three sub-domains, represented in green in Fig. 5.2:  $\lambda < \lambda_-$ , for which Eq. (5.12) is used;  $\lambda_- \leq \lambda < \lambda_+$ , for which either Eq. (5.11) or Eq. (5.12) are used, but the Einstein B coefficients have interpolated and resampled values; and  $\lambda \geq \lambda_+$ , for which the sum in Eq. (5.8) is truncated. The truncated part includes a total of 5000 bound-bound transitions, most of which were computed with the interpolated B coefficients, and the remainder of the sum is approximated using Eq. (5.10), in which all B coefficients are interpolated (SR). This is schematically represented by the red domains in Fig. 5.2.

We note that for  $\lambda < \lambda_{\rm th}$ , the total cross-section varies very slowly, so that the choice of  $\lambda_-$  is not really important as the interpolation between  $\lambda_-$  and  $\lambda_{\rm th}$  will provide accurate results. However,  $\lambda_T$  should be chosen as close as possible to  $\lambda_{\rm th}$  and should satisfy both  $\lambda_T \ll \lambda_t$  and  $\lambda_T \ll \lambda_+$  to obtain an accurate total cross-section, requiring an explicit computation of a large number of lines. The considered 1000 bound-bound transitions with the Einstein B coefficients computed explicitly is not sufficient, and additional transitions (till  $n_u = 5000$ , corresponding to  $\lambda_T$ ) are considered using the interpolated Einstein B coefficients.

For line transitions to a higher level with quantum number  $n_u$  above the  $n_u = 81$  threshold, the natural broadening of the lines is extrapolated. Below that threshold, the natural broadening is explicitly computed using Eq. (6.59b) in Landi Degl'Innocenti & Landolfi (2004) (see Fig. 5.3):

$$\Gamma = \frac{\gamma_{\rm l} + \gamma_{\rm u}}{4\pi},\tag{5.47}$$

where  $\gamma_1$  and  $\gamma_u$  are the inverse lifetimes of the lower and upper levels. The inverse lifetimes are given by the effective Einstein A coefficients, which are computed using Eq. (63.8) in Bethe & Salpeter (1957) and the usual relations between the Einstein A and B coefficients. Above  $n_u = 81$ , the extrapolation is carried out by fitting a (semi-empirical) power law  $\gamma_u(n) \sim an^{-b}$ .

Figure 5.1 was produced using the methods described above. It is not to be directly compared to a realistic plasma, but it exhibits some characteristic features that are expected to be found in observations as well. First of all, no discontinuity is found anywhere, and in particular, nothing special occurs at the Balmer limit. However, the lower envelope of the spectral lines, interpreted as the "continuum", quickly drops to lower cross-sections. On a spectrum exhibiting a wider range of wavelengths, it would almost appear as a "jump".

The location of the jump is not well defined. Longward of the Balmer limit, close inspection indeed reveals the existence of oscillations up to the limit.

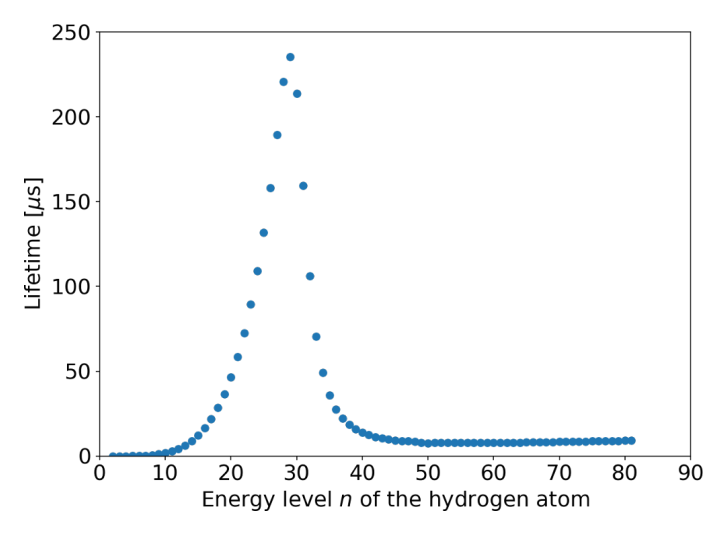


**Figure 5.3.** Lifetimes of the atomic levels n of the hydrogen atom for 1 < n < 82.

With a limited spectral resolution, however, there will be a wavelength short-ward of which the oscillating cross-section (lines) become a quasi-continuum. In Fig. 5.1 the vertical blue line on the right of each panel is the position at which the FWHM of spectral lines is equal to the line separation, and it could be taken as the definition of the Balmer's jump position.

By comparing the plot in the top panel of Fig. 5.1 (no thermal broadening) with the plot in the bottom panel (thermal broadening corresponding to a thermal velocity of  $15\,\mathrm{m\,s^{-1}}$ ), we see that the (rather arbitrary) point in which the lines become a quasi-continuum is displaced towards longer wavelengths. The position of this point is very sensitive to the broadening mechanisms that are considered. In the solar plasma, with a temperature of about 6200 K (as expected at the depth at which the solar continuum is formed), and considering only natural and thermal broadening, we expect a displacement of the Balmer jump of approximately  $7\,\mathrm{\mathring{A}}$ .

We note that an alternative definition of the Balmer jump is given in Stenflo (2005), according to which the Balmer jump is located at the wavelength on which the Balmer continuum (lower envelope of spectral lines in Fig. 5.1) intersects the Lyman continuum. This alternative definition has the advantage to better fit what visually looks like the Balmer jump of the intensity spectrum of the Sun, and is located at wavelengths much longer than our definition (in the cited paper, for solar conditions and taking also pressure broadening mechanisms into account, the position is reported to be shifted by 140  $\mathring{A}$ , while a shift of 100  $\mathring{A}$  is reported from observational data).

We emphasize that the Gaussian broadening displayed in the bottom panel of Fig. 5.1 is not representative of any specific plasma. Its only purpose is

to provide a qualitative description of the effect of additional broadening. In addition to the thermal Gaussian broadening (Doppler broadening), the interaction between the almost-free electrons close to the photoionization threshold and the electric field of the surrounding ions and electrons in a realistic plasma has to be taken into account (see e.g. Griem 1960). The electric field is not only responsible for the usual linear and quadratic Stark broadening (which rapidly increases with the principal quantum number of the levels), but it also provides an unbounded contribution to the Hamiltonian, which results in the quenching of the lines with high upper quantum number n. This latter aspect has been studied by Lanczos (1931), and it is also described at the end of the chapter on the Stark effect in the book of Bethe & Salpeter (1957).

#### 5.7 Conclusion

The Balmer jump is produced by a rapid drop of the total Balmer cross-section, but this variation is smooth and continuous when both bound-bound and bound-free processes are taken into account, and its shape and location are dependent on how it is defined and on the broadening mechanisms. A possible definition of the position of the Balmer jump is the location at which the distance between consecutive spectral lines equals the FWHM of the spectral lines. In this work, we have considered an isolated hydrogen atom (no collisions), and we have found that this location is shifted about 7 Å longward of the Balmer limit when considering thermal broadening under solar conditions with respect to the ideal situation in which only natural broadening comes into play.

Moreover, we have shown that at specific wavelengths, and in particular at the Balmer limit, it is possible to compute the cross-section in a fully analytical way. At the Balmer limit, we found this value to be proportional to  $\alpha a_0^2$ , with  $\alpha$  being the fine-structure constant,  $a_0$  being the Bohr radius, and the proportionality constant being the pure mathematical constant  $\pi^2 \, 2^{12} \times 5 / \exp(8)$ .

We proposed a method to deal numerically with the accumulation of an infinite amount of lines and applied it to the simple case of the hydrogen atom near the Balmer limit. We expect this method to be also applicable to the accumulation of spectral lines formed by more complex atoms or molecules. The modelling of the spectrum near the Balmer limit, taking the interactions with the surrounding plasma into account, is expected to be significantly more complex than the present approach and is therefore left for a future work.

## 5.A Reduced matrix elements of the dipole operator

The reduced matrix elements  $\langle \alpha J \parallel \mathbf{d} \parallel \alpha' J' \rangle$  of the dipole operator  $\mathbf{d} = -e_0 \mathbf{r}$  can be expressed in terms of a radial integral in a quite general way by assuming that the quantum numbers contained in  $\alpha$  and  $\alpha'$  are eigenvalues of operators commuting with angular momentum. We start from the Wigner–Eckart theorem as given in Eq. (2.96) of Landi Degl'Innocenti & Landolfi (2004):

$$\langle \alpha JM \mid T_q^k \mid \alpha' J' M' \rangle$$

$$= (-1)^{J'+k+M} \sqrt{2J+1} \begin{pmatrix} J & J' & k \\ -M & M' & q \end{pmatrix} \langle \alpha J \parallel \mathbf{T}^k \parallel \alpha' J' \rangle , \quad (5.48)$$

which is inverted using the orthogonality relations of the 3-j symbols:

$$\langle \alpha J \parallel \mathbf{T}^{k} \parallel \alpha' J' \rangle = (-1)^{J'+k+M} \sqrt{2J+1} \times \sum_{M',q} \begin{pmatrix} J & J' & k \\ -M & M' & q \end{pmatrix} \langle \alpha J M \mid T_{q}^{k} \mid \alpha' J' M' \rangle,$$
 (5.49)

and which holds for any  $M \in \{-J, -J+1, \ldots, J-1, J\}$ . By definition, an irreducible spherical vector rotates with the same transformation law as the l=1 components of the spherical harmonics  $Y_l^m$ . Hence, from the components  $(T_x, T_y, T_z)$  of an arbitrary Cartesian vector  $\mathbf{T}$  with norm T, we can construct a spherical vector whose components are given by  $cTY_1^m(\mathbf{T}/T)$ , with c an arbitrary constant.

Fixing c provides a one-to-one relation between Cartesian vectors and irreducible spherical vectors. For consistency with Eq. (5.17), the constant is chosen so that the spherical components of the vector field operator  $\mathbf{r}$  are given by Eq. (2.82) of Landi Degl'Innocenti & Landolfi (2004):

$$r_m^1 = \sqrt{\frac{4\pi}{3}} r Y_1^m(\hat{\mathbf{r}}),$$
 (5.50)

which is inserted in the inverted version of the Wigner–Eckart theorem. After setting M=0, the resulting expression reads

$$\langle \alpha J \parallel \mathbf{d} \parallel \alpha' J' \rangle = e_0 (-1)^{J'+1} \sqrt{2J+1} \langle \alpha \mid r \mid \alpha' \rangle$$

$$\times \sqrt{\frac{4\pi}{3}} \sum_{M'q} \begin{pmatrix} J & J' & 1 \\ 0 & M' & q \end{pmatrix} \langle J0 \mid Y_1^q(\hat{\mathbf{r}}) \mid J'M' \rangle.$$
(5.51)

The angular integrals can be computed using Weyl's theorem (see e.g. relation

(8.8) of Landi Degl'Innocenti 2014), resulting in

$$\langle \alpha J \parallel \mathbf{d} \parallel \alpha' J' \rangle = e_0 (-1)^{J'+1} \sqrt{2J'+1} \times \langle \alpha \mid r \mid \alpha' \rangle$$

$$\times \begin{pmatrix} J & J' & 1 \\ 0 & 0 & 0 \end{pmatrix} \sum_{M'q} (2J+1) \begin{pmatrix} J & J' & 1 \\ 0 & M' & q \end{pmatrix}^2.$$
(5.52)

Using properties of the 3-j symbols, it is possible to check that the sum in the previous relation is equal to 1, leading to our final result

$$\langle \alpha J \parallel \mathbf{d} \parallel \alpha' J' \rangle = e_0 (-1)^{J'+1} \sqrt{2J'+1} \begin{pmatrix} J & J' & 1 \\ 0 & 0 & 0 \end{pmatrix} \times \langle \alpha \mid r \mid \alpha' \rangle.$$
(5.53)

# 5.B Asymptotic properties of the Whittaker M function

We show that

$$\lim_{\kappa \to \infty} \kappa^{\mu + \frac{1}{2}} M_{\kappa,\mu} \left( \frac{z}{\kappa} \right) = \lim_{\kappa \to \infty} (i\kappa)^{\mu + \frac{1}{2}} M_{i\kappa,\mu} \left( -\frac{iz}{\kappa} \right)$$
$$= z^{\mu + \frac{1}{2}} {}_{0}F_{1}(1 + 2\mu; -z)$$
 (5.54)

for  $\mu \in \mathbb{C}$ . The hypergeometric function  ${}_{0}F_{1}$  is defined by the series

$$_{0}F_{1}(\gamma;z) = \sum_{k=0}^{\infty} \frac{1}{(\gamma)_{k}} \frac{z^{k}}{k!}, \quad (\gamma)_{k} \equiv \gamma(\gamma - 1)(\gamma - 2) \cdots (\gamma - k + 1), \quad (5.55)$$

and the Whittaker M function is defined by

$$M_{\kappa,\mu}(z) = \exp\left(-\frac{z}{2}\right) z^{\mu + \frac{1}{2}} {}_{1}F_{1}\left(\mu - \kappa + \frac{1}{2}, 1 + 2\mu; z\right).$$
 (5.56)

The confluent hypergeometric function  $_1F_1$  is studied in detail in Lebedev & Silverman (1965) and defined by the hypergeometric series

$$_{1}F_{1}(\alpha,\gamma;z) = \sum_{k=0}^{\infty} \frac{(\alpha)_{k}}{(\gamma)_{k}} \frac{z^{k}}{k!}, \quad \alpha,\gamma,z \in \mathbb{C}, \quad \gamma \neq 0,-1,-2,\dots$$
 (5.57)

In particular,  ${}_1F_1$  is an entire function of z and of its parameter  $\alpha$ , and a meromorphic function of  $\gamma$  with simple poles on points  $\gamma = 0, -1, -2$ , etc.

We first wish to calculate the asymptotic behaviour of  ${}_1F_1\left(a+\kappa,\gamma;\frac{z}{\kappa}\right)$  when  $\kappa\to\pm\infty$  for fixed complex numbers a and z and  $\gamma\neq0,-1,-2$ , etc. To

this aim, we use the dominated convergence theorem applied to the measure space  $(\mathbb{Z}_{\geq 0}, \Sigma, \mu)$ , with  $\Sigma = \mathcal{P}(\mathbb{Z}_{\geq 0})$  the power set of  $\mathbb{Z}_{\geq 0}$  and  $\mu$  the counting measure. With these specific choices, the dominated convergence theorem states that this limit can be computed term by term in the series expansion of  ${}_{1}F_{1}$ , as long as there exists a bounding function B(k) such that for some finite number K

$$\left| \frac{(a+\kappa)_k}{(\gamma)_k} \frac{1}{\kappa^k} \right| \le B(k) \quad \forall |\kappa| > K, \tag{5.58}$$

with B(k) independent of  $\kappa$ , and the series

$$\sum_{k=0}^{\infty} B(k) \frac{|z|^k}{k!} < \infty. \tag{5.59}$$

A bounding function like this can be found for  $|\kappa| > |a|$ ,  $|a + \kappa| > |\gamma|$  and  $|a + \kappa| > |\gamma|^2$  (we choose for example  $K = 1 + |a| + |\gamma| + |\gamma|^2$ ),

$$\left| \frac{(a+\kappa)_k}{(\gamma)_k} \frac{1}{\kappa^k} \right| = \left| \frac{1\left(1 + \frac{1}{a+\kappa}\right) \cdots \left(1 + \frac{k-1}{a+\kappa}\right)}{1\left(1 + \frac{1}{\gamma}\right) \cdots \left(1 + \frac{k-1}{\gamma}\right)} \frac{\left(1 + \frac{a}{\kappa}\right)^k}{\gamma^k} \right|$$

$$\leq \sup_{n \in \mathbb{Z}_{\geq 0}} \left( \left| \frac{1 + \frac{n}{a+\kappa}}{1 + \frac{n}{\gamma}} \right| \right)^k \frac{2^k}{|\gamma|^k} \quad (\gamma \neq 0, -1, -2, \dots)$$

$$= \sup_{n \in \mathbb{Z}_{\geq 0}} \left( \left| \left(\gamma - \frac{\gamma^2}{a+\kappa}\right) \frac{1}{n+\gamma} + \frac{\gamma}{a+\kappa} \right| \right)^k \frac{2^k}{|\gamma|^k}$$

$$\leq \sup_{n \in \mathbb{Z}_{\geq 0}} \left( \left( |\gamma| + \frac{|\gamma|^2}{|a+\kappa|} \right) \frac{1}{|n+\gamma|} + \frac{|\gamma|}{|a+\kappa|} \right)^k \frac{2^k}{|\gamma|^k}$$

$$\leq \left( \frac{1 + |\gamma|}{d(-\gamma, \mathbb{Z}_{\geq 0})} + 1 \right)^k \frac{2^k}{|\gamma|^k}$$

$$= \left( \frac{2}{|\gamma|} \left( 1 + \frac{1 + |\gamma|}{d(-\gamma, \mathbb{Z}_{\geq 0})} \right) \right)^k$$

$$\equiv B(k) \equiv cB^k,$$
(5.60)

where with this bound c=1, and we have defined the distance function for  $z \in \mathbb{C}$  and  $E \subset \mathbb{C}$  to be given by

$$d(z, E) \equiv \inf_{w \in E} (|z - w|). \tag{5.61}$$

With the bound B(k), it is clear that Eq. (5.59) is satisfied:

$$\sum_{k=0}^{\infty} B(k) \frac{|z|^k}{k!} = c \sum_{k=0}^{\infty} B^k \frac{|z|^k}{k!} = c \cdot \exp(B|z|) < \infty, \tag{5.62}$$

but we note that in the relevant case in which  $\gamma \geq 2$  (corresponding to the angular momentum  $l \geq 0$ ), K could be chosen even greater, and with c = 3/2, it is possible to find a similar bound for which B is arbitrarily close to 1/3 (this bound is not required for the present proof, but will be useful later). The limits, term by term in the series expansion of  ${}_{1}F_{1}$ , are finally given by

$$\lim_{\kappa \to \pm \infty} \frac{(a+\kappa)_k}{(\gamma)_k} \frac{1}{\kappa^k} = \frac{1}{(\gamma)_k},\tag{5.63}$$

and by application of the dominated convergence theorem

$$\lim_{\kappa \to \pm \infty} {}_{1}F_{1}\left(a + \kappa, \gamma; \frac{z}{\kappa}\right) = \sum_{k=0}^{\infty} \frac{1}{(\gamma)_{k}} \frac{z^{k}}{k!} \equiv {}_{0}F_{1}(\gamma; z). \tag{5.64}$$

The same reasoning with the same bound, but substituting  $\kappa \to i\kappa$ , provides a proof of

$$\lim_{\kappa \to \pm \infty} {}_{1}F_{1}\left(a + i\kappa, \gamma; -\frac{iz}{\kappa}\right) = {}_{0}F_{1}(\gamma; z). \tag{5.65}$$

The proof of Eq. (5.54) then follows by substituting  $\kappa \to -\kappa$  (and  $\kappa \to -i\kappa$ , respectively),  $z \to -z$ ,  $a \to \mu + \frac{1}{2}$  and  $\gamma \to 1 + 2\mu$  in Eqs. (5.64) and (5.65), and inserting the resulting limits in Eq. (5.56).

We note that choosing 1/3 < B < 1/2 further allows us to prove that the wavefunctions of the bound/free electrons are bounded independently of  $n_u$  and  $\varepsilon$  and that the wavefunction of the bound electron is (asymptotically) exponentially decreasing. It is indeed straight-forward to check with this bound that  $_1F_1$  in Eq. (5.56) grows more slowly than  $\exp(z/2)$ , allowing an exponential decay of the Whittaker M function in Eq. (5.56). Hence the integrands inside the radial integrals (5.19) and (5.21) are also bounded and (asymptotically) exponentially decreasing. Using again the dominated convergence theorem, we can further justify the interchange of the limits  $n_u \to \infty$  (and  $\varepsilon \to 0$  respectively) and the radial integrals.

Acknowledgements. We are grateful to Edgar S. Carlin for his help with the computation of the reduced matrix elements of the dipole operator, and to Jhih-Huang Li for his revision of the derivations of the asymptotic properties of the Whittaker M function. We are also very grateful to Jiří Štěpán and Roberto Casini for a preliminary reviewing of this work and for providing new ideas and useful feedback, as well as to Javier Trujillo Bueno for inspiring discussions. We also acknowledge the referee's valuable and encouraging input. This work was supported by the Swiss National Science Foundation under grant ID 200020\_157103/1.

Note added in proof. We call the reader's attention to the fact that Menzel & Pekeris (1935) and references therein studied the limit  $n_u \to \infty$  for the wavefunction of the bound electron and came to the conclusion that there was exact continuity of the absorption coefficient at the Balmer limit. In the present paper, we used the modern formalism of Landi Degl'Innocenti & Landolfi (2004) to prove continuity.

### **Bibliography**

- Abramowitz, M. & Stegun, I. 1964, Handbook of Mathematical Functions: With Formulas, Graphs, and Mathematical Tables, Applied mathematics series (Dover Publications)
- Bethe, H. A. & Salpeter, E. E. 1957, Quantum Mechanics of One- and Two-Electron Atoms (New York: Academic Press)
- Burgess, A. & Seaton, M. J. 1960, "A general formula for the calculation of atomic photo-ionization cross-sections", MNRAS, 120, 121
- Gordon, W. 1929, "Zur Berechnung der Matrizen beim Wasserstoffatom", Ann. Phys., **394**, 1031
- Griem, H. R. 1960, "Stark Broadening of Higher Hydrogen and Hydrogen-Like Lines by Electrons and Ions.", ApJ, 132, 883
- Griffiths, D. J. 1995, Introduction to Quantum Mechanics (Prentice Hall)
- Lanczos, C. 1931, "Zur Intensitätsschwächung der Spektrallinien in hohen elektrischen Feldern", Z. Phys., **68**, 204
- Landi Degl'Innocenti, E. 2014, Atomic Spectroscopy and Radiative Processes (Springer-Verlag)
- Landi Degl'Innocenti, E. & Landolfi, M. 2004, Astrophysics and Space Science Library, Vol. 307, *Polarization in Spectral Lines* (Kluwer Academic Publishers)
- Lebedev, N. & Silverman, R. 1965, Special Functions and Their Application, Selected Russian publications in the mathematical sciences (Englewood Cliffs)
- Menzel, D. H. 1964, "Generalized Radial Integrals With Hydrogenic Functions", Rev. Mod. Phys., 36, 613
- Menzel, D. H. & Pekeris, C. L. 1935, "Absorption coefficients and hydrogen line intensities", MNRAS, 96, 77

Morabito, L. K., van Harten, G., Salgado, F., et al. 2014, "Exact bound-bound Gaunt factor values for quantum levels up to n = 2000", MNRAS, 441, 2855 [arXiv:1407.5784]

- Seaton, M. J. 1958, "The Quantum Defect Method", MNRAS, 118, 504
- Stenflo, J. O. 2005, "Polarization of the Sun's continuous spectrum", A&A, 429, 713

# Polarization in the continuum

### Centre-to-limb variation

#### Contents

6.1	l Introd	Introduction				
6.2	2 The p	hysics and equations				
	6.2.1	Generalities				
	6.2.2	Scattering and non-scattering processes 109				
	6.2.3	Methods used for the solution of the equations $\dots$ . 111				
6.3	3 Observ	vational data and 1D models				
	6.3.1	Temperature structure				
	6.3.2	Limb-darkening				
	6.3.3	Centre-to-limb variation of polarization 117				
6.4	4 The co	ontinuum from 3D models				
	6.4.1	Polarization maps at disc centre				
	6.4.2	Limb-darkening				
	6.4.3	Centre-to-limb variation of polarization				
	6.4.4	The contribution of the far red wing of Lyman- $\beta$ 125				
6.5	5 Discus	scussion and conclusions				
Bi	bliograph	y				

### 6.1 Introduction

In this chapter we apply the tools presented in Section 2.3 to our high-resolution 3D models described in Sect. 2.1.5, in order to produce polarization maps of the quiet solar photosphere at a variety of heliocentric angles for a set of chosen continuum wavelengths in the visible. We also derive a curve of the average linear polarization versus the heliocentric angle (ie. the centre-to-limb variation of the polarized continuum), for a chosen set of wavelengths.

There are multiple aims to this investigation. The unavoidable instrumental cross-talk  $I \to Q$  results in an offset of the zero level of the fractional polarization Q/I (see e.g. Stenflo et al. 1997). A first aim is to provide synthetic observations that could be used to develop an accurate calibration strategy. At the present time, a natural assumption is used for the calibration of spectropolarimeters: the polarization at disc centre is zero. Since the Sun exhibits, in a good approximation, cylindrical symmetry along the line-of-sight when pointing at disc centre, this assumption is reasonable. However, with accurate instrumentation capable of measuring extremely small levels of polarization and with the expected spatial resolution capabilities of upcoming solar telescopes such as the 4 m Daniel K. Inouye Solar Telescope (DKIST, see Keil et al. 2010) or the 4 m European Solar Telescope (EST, see Collados et al. 2010), the calibration methods will have to be revised.

At a more fundamental level, the linear polarization exhibits a centre-tolimb variation that is different but complementary to limb-darkening. While limb-darkening is closely related to temperature gradients in the solar atmosphere, the centre-to-limb variation of linear polarization is also extremely sensitive to the anisotropy of the radiation field in the presence of scattering processes.

The general problem of radiative equilibrium in stellar atmospheres was gradually tackled by Chandrasekhar in a series of twenty-four papers published in-between the years 1944 and 1948. In one of these contributions, Chandrasekhar (1946) considers the polarized radiative transfer equations allowing for scattered radiation in accordance with Rayleigh's law, well before the present formalism for polarized radiation was developed. These investigations were eventually gathered in Chandrasekhar (1960), in which quantities like the centre-to-limb variation of linear polarization in fully scattering atmospheres were analytically studied.

The theoretical pioneering work of Chandrasekhar on the scattering of polarized light in stellar and planetary atmospheres enabled, together with the development of sophisticated computational tools, the study of realistic atmospheres like the solar photosphere studied here. The polarized solar continuum has already been modelled by e.g. Fluri & Stenflo (1999), and its centre-to-limb variation was also semi-empirically determined later, with the help of a model for depolarizing lines (Stenflo 2005), which however displays a lower polarization than previously modelled. The centre-to-limb variation of the polarization in the solar continuum has also been observed by Wiehr & Bianda (2003), who found an excellent match with the FAL-C model of Fluri & Stenflo (1999). More recently, 3D radiative transfer has been carried out in order to produce a more realistic modelling taking into account symmetry-breaking effects caused by horizontal inhomogeneities arising from surface convection (Trujillo Bueno & Shchukina 2009). This later contribution showed a remarkable agreement with the semi-empirical data of Stenflo (2005), which was believed to be sig-

6.1. Introduction 105

nificantly better than that obtained via the use of 1D models.

Independently, Kostogryz & Berdyugina (2015) and Kostogryz et al. (2016) studied in detail, with 1D modelling, the centre-to-limb variation of polarization and intensity for stars of F, G and K spectral type, including the Sun, and they compared their results with the ones of the work of Fluri & Stenflo (1999) and Stenflo (2005). An important and new contribution was the consideration of spherical atmospheres in the calculation of polarized radiative transfer in the continuum, which is required for an accurate modelling close to the stellar limb. A new bridge between stellar physics and exoplanet research was also established in Kostogryz et al. (2015), in which the polarimetric effect of exoplanets transiting in front of their star was studied, as well as the effect of starspots and starspot-crossing during transits. It was found that the polarization parameters are sensitive to spot sizes and positions, they reveal the rotation period independently of spot-crossing events, and they provide parameters like the spatial orientation of the orbit of the exoplanet, which cannot be derived with photometrical techniques. The minimal polarimetric sensitivity required for these studies is however about one order of magnitude higher than the one provided by the existing instruments on bright targets, so that the effective application of these new techniques will have to be delayed until a new generation of spectropolarimeters is available. The symmetry breaking leading to a linear polarization signal from an unresolved star that is either rapidly rotating or masked by a binary companion or a transiting planet was also reported in the proceeding of Harrington (2015).

In the present chapter we carry out 3D modelling at high spatial resolution as well as 1D modelling, and we try to quantify the effects of horizontal inhomogeneities as compared to the effects arising from using different model atmospheres and/or different methods and approximations for the computation of scattering and non-scattering opacities. This task is non-trivial, since 3D models do not intrinsically offer natural 1D "equivalent" models: we will see that there are different ways of reducing a 3D model to a 1D "equivalent" model, and we will attempt a "natural choice". 3D models can also be compared to semi-empirical 1D models that typically have different temperature structures. One major difficulty in this investigation is that the work previously carried out by different scientists is not exactly reproducible, since we lack the codes, the models, and the exact opacities that were initially used. For this reason it is not straight forward to determine which of these factors (if not all of them) are responsible for the mismatches of the observables (e.g limbdarkening curves, centre-to-limb variation of polarization, polarization spectra, etc.).

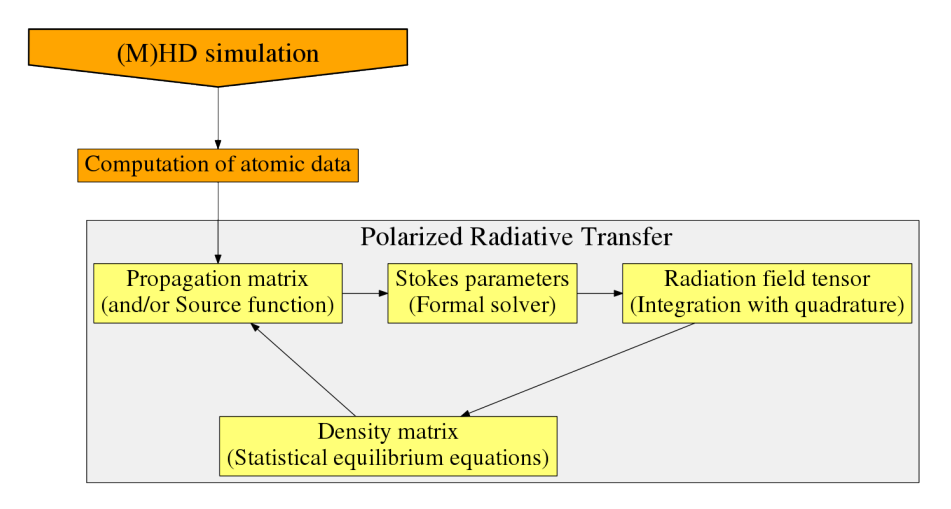


**Figure 6.1.** Schematic description of the general non-LTE computational pipeline: from (M)HD simulations to synthetic observations.

# 6.2 The physics and equations governing the polarized continuum

#### 6.2.1 Generalities

The polarized continuum is mainly determined by the scattering processes. The underlying physics and the statistical treatment used to derived the corresponding cross-sections and the equations for radiative transfer were briefly discussed on Sec. 2.2 from a general perspective, and were subsequently employed for the polarized light of the solar continuum in Sec. 2.3. Here we make a list of the relevant tools and final equations that are directly used in the *Polarized RAdiative Transfer In the Continuum* (PRATIC) module we specifically wrote for the *Polarized Radiative TrAnsfer* (PORTA) code of Štěpán & Trujillo Bueno (2013).

The pipeline displayed in Fig. 6.1 schematically shows the different steps involved in the generation of spectropolarimetric synthetic observations. As a first step, radiative (M)HD simulations are required, as well as the atomic data involved in the computation of the Einstein coefficients that later appear in the evolution equation of the atomic system (the statistical equilibrium equations). Ideally, the atomic data used in the computation of derived quantities (e.g. temperature) from the (M)HD simulations (opacities and abundances used to derive the equation of state) should be consistent with the atomic data used in the polarized radiative transfer calculations.

The statistical equilibrium equations coupled with the formal polarized radiative transfer equations constitute a non-linear system. The last step in

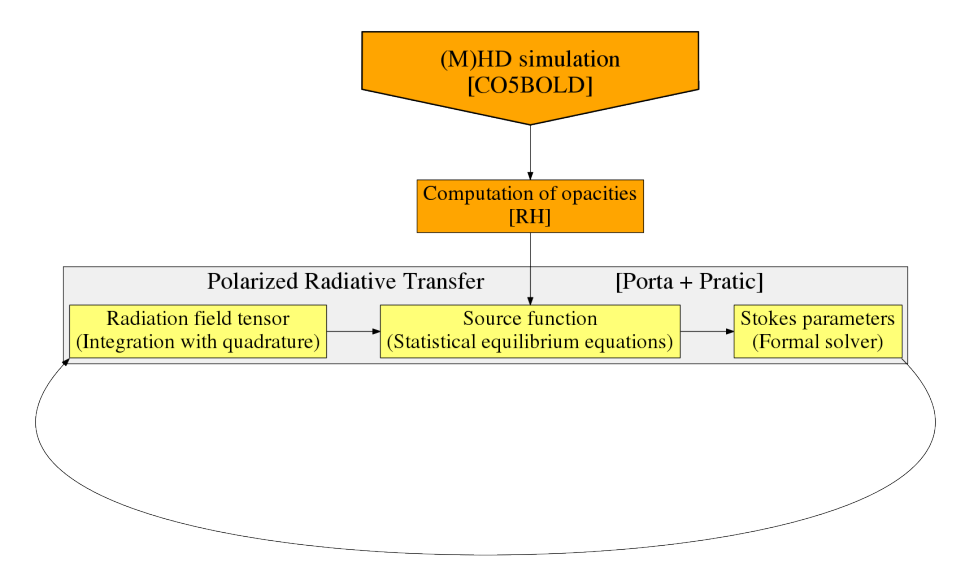


Figure 6.2. Schematic description of simplified non-LTE computational pipeline for the computation of the continuum radiation.

which the 3D polarized radiative transfer is performed (grey box in Fig. 6.1) is an iterative process. In the context of polarized radiative transfer in the continuum, the statistical equilibrium equations can be solved analytically (Eq. (2.47)) and directly inserted into the expression for the coefficients of the propagation matrix, which provide the source function of Eq. (2.33). This procedure simplifies the pipeline in the context of continuum radiation, which is updated in Fig. 6.2.

The iterative pipeline of Fig. 6.2 is a non-LTE pipeline, since the source function is recalculated at each step and is not the one given by the Plack function (in which case polarization would be in-existent). This is because scattering processes are intrinsically non-LTE processes. However, the opacities appearing in the middle orange box of the figure are calculated under LTE conditions and are kept unchanged at each iteration. In the following we summarize the relevant equations, that correspond to each of the yellow boxes of the iterative loop shown in Fig. 6.2.

At first, the source function is taken to be the Planck function for intensity and zero for the other components of the Stokes vector. In the successive operations it is updated from the radiation field tensor by using the equations (2.33) that we rewrite here:

$$S_I = \frac{\eta_I^{ns}}{\eta_I^{ns} + \eta_I^s} B_{\nu}(T) + \frac{\eta_I^s}{\eta_I^{ns} + \eta_I^s} \left[ J_0^0 + \frac{1}{2\sqrt{2}} \left( 3\mu^2 - 1 \right) J_0^2 \right]$$

$$-\sqrt{3}\mu\sqrt{1-\mu^{2}}\left(\cos\left(\chi\right)\hat{J}_{1}^{2}+\sin\left(\chi\right)\hat{J}_{1}^{2}\right) + \frac{\sqrt{3}}{2}\left(1-\mu^{2}\right)\left(\cos\left(2\chi\right)\hat{J}_{2}^{2}+\sin\left(2\chi\right)\hat{J}_{2}^{2}\right)\right],$$

$$S_{Q} = \frac{\eta_{I}^{s}}{\eta_{I}^{ns}+\eta_{I}^{s}}\left[\frac{3}{2\sqrt{2}}\left(\mu^{2}-1\right)J_{0}^{2}-\sqrt{3}\mu\sqrt{1-\mu^{2}}\left(\cos\left(\chi\right)\tilde{J}_{1}^{2}+\sin\left(\chi\right)\hat{J}_{1}^{2}\right) - \frac{\sqrt{3}}{2}\left(1+\mu^{2}\right)\left(\cos\left(2\chi\right)\tilde{J}_{2}^{2}+\sin\left(2\chi\right)\hat{J}_{2}^{2}\right)\right],$$

$$S_{U} = \frac{\eta_{I}^{s}}{\eta_{I}^{ns}+\eta_{I}^{s}}\left[\sqrt{3}\sqrt{1-\mu^{2}}\left(\sin\left(\chi\right)\tilde{J}_{1}^{2}+\cos\left(\chi\right)\hat{J}_{1}^{2}\right) + \sqrt{3}\mu\left(\sin\left(2\chi\right)\tilde{J}_{2}^{2}+\cos\left(2\chi\right)\hat{J}_{2}^{2}\right)\right].$$

$$(6.1)$$

The absorption coefficients  $\eta_I^s$  and  $\eta_I^{ns}$  refer to the scattering and non-scattering contributions respectively;  $\mu$  is the cosine of the heliocentric angle and  $\chi$  is the azimuthal angle;  $J_Q^K$  are the components of the radiation field tensor, with real parts denoted by a tilde and imaginary parts denoted by a hat. The radiative transfer Eq. (2.34) then reads

$$\frac{\mathrm{d}}{\mathrm{d}\tau}I = I - S_I,\tag{6.2}$$

and I stands for any of the Stokes components. Here,  $\tau$  is the monochromatic optical depth along the integration ray, so that  $d\tau = \chi_c ds$  for  $\chi_c = \eta_I^{ns} + \eta_I^s$ . We refer to the part of the code that solves these equations assuming a known source function as the *formal solver*. The formal solver integrates the radiative transfer equation along a finite number of directions provided by a chosen quadrature. Finally, the Stokes vector is integrated in Eq. (2.35) over all directions of the quadrature in order to provide the radiation field tensor:

$$\begin{split} J_0^0 &= \oint \frac{\mathrm{d}\Omega}{4\pi} I_{\nu\vec{\Omega}}, \\ J_0^2 &= \oint \frac{\mathrm{d}\Omega}{4\pi} \frac{1}{2\sqrt{2}} \left[ \left( 3\mu^2 - 1 \right) I_{\nu\vec{\Omega}} + 3 \left( \mu^2 - 1 \right) Q_{\nu\vec{\Omega}} \right], \\ J_1^2 &= \oint \frac{\mathrm{d}\Omega}{4\pi} \frac{\sqrt{3}}{2} \sqrt{1 - \mu^2} \exp\left( \mathrm{i}\chi \right) \left[ -\mu \left( I_{\nu\vec{\Omega}} + Q_{\nu\vec{\Omega}} \right) - \mathrm{i}U_{\nu\vec{\Omega}} \right], \\ J_2^2 &= \oint \frac{\mathrm{d}\Omega}{4\pi} \frac{\sqrt{3}}{4} \exp\left( 2\mathrm{i}\chi \right) \left[ \left( 1 - \mu^2 \right) I_{\nu\vec{\Omega}} - \left( 1 + \mu^2 \right) Q_{\nu\vec{\Omega}} - 2\mathrm{i}\mu U_{\nu\vec{\Omega}} \right]. \end{split}$$
(6.3)

The iterative loop restarts by inserting the radiation field tensor into Eq. (6.1), and it is only terminated when the difference in  $J_0^0$  between two successive steps drops below a chosen threshold. The present description is however purely formal. At the numerical level, the direct use of this strategy would be

equivalent to a generalization of the Λ-iteration; it would have a poor convergence, the criteria to decide whether to terminate the iteration or not would be insufficient, and the cumulated round-off errors after convergence would be significant. In practice, a variation of the accelerated Λ-iteration is used by PORTA (described in the context of radiative transfer in e.g. Trujillo Bueno & Manso Sainz 1999; Manso Sainz & Trujillo Bueno 2003; Štěpán & Trujillo Bueno 2011, 2013).

Before numerically solving Eqs. (6.1) to (6.3) for a given model atmosphere, we note that some insight is already provided by the equations alone. First of all, in the radiative transfer equation (6.2), all Stokes components are decoupled. This is a peculiarity of the continuum, for which the propagation matrix is diagonal. This means that the usual Eddington-Barbier relation for the emergent intensity  $I_{\rm out}$ 

$$I_{\text{out}} \approx S_I(\mu = 0)$$
 (6.4)

can in principle also be applied to Stokes Q and Stokes U. The Eddington-Barbier relation is justified from the explicit solution of (6.2),

$$I_{\text{out}} = \frac{1}{\mu} \int_0^\infty S_I(t) \exp\left(-\frac{t}{\mu}\right) dt.$$
 (6.5)

Indeed, assuming that the source function is given by it's Taylor expansion, the emerging intensity (and the emerging polarization components Q and U respectively) are given by

$$I_{\text{out}} = \sum_{k=0}^{\infty} \mu^k \frac{\mathrm{d}^k}{\mathrm{d}t^k} S_I(t=0),$$
 (6.6)

which correspond exactly to the series expansion of the source function around t=0 evaluated at  $t=\mu$ , except for the missing 1/k! factor. For k=0 and k=1 this factor is 1, and the approximation is equivalent to assuming the source function to be a first-order polynomial in the region  $t \in [0; \mu]$ .

# 6.2.2 The role played by scattering and non-scattering processes

A list of all scattering and non-scattering contributions considered in this work was provided in Sec. 2.2.4. We use routines of the RH code (Uitenbroek 1998) to compute the corresponding absorption coefficients of all of these contributions in LTE. A simple and qualitative way of estimating the contribution of each physical process to the emerging intensity and polarization is to compare their corresponding absorption coefficients as a function of optical depth  $\tau$  inside a 1D model. To this aim we chose the FAL-C model of Fontenla

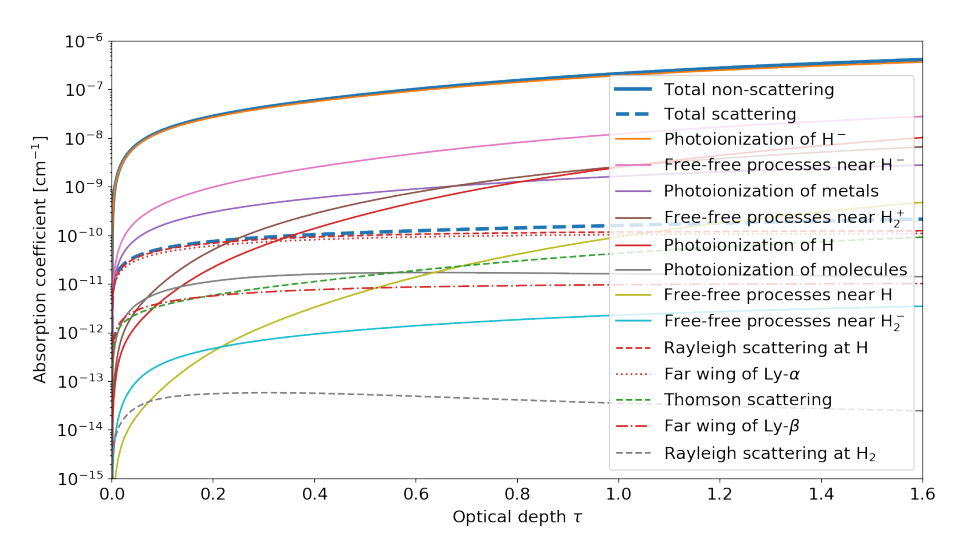


Figure 6.3. Absorption coefficients as a function of monochromatic optical depth for a number of atomic processes, at a wavelength of 5350 Å. Non-scattering processes are represented by solid lines and scattering processes are represented by dashed lines. In the legend, they are ordered from top to bottom in descending order of absorption coefficient at  $\tau=0.4$ . Bold lines correspond to the total non-scattering and scattering absorption coefficients respectively. Rayleigh scattering at H includes the far wings of the spectral lines of the Lyman series. Note that the curve corresponding to the total non-scattering absorption coefficient overlaps with the curve corresponding to photoionization of  $H^-$ .

et al. (1993) as it was also used by Fluri & Stenflo (1999), and we plotted the absorption coefficient of different atomic processes versus optical depth in Fig. 6.3.

As expected, at optical wavelengths, the non-scattering absorption coefficient contributes most to the total absorption coefficient (by several orders of magnitude), and the absorption coefficient due to the photoionization of  $H^-$  fully dominates the various non-scattering absorption coefficients. A close examination of Eq. (6.1) suggests that only the first term (proportional to the fraction of non-scattering absorption) of the source function for the intensity,  $S_I$ , significantly contributes, since the second term (proportional to the fraction of scattering absorption) is expected to be much smaller. However, the source functions for linear polarization  $S_Q$  and  $S_U$  do not have a term proportional to the fraction of non-scattering absorption. This means that even though the scattering absorption coefficient is orders of magnitude smaller than the total absorption coefficient, it determines the linearly polarized signal.

We also note that, at  $\tau=0.15$  and higher up in the atmosphere, the contribution of the far wing of Lyman- $\beta$  to the total scattering absorption coefficient is more important than the Thomson absorption coefficient. In

particular, the formula of Baschek & Scholz (1982) for Rayleigh scattering,

$$\sigma_R \approx \sigma_T \left(\frac{966}{\lambda}\right)^4 \left[1 + \left(\frac{1566}{\lambda}\right)^2 + \left(\frac{1480}{\lambda}\right)^4\right],$$
 (6.7)

in which  $\lambda$  is expressed in Å and  $\sigma_T$  is the Thomson cross-section, is a very accurate approximation for the scattering cross-section due to the far wing of Lyman- $\alpha$ , but does not include the far wings of the successive lines of the Lyman series. As we shall see in Sec. 6.4.4, ignoring these further contributions leads to inaccurate modelling of the linear polarization.

#### 6.2.3 Methods used for the solution of the equations

The POlarized Radiative TrAnsfer (PORTA) framework of Stěpán & Trujillo Bueno (2013) is used in order to solve the non-LTE polarized radiative transfer (RT) equations. The PORTA code implements different schemes for the main iteration loop; we use a Jacobian-based method. The PORTA code also implements a short-characteristics formal solver (Kunasz & Auer 1988) for which a variety of interpolation methods are available. Two different interpolations are required when using a short-characteristics scheme. First, the radiation transfer quantities (the components of the propagation matrix and of the emission vector) need to be obtained, when integrating along the short characteristic, in the upwind and downwind points. Then, the source function needs to be interpolated along the short characteristic for explicit integration. For the present problem, we configured the PORTA code in order to make a bilinear 4-point interpolation for the radiative transfer quantities (less accurate than the biquadratic interpolation but in principle sufficient for fine enough grids) and a quadratic monotonic Bézier interpolation along the short characteristic for the source function.

In addition, the PORTA framework implements the Gaussian quadratures for a given number of declination and azimuthal angles in order to perform the integrals over the sphere that appear in Eq. (6.3). Useful quantities as the tensor  $\mathcal{T}_Q^K$  appearing in the formalism of Landi Degl'Innocenti & Landolfi (2004) are also defined. But one of the most important features of PORTA is its efficient parallelization strategy, using the Message Passing Interface (MPI) standard.

Since PORTA is a flexible framework for the polarized radiative transfer in a variety of physical situations, the physics itself is not present in the framework. For instance, PORTA cannot compute the source function (Eq. (6.1) in the present context), it cannot solve the statistical equilibrium equations, and it has no knowledge of the integrand in the defining equations of the radiation field tensor of Eq. (6.3). However, it provides the prototypes of the corresponding routines. These routines must be defined in an external module that

appears to PORTA as a shared library. The external module is linked with the PORTA library, enabling in this way all the tools and definitions available in the PORTA library. Since the input and output data relevant for the calculations also depend on the physical problem, the PORTA module must also include two routines for the encoding and decoding of node data.

For the specific problem presented in this chapter, we wrote the *Polarized RAdiative Transfer In the Continuum* (PRATIC) module for the PORTA code. Since all scattering and non-scattering absorption coefficients are computed in LTE (meaning that they do not need to be updated at each Jacobi iteration), we decided to include them in the input node data that is loaded by PORTA. The calculation of these absorption coefficients and the synthesis of the input PORTA box from the CO<sup>5</sup>BOLD data is then an independent step, that is dealt with by a secondary MPI-parallel code (*ltebackgrmpi*) that we wrote for this specific purpose.

Itebackgrmpi is essentially a wrapper for the RH routines that we borrow from the RH code of Uitenbroek (1998). It additionally implements a queue of MPI threads: since the calculation of absorption coefficients is a local problem, the pixels of the 3D box are segmented into chunks by a master process, and are sent to the next free thread waiting in the queue. When a thread has finished its job, it sends the computed data back to the master and declares itself free again. There are two kind of jobs, "computing" jobs and "writing" jobs. The former kind of jobs are run concurrently, whereas a lock ensures that the latter kind of jobs are run sequentially. Whenever the three conditions 1) the lock is unset (no writing is going on), 2) the master has received data to write and 3) a thread declares itself free are fulfilled, the master allocates a "writing" job for the free thread.

The main drawback of the PORTA code and the *ltebackgrmpi* module is the amount of memory used. Loading one of our CO<sup>5</sup>BOLD models already requires 7.7 G, and a PORTA box additionally contains all components of the radiation field tensor, for each frequency. For this reason, we were constrained to store one single frequency per PORTA box.

### 6.3 Observational data and 1D models

At the present time, Wiehr (1978) and Wiehr & Bianda (2003) provide the only available measured data of the centre-to-limb variation of polarization in the continuum. Older measurements as those of Leroy (1972) and Mickey & Orrall (1974) are also available, but they were carried out with filters on bands larger than 10 Å that either fail to accurately isolate the continuum from spectral lines or are subject to instrumental problems. New measurements are presently carried out at the "Istituto Ricerche Solari Locarno" (IRSOL) and the choices of wavelengths and heliocentric angles that were made for these

new measurements determined our choices for the synthesis of polarization data from our 3D models.

From a 1D-modelling perspective, the polarized solar continuum has been extensively studied by Fluri & Stenflo (1999). An interesting conclusion was that the model dependence of the continuum polarization is mainly due to the different limb-darkening curves appearing from model to model; among the many 1D models they studied, only the two models for which the chromosphere was playing a sensible contribution constituted an exception to this rule. Fluri & Stenflo (1999) also provided a semi-empirical formula for the linear polarization in terms of limb-darkening,

$$\frac{Q_{\lambda}}{I_{\lambda}}(\mu) = q_{\lambda} \frac{1 - \mu^2}{(\mu + m_{\lambda}) I_{\lambda}(\mu) / I_{\lambda}(1)}, \tag{6.8}$$

in which  $\log(q_{\lambda}) = a_0 + a_1\lambda + a_2\lambda^2$  is a quadratic polynomial in  $\lambda$  whose coefficients  $a_i$  were fitted for each model, and  $m_{\lambda}$  is a one-degree polynomial in  $\lambda$  with model-independent coefficients. Since our (M)HD simulations do not include all the physics required for the simulation of the chromosphere, and we perform radiative transfer in LTE, all possible chromospheric effects are likely to be missing or inaccurate. It however makes sense to compare our 3D modelling to most of the 1D modelling of Fluri & Stenflo (1999), in which there are no significant chromospheric effects. In order to produce a semi-empirical reference curve, we inserted the parameters corresponding to the FAL-C model into Eq. (6.8), and the observed limb-darkening curve of Neckel & Labs (1994).

With the same purpose of producing a semi-empirical reference curve, Stenflo (2005) uses the Atlas of the Second Solar Spectrum (Gandorfer 2000, 2002, 2005) and relies on a model for the behaviour of the depolarizing lines. Since all the data provided by the atlas is measured at the solar limb ( $\mu = 0.1$ ), Stenflo (2005) makes use of Eq. (6.8) in order to extract  $q_{\lambda}$ . We remind that  $m_{\lambda}$  is determined in Fluri & Stenflo (1999) and it is assumed to be modelindependent. Furthermore, Stenflo (2005) uses the limb-darkening curve of Neckel (1996), and in this way he obtains semi-empirical centre-to-limb variation of polarization curves for  $Q_{\lambda}/I_{\lambda}$  through Eq. (6.8).

For the intensity, the available data that we consider in the following is the limb-darkening curves of Neckel & Labs (1994) and of Neckel (1996). For polarization, we consider the observations of Wiehr & Bianda (2003) and the semi-empirical data derived from Eq. (6.8), by using the parameters for the FAL-C model that are available in Fluri & Stenflo (1999) with the above-mentioned limb-darkening curves.

By replicating the data from 1D models within a column of  $3 \times 3$  grid cells into the horizontal directions, we build 3D plane-parallel models, for which radiative transfer can be carried out in exactly the same way as done for the full 3D models. We repeat the calculations of Fluri & Stenflo (1999) for their

interpolation of the FAL-C model, and we generate 1D models from our (M)HD cubes, by averaging temperature and density either on horizontal planes or on isosurfaces of constant bolometric optical depth  $\tau$ .

#### **6.3.1** Temperature structure

The 1D models from which we perform polarized radiative transfer computations are

- FALC390, the model interpolated to 390 grid points by Fluri & Stenflo (1999) from the original model of Fontenla et al. (1993) with with 72 grid points,
- v50-flat, obtained by averaging the snapshot d3gt57g44v50fc.134051 of our CO<sup>5</sup>BOLD models over horizontal planes,
- v50-iso, obtained by averaging the snapshot d3gt57g44v50fc.134051 over isosurfaces of constant bolometric optical depth  $\tau$ ,
- roe-flat, obtained by averaging the magnetic field-free snapshot d3gt57g44roefc.56016 of our CO<sup>5</sup>BOLD models over horizontal planes,
- roe-iso, obtained by averaging the snapshot d3gt57g44roefc.56016 over isosurfaces of constant bolometric optical depth  $\tau$ .

The averaging procedure on isosurfaces of constant bolometric optical depth  $\tau$  is performed as follows: 1) determine the average optical depth  $\langle \tau \rangle_z$  on all horizontal planes z, 2) determine the average height  $\langle h \rangle_{\langle \tau \rangle_z}$  of the isosurfaces of constant  $\langle \tau \rangle_z$  and remove all points for which the corresponding isosurfaces overflows out of the box, 3) interpolate with a spline the points  $(\langle h \rangle_{\langle \tau \rangle_z}, \log(\langle \tau \rangle_z))$  at the vertical grid-coordinates z, hence obtaining the points  $(z, \log(\tau_z))$ .

This procedure guarantees that, in a very good approximation, the average height of the isosurface of constant  $\tau_z$  is precisely z (empirically, the absolute error between these two quantities is below 1 m for all isosurfaces, on a 2800 km heigh box). The CO<sup>5</sup>BOLD output variables (e.g. density and internal energy) are then linearly interpolated on those isosurfaces and their averages are used in order to compute temperature through the equation of state. The computation of opacities and radiative transfer are performed in the same way as with the FALC390 1D model atmosphere.

The variables used by the RH routines in order to compute opacities are density and temperature, which are derived quantities (i.e. they require the use of the equation of state in order to be determined from the output simulation data). We must note here that spatial averaging and the application of the equation of state are non-commuting operations. Fig. 6.4 shows that the order matters when the spatial averages are taken over horizontal planes, whereas it

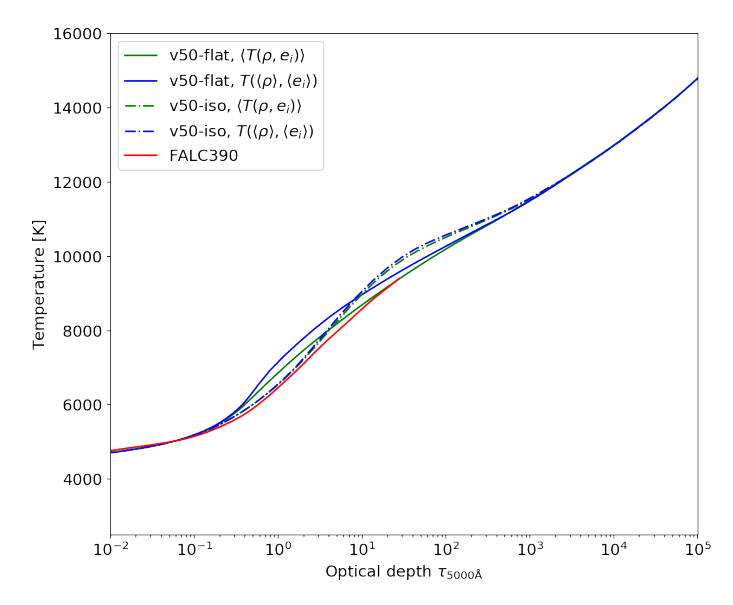


**Figure 6.4.** Spatially averaged temperatures of the snapshot d3gt57g44v50fc.134051, using different averaging methods. Solid curves represent flat averages over horizontal planes, whereas dot-dashed curves represent averages over isosurfaces of constant optical depth. Green curves provide direct averaging of temperature, whereas the blue curves refer to temperatures computed from the averaged density and internal energy.

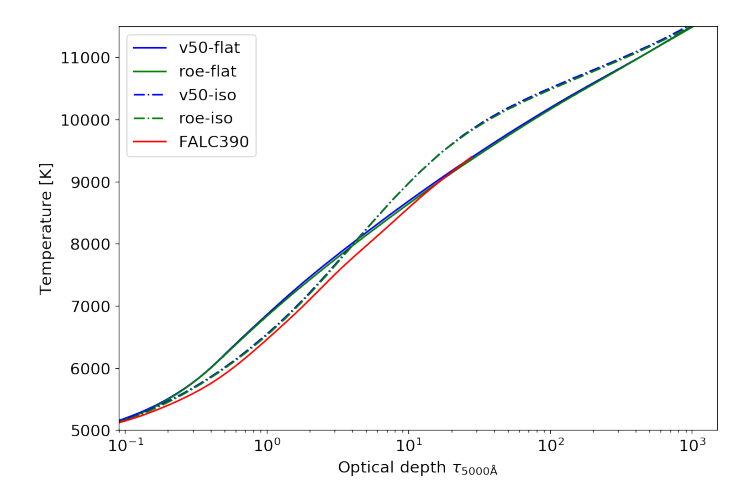


Figure 6.5. Comparison of the temperature structure of the considered 1D models.

is less significant when spatial averages are computed on surfaces of constant optical depth. In the following, density and temperature are first computed from internal quantities by using the equation of state, and spatial averages are taken as a subsequent step over density and temperature, either on horizontal planes or on surfaces of constant bolometric optical depth  $\tau$ . The way averages, interpolations, calculations of opacities, and calculations of optical depths are performed, all affect the temperature structure of the model. It is therefore crucial to enforce a consistent computation of those quantities among all the model atmospheres.

Since radiative transfer codes do not usually need an optical depth scale, such a scale is given here using separate routines. It is then crucial to calculate it in a consistent way: both density and temperature should be averaged in the very same manner. Two 1D models computed from the same 3D model will have different optical depth scales, when the averaging was done differently. In Fig. 6.4, the computation of isosurfaces on which physical quantities are averaged is done at constant bolometric optical depth  $\tau$ . However, the depth scale of the x-axis is chosen to be the monochromatic optical depth at a wavelength of 5000 Å. The density and temperature were consistently averaged in order to compute the optical depth scale.

From Fig. 6.5 we observe that on depths where the monochromatic optical depth is close to unity, the averaged temperature over isosurfaces of constant bolometric optical depth has better agreement with the corresponding temperature structure of the FALC390 model than the averaged temperature on horizontal layers. At deeper depths, our 1D models with isosurface averaging exhibit a temperature bump that is much less pronounced or in-existent in the FALC390 model. In contrast, at deeper depths, the horizontal averaging seems to provide better agreement.

#### 6.3.2 Limb-darkening

Fig. 6.6 shows the limb-darkening curves corresponding to the considered 1D models as well as the limb-darkening observed by Neckel & Labs (1994). The agreement is good at long wavelengths but all models display a small bump at shorter wavelengths (they are excessively concave, which appears clearly at heliocentric angles near  $\mu=0.4$ ). Since the original FAL-C model was constructed in order to give perfect agreement with the observations, and the two 1D models derived from 3D simulations and the FALC390 model are closer to each other than they are to the observations, we suspect slight inaccuracies in the non-scattering opacities. It could also be that the bilinear 4-point interpolation of the radiative transfer quantities (see Sect. 6.2.3) is not sufficient to reach an acceptable accuracy.

The v50-flat and roe-flat models are not shown in Fig. 6.6 in order to keep it not too busy, but the corresponding curves are clearly discrepant with all

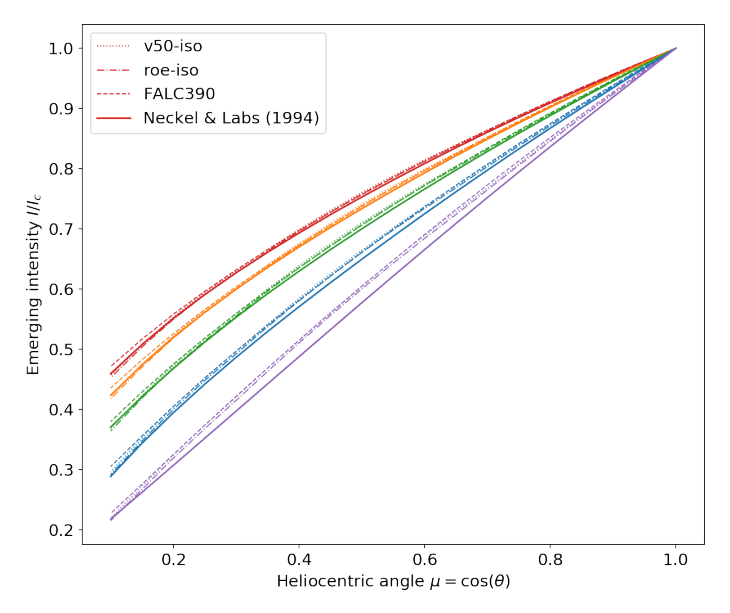


Figure 6.6. Limb-darkening curves of the considered 1D models and observations at a variety of wavelengths in the visible spectrum: 3880 Å(violet), 4560 Å(blue), 5350 Å(green), 6040 Å(orange) and 6565 Å(red). The emerging intensity is normalized by its own value,  $I_c$ , at disc centre.

other curves, as can already be expected from their corresponding temperature structure in Fig. 6.5.

#### 6.3.3 Centre-to-limb variation of polarization

Fig. 6.7 shows the centre-to-limb variation of the polarization of the considered 1D models, as well as of the semi-empirical curve established with Eq. (6.8) (here referred as Fluri & Stenflo 1999) with the parameters corresponding to the FAL-C model and the limb-darkening curve of, respectively, Neckel & Labs (1994) referred as NL1994 and our own radiative transfer modelling referred as FALC390. The agreement is again better in the red than in the blue part of the spectrum.

Since the thick curves (solid and dashed) are both computed from the same semi-empirical formula, with the same parameters, but with different limb-darkenings, the discrepancy between the two provides a qualitative idea of how limb-darkening affects the centre-to-limb variation of polarization.

On the contrary, the FALC390 model (thin dashed curve) and the semiempirical model using the FALC390 limb-darkening (thick solid line) should exactly match if the opacities used by Fluri & Stenflo (1999) and the opacities we computed with the RH routines (Uitenbroek 1998) were identical and

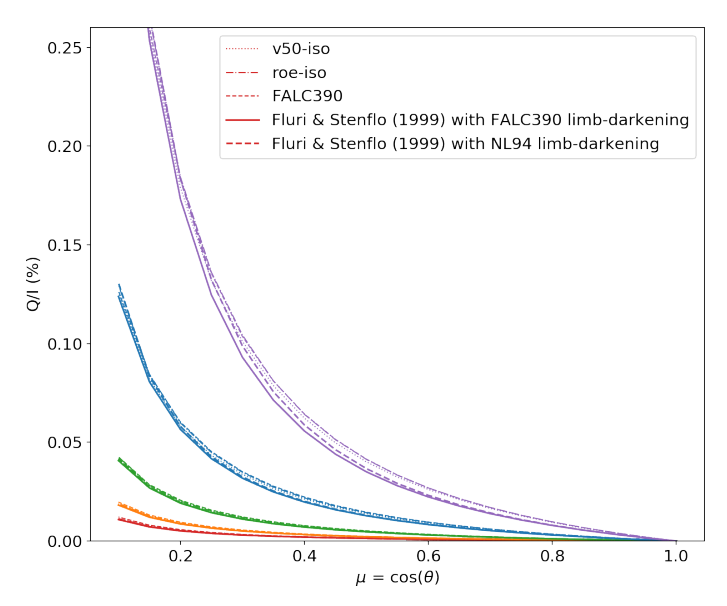


Figure 6.7. Centre-to-limb variation of the continuum polarization of the considered 1D models at a variety of wavelengths in the visible spectrum: 3880 Å(violet), 4560 Å(blue), 5350 Å(green), 6040 Å(orange) and 6565 Å(red). Fluri & Stenflo (1999) refers to the semi-empirical formula given in Eq. (6.8) with the parameters of the FAL-C model and the limb darkening either obtained from the FALC390 interpolated model or from the observations of Neckel & Labs (1994) referred as NL94 in the caption.

if the two radiative transfer codes are both accurate. Here, we attribute the discrepancy to mismatches in the computed opacities. Since the RH code provides routines to compute a generous amount of contributions to the scattering opacities, we suspect that the slightly lower polarization appearing in the semi-empirical curve with the FALC390 limb-darkening is rather due to missing contributions in the scattering-opacities that were used in order to determine the parameters of the semi-empirical model rather than to discrepancies in the non-scattering opacities. At longer wavelengths the same discrepancies appear, although they are not fully visible in Fig. 6.7.

An other possible representation of the same data is given in Fig. 6.8, in which the linear polarization is plotted as a function of wavelength for a selection of heliocentric  $\mu$  values.

### 6.4 The continuum from 3D models

Carrying out the present investigation from high-resolution 3D models rather than from 1D models is a computationally intensive task and requires involved

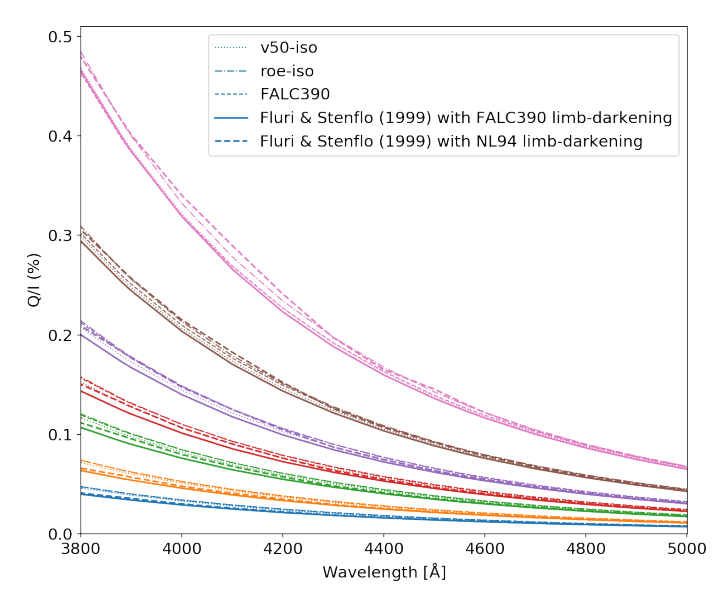


**Figure 6.8.** Polarized spectrum at a variety of heliocentric angles: from top to bottom,  $\mu = 0.1, 0.15, 0.2, 0.25, 0.3, 0.4, 0.5$ .

codes and post-processing tools. The 1D modelling already gave us a lot of insight on the polarized continuum. However, there are two questions that cannot be answered with 1D modelling. First, we would like to know how the spatially averaged polarized spectrum and centre-to-limb variation of polarization compare to the 1D modelling. There is the possibility that radiative transfer over the averaged internal structure of a 3D atmosphere on isosurfaces of constant optical depth would not yield the same polarization as the spatial average of the emerging polarization from the full 3D atmosphere. Second, since the surface of the Sun is corrugated by convective cells, at granular scale, cylindrical symmetry with respect to lines-of-sight is broken also when looking at disc centre. A non-zero amount of polarization is hence expected at small scales anywhere on the solar disc, and the 3D structures should also appear in polarization maps. This further investigation obviously requires high-resolution 3D modelling.

#### 6.4.1 Polarization maps at disc centre

For the magnetic model d3gt57g44v50fc.134051, the calculated intensity and polarization maps are shown in Fig. 6.9 at disc centre. The top left panel shows temperature at the isosurface of constant bolometric optical depth, whereas the top right panel displays a map of the emergent monochromatic intensity contrast,  $I/\langle I \rangle - 1$ . As expected, both quantities faithfully reproduce the

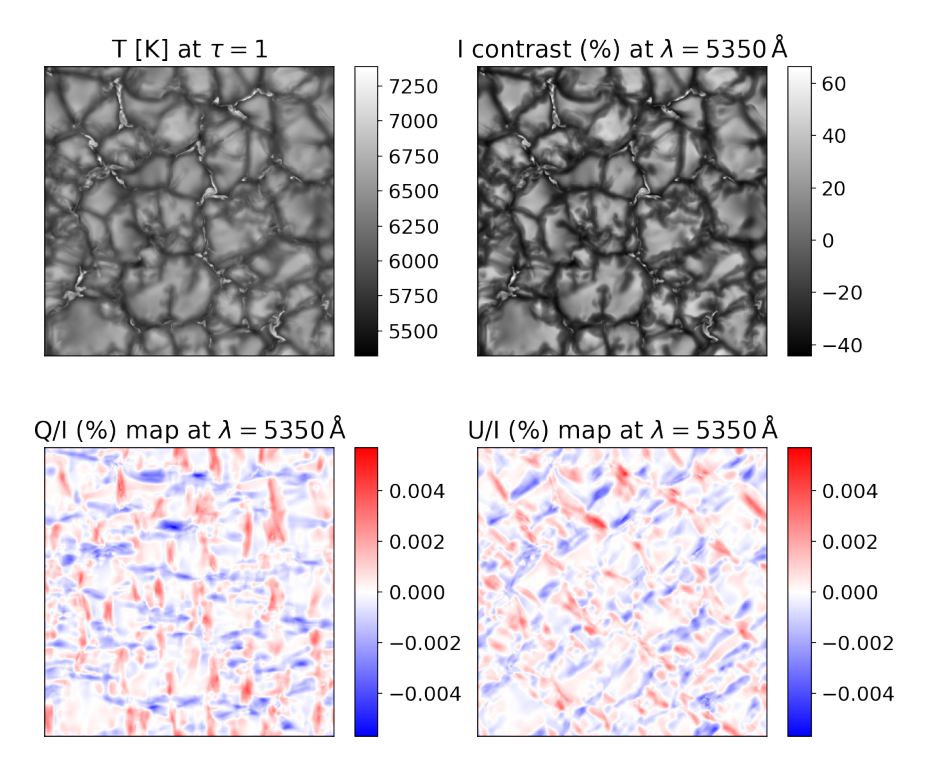
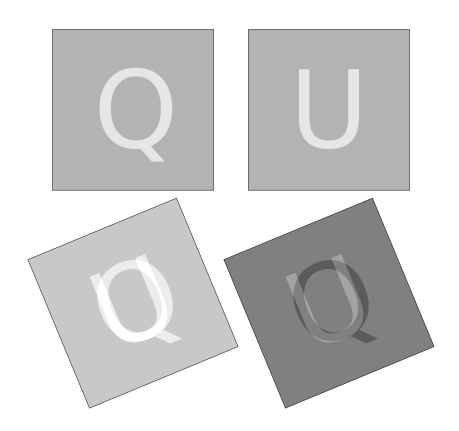


Figure 6.9. Temperature structure on the isosurface of unit bolometric optical depth and intensity contrast of the d3gt57g44v50fc.134051 model (top row) and linear polarization Q/I and U/I from the same model (bottom row). All maps cover a horizontal field of view of  $9.6 \times 9.6 \,\mathrm{Mm}^2$ .

solar granulation pattern and are very similar, except for the fact that the monochromatic emerging intensity image is sharper than the temperature map.

The bottom maps of Fig. 6.9 display small but non-zero polarization signals, that go up to  $10^{-5}$  both for Q/I and for U/I. We note that we consider here the linear components of the emergent polarization Q and U normalized by the local emergent intensity I. Q/I displays a chequered pattern, and U/I displays the same pattern rotated by an angle of  $45^{\circ}$ . Since, at disc centre, the Sun is essentially invariant under rotation around line-of-sight, one expects at first glance no preferred orientation. There are two equivalent ways of understanding this pattern. From an observational point of view, even if there is no preferred direction at disc centre, the observer breaks the symmetry by choosing a certain orientation for the polarimeter. In the same way, in the numerical simulations, the definition of Q and U requires the definition of a reference angle, that breaks the symmetry.

An alternative and more formal approach is to note that Q and U are not invariant under geometric rotations. There is a well defined way in which the



**Figure 6.10.** Rotation of fake Q and U maps by an angle of  $30^{\circ}$ .

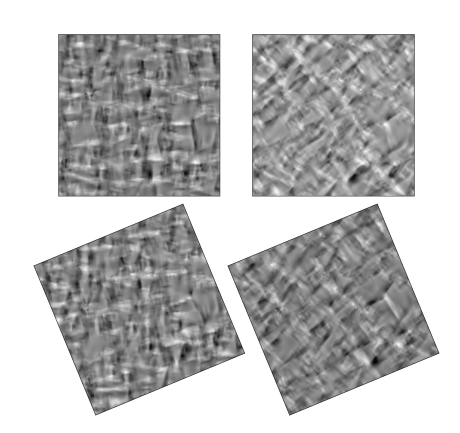


**Figure 6.11.** Rotation of simulated Q and U maps by an angle of  $30^{\circ}$ .

Stokes vector transforms under rotation, that includes both a geometric rotation and a mixing of the components of the Stokes vector. This appears clearly in Fig. 6.10, in which the Q and U maps are artificial. Instead, in Fig. 6.11, realistic Q and U maps with their corresponding chequered patterns are appropriately rotated. The patterns, however, remain invariant under rotation, as expected. This pattern is therefore not a numerical artefact from the computational grid on which the physical quantities are discretized: it is a pattern intrinsic to the definition of the Stokes vector.

At the solar limb, light is mainly polarized parallel to it. With the present and usual definition of the Stokes parameters, at the solar limb we have positive Q signals and almost zeros signals in Stokes U. For this reason Stokes Q is usually used as a measure for linear polarization. However, at disc centre and with high resolution simulations, there is no real distinction between Stokes Q and Stokes U, and both carry the same amount of polarization. The relevant quantity is the total amount of polarization,  $P \equiv \sqrt{Q^2 + U^2}$ . Under rotations P has also a simpler transformation law than Q and U, since it simply rotates geometrically and does not mix components with any other quantity. We will later show and discuss maps of P.

#### 6.4.2 Limb-darkening

Maps of the intensity contrast of the d3gt57g44v50fc.134051 model are shown in Fig. 6.12 for lines-of-sight of different inclination angles  $\mu$  in the continuum at a wavelength of  $\lambda = 5350\,\text{Å}$ . Granules are well visible at all heliocentric angles  $\mu$ . It should however be noted that the overall contrast diminishes from disc centre to solar limb, and it has been enhanced in Fig. 6.12 by adapting the grey-scale map.

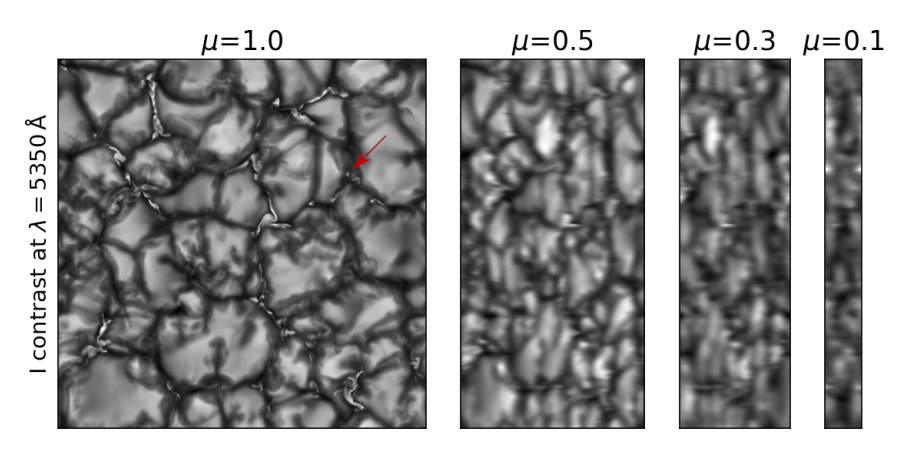


Figure 6.12. Intensity contrast maps along different lines-of-sight defined by the heliocentric angle  $\mu = \cos(\theta)$ , at wavelength  $\lambda = 5350$  Å. The contrast is normalized to the average intensity over each individual map, so that the limb-darkening is not apparent on this figure: each map has its own grey scale. At disc-centre, the intensity contrast extends approximately from -45% (black) up to 65% (white), whereas at the limb the range is reduced, going from -15% up to 30%. A bright point is signalled with the red arrow.

The spatially averaged limb-darkening curves corresponding to the models d3gt57g44v50fc.134051 and d3gt57g44roefc.56016 is shown in Fig. 6.13, together with the corresponding 1D models averaged over isosurfaces of constant bolometric optical depth, v50-iso and roe-iso respectively, as well as the observations of Neckel & Labs (1994). The discrepancy between the 3D modelling and the 1D modelling is striking. The 3D modelling shows an excess of intensity at intermediate heliocentric angles. In fact, all numerical models we have studied, both 1D and 3D, produce limb-darkening curves with a an excess of concavity, at intermediate heliocentric angles, that is particularly pronounced in the 3D high-resolution modelling. We did not find a definitive explanation for this behaviour. A possible explanation resides in the Cartesian grid we used in radiative transfer instead of the more appropriate spherical grid. From a purely geometric point of view, equally long inclined rays directed with an angle corresponding to  $\mu = 0.5$  reach 10 km deeper in the Cartesian grid than in the spherical grid, hence probing, in some places, significantly hotter structures. 1D models and low-resolution 3D models are of course also affected, but possibly in a less significant way, since the atmosphere is horizontally averaged/smoothed. This explanation is however not compatible with the 3D modelling of Trujillo Bueno & Shchukina (2009), who used a snapshot that resulted from the hydrodynamic model of Asplund et al. (2000). Trujillo Bueno & Shchukina (2009) find indeed an emerging intensity that is systematically too low at intermediate heliocentric angles. However, since the adopted opacities are different in the two models, a fair comparison is not possible. In

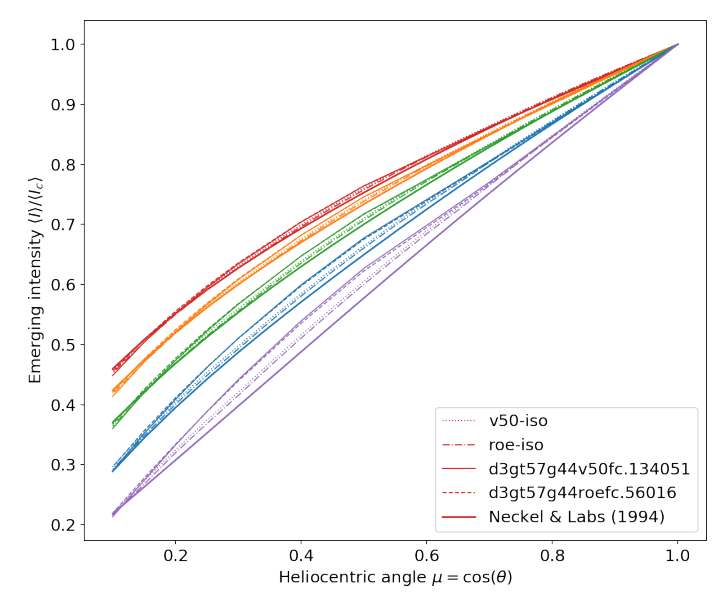


Figure 6.13. Spatially averaged limb-darkening curves of the considered 3D models, together with the corresponding 1D averaged models and the observations of Neckel & Labs (1994), at a variety of wavelengths in the visible spectrum: 3880 Å(violet), 4560 Å(red), 5350 Å(green), 6040 Å(orange) and 6565 Å(blue). The emerging intensity is normalized by its own value at disc centre  $I_c$ .

addition, since our 1D models as well as the FALC390 model already show a bit too high intensities with respect to the limb-darkening of Neckel & Labs (1994), we could also have underestimated the non-scattering opacities. Some evidence of it is given by the fact that the same FALC390 limb-darkening curve as computed by Fluri & Stenflo (1999), FALC<sub>5</sub> in Fig. 3 of the cited paper, seems to have a slightly better agreement with the observations of Neckel & Labs (1994).

#### 6.4.3 Centre-to-limb variation of polarization

In spite of the difficulties that emerged from the spatially averaged limb-darkening curves, we still continue our study of the continuum with the centre-to-limb variation of polarization. We know that inaccuracies in the limb-darkening curve are not so strongly reflected in the centre-to-limb variation of polarization. This appeared clearly when comparing the FALC390 model with the observations of Neckel & Labs (1994) in Fig. 6.6. The relative difference in the limb-darkening between these two models is similar to the relative difference between the 3D models and their 1D counterpart, and this relative difference is only slightly reflected on the variation of polarization appearing

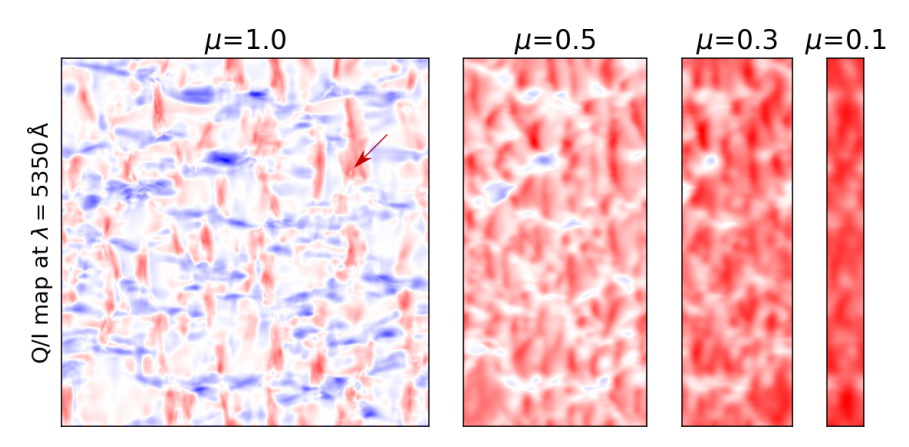


Figure 6.14. Q/I polarization maps along lines-of-sight of different inclination angles defined by the heliocentric angle  $\mu=\cos(\theta)$ , at wavelength  $\lambda=5350\,\text{Å}$ . At disc-centre, the polarization signal extends approximately from  $-6\times10^{-5}$  (blue) up to  $6\times10^{-5}$  (red), whereas at the limb the range is one order of magnitude more extended, going from  $-6\times10^{-4}$  up to  $6\times10^{-4}$ . The colour map is divergent and centred at zero polarization (white); the Q signal has to preferred sign at disc centre but clearly favours positive sign at the limb. The bright point signalled with the red arrow now appears as a tiny depolarized point.

in Fig. 6.7.

We have shown that the meaningful physical quantity describing linear polarization is  $P=\sqrt{Q^2+U^2}$ . It is however still interesting to consider maps of Q/I, since their spatial average is later used to compare our simulations with observations and with past 1D modelling. These polarization maps are shown in Fig. 6.14. The corresponding maps of total linear polarization are shown in Fig. 6.15. At disc centre, the granules appear as regions of extremely low polarization. This is well understood since the granules have in a good approximation a cylindrical symmetry along the normal direction, that coincides with the line-of-sight at disc centre. Hence, the perpendicular component to the line-of-sight of te radiation field is isotropic. This symmetry obviously breaks with inclined rays, since temperature has a strong temperature gradient along the vertical direction within granules, which renders them brighter than the intergranular lanes at inclined angles.

Similarly, at disc centre, the magnetic bright features/points that reside in the intergranular lanes appear as regions of low linear polarization. This happens for the same reason for which granules are also darker: these magnetic features are horizontally homogeneous regions, and hence the horizontal component of the radiation field is isotropic. We note that normalizing the linear polarization by the intensity accentuates the contrast difference between the depolarized features and the surrounding areas, but these features already appear as regions of low polarization in maps of pure linear polarization with-

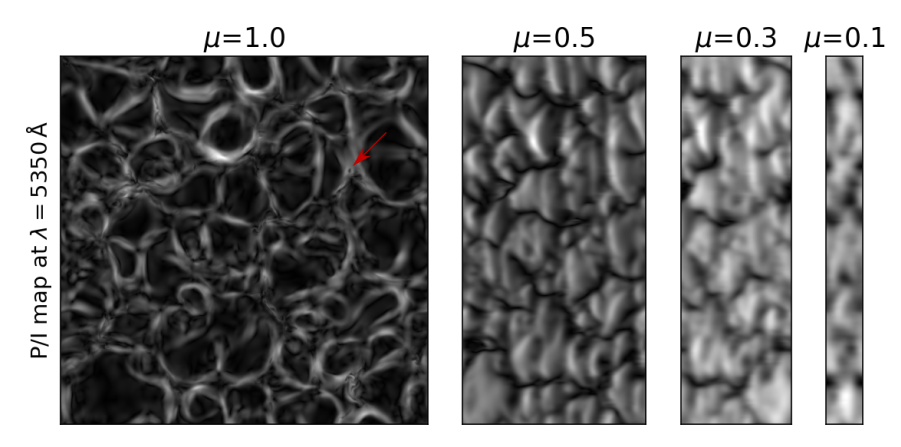


Figure 6.15. P/I polarization maps along different lines-of-sight defined by the heliocentric angle  $\mu=\cos(\theta)$ , at wavelength  $\lambda=5350\,\text{Å}$ . At disc-centre, the polarization signal extends approximately from zero polarization (black) up to  $6\times10^{-5}$  (white), whereas at the limb the range extends from  $2\times10^{-4}$  up to  $6\times10^{-4}$ . The bright point signalled with the red arrow appears again as a tiny depolarized point. Note that the maps for inclined line-of-sight correspond to the middle-left limb, and not to the middle-right limb!

out any normalization. A selected bright point is marked in Figs. 6.12, 6.14 and 6.15.

The spatially averaged centre-to-limb variation of the linear polarization  $\langle Q \rangle / \langle I \rangle$  of the considered 3D models is shown in Fig. 6.16, together with the corresponding 1D averaged models as well as the curve obtained by using the semi-empirical formula of Eq. (6.8) with, respectively, the FALC390 limb-darkening and the observed limb-darkening of Neckel & Labs (1994). The agreement between all curves for linear polarization is impressive, and much better than for the intensity, as seen in the limb-darkening plot of Fig. 6.13. This suggests that the scattering opacities are less sensitive to small variations of temperature and density than the non-scattering opacities.

### 6.4.4 The contribution of the far red wing of Lyman- $\beta$

As anticipated in Sec. 6.2.2, the red wing of Lyman- $\beta$  is expected to play an important role in the centre-to-limb variation of polarization, especially towards the limb, because at the depth range in which the continuum is formed for inclined rays the Rayleigh scattering absorption coefficient due to the far red wing of Lyman- $\beta$  dominates the absorption coefficient for Thomson scattering at free electrons (Fig. 6.3).

Fig. 6.17 shows, among other data, the averaged linear polarization  $\langle Q \rangle / \langle I \rangle$  at heliocentric angle  $\mu = \cos(\theta) = 0.1$  for the considered 3D models at a selected number of wavelenghts. For the 3D model d3gt57g44v50fc.134051,

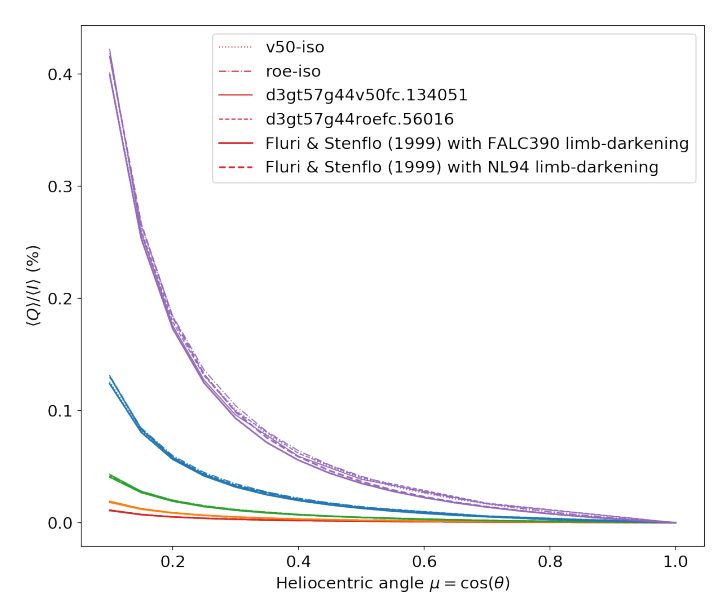


**Figure 6.16.** Spatially averaged centre-to-limb variation of the linear polarization  $\langle Q \rangle / \langle I \rangle$  of the considered 3D models, together with the corresponding 1D averaged models as well as the corresponding determination using the semi-empirical formula of Eq. (6.8) with the FALC390 limb-darkening and the observed limb-darkening of Neckel & Labs (1994).

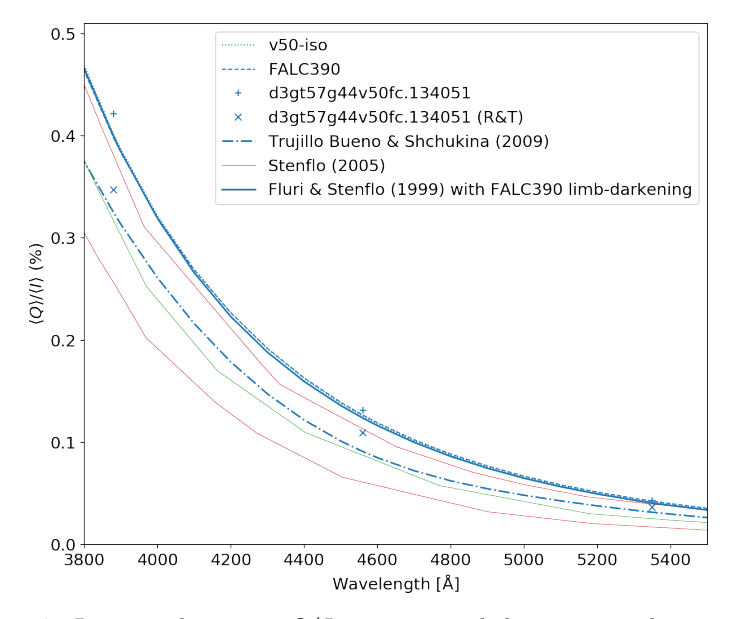


Figure 6.17. Linear polarization Q/I spectrum at heliocentric angle  $\mu = \cos{(\theta)} = 0.1$  for a selection of 1D models and spatially averaged linear polarization  $\langle Q \rangle / \langle I \rangle$  for the d3gt57g44v50fc.134051 3D model, for the model of Asplund et al. (2000) as computed by Trujillo Bueno & Shchukina (2009), as well as the semi-empirical determination of Stenflo (2005) (thin green solid line) with the corresponding lower and upper bounds (thin red solid lines). For the model d3gt57g44v50fc.134051, only a reduced amount of data is available, but the computations has been carried out twice, once including all available scattering opacities listed in Sec. 2.2.4, once including only both Rayleigh scattering in the far wing of Lyman- $\alpha$  and Thomson scattering ("R&T" label in the legend), as it was done by Trujillo Bueno & Shchukina (2009).

the points are plotted, once including all available scattering opacities (see Sec. 2.2.4), and once including Rayleigh scattering in the far wing of Lyman- $\alpha$  (as given by Eq. (6.7)) and Thomson scattering alone. We label this second curve that includes a limited number of scattering opacities with the letters "R&T". By far, the most important missing contribution in this second choice is the far red wing of Lyman- $\beta$ . We deduce from these two curves that this contribution is not negligible.

In Fig. 6.17 we also observe a significant discrepancy between the FALC390 model of Fluri & Stenflo (1999) and the later semi-empirical determination of Stenflo (2005). Trujillo Bueno & Shchukina (2009) find an excellent agreement between their own 3D synthesis and the semi-empirical curve of Stenflo (2005), which mislead to the conclusion that the precise evaluation of linear polarization in the continuum requires realistic 3D modelling. However, our own calculations suggest that, to the contrary, spatial averages of linear polarization from 3D maps are extremely close to all considered 1D synthesis. In fact, Trujillo Bueno & Shchukina (2009) neglected the contribution of the red far wing of Lyman- $\beta$ , and therefore missed a significant amount of polarization, in such a way that their curve would agree with the semi-empirical determination of Stenflo (2005). However, our calculations suggest that the polarization curve of Fluri & Stenflo (1999) is the correct one.

#### 6.5 Discussion and conclusions

In this contribution we have presented the methods and tools for computing radiative transfer of polarized radiation, both from 1D and 3D models. We propose a natural way of reducing 3D models to equivalent 1D models, and we have synthesized polarization maps from two snapshots of two of our numerical M(HD) simulations, one magnetic, the other non-magnetic. The synthesis of both polarized and non-polarized spectra from the two simulations did not show any significant difference. The comparison of the limb-darkening from the 3D model atmospheres to the limb-darkening from 1D atmospheres gave significant discrepancies that we have not yet fully understood. The possible factors contributing to these differences are the Cartesian nature of the grid, a possibly inaccurate computation of the non-scattering opacities, and a possibly inaccurate bilinear 4-point interpolation of the radiative transfer quantities. These verifications would required additional investigations.

Instead, the linearly polarized spectrum shows am excellent agreement among all the computations we carried out and with the computations of Fluri & Stenflo (1999). It however exhibits a significantly higher polarization than the corresponding spectrum from the 3D calculations of Trujillo Bueno & Shchukina (2009) and from the semi-empirical determination of Stenflo (2005). We can partially explain the discrepancy between the former 3D calculations

and our own by the missing Lyman- $\beta$  opacities in the computation of Stenflo (2005). Since the determination of Stenflo (2005) relies on a model for depolarizing lines, the difference could be attributed to such a model, but a deeper investigation is required to proof or falsify this hypothesis, and presently we must consider this problem as an open question.

A more theoretical and interesting question is how the source functions for the different Stokes components compare. Since the Stokes components in the radiative transfer equation decouple for the continuum, we have seen that the formal transfer is the same for intensity and polarization. The only difference between the emerging intensity and polarization is then encoded in the corresponding source functions. As a first approximation, we have concluded that both intensity and polarization form in the same layers, but Fluri & Stenflo (1999) already showed that in some models there are chromospheric contributions and non-LTE effects in the polarized spectrum, which would be interesting to reproduce with 3D radiative transfer.

A last and very important extension to this investigation would be the inclusion of additional models or additional snapshots of the same model in order to improve the statistics. Our limited number of models seems to suggest that the model-dependence is not as significant as the dependencies on scattering and non-scattering opacities, but this conclusion should be revisited after improving the statistics.

#### Bibliography

- Asplund, M., Nordlund, Å., Trampedach, R., & Stein, R. F. 2000, "Line formation in solar granulation. II. The photospheric Fe abundance", A&A, **359**, 743 [astro-ph/0005321]
- Baschek, B. & Scholz, M. 1982, *Radiative processes*, ed. K. Schaifers & H. H. Voigt (Berlin, Heidelberg: Springer Berlin Heidelberg), 100–106
- Chandrasekhar, S. 1946, "On the Radiative Equilibrium of a Stellar Atmosphere. XI.", ApJ, 104, 110
- Chandrasekhar, S. 1960, Radiative transfer
- Collados, M., Bettonvil, F., Cavaller, L., et al. 2010, "European Solar Telescope: Progress status", Astron. Nachr., **331**, 615
- Fluri, D. M. & Stenflo, J. O. 1999, "Continuum polarization in the solar spectrum", A&A, 341, 902
- Fontenla, J. M., Avrett, E. H., & Loeser, R. 1993, "Energy balance in the solar transition region. III - Helium emission in hydrostatic, constant-abundance models with diffusion", ApJ, 406, 319

Gandorfer, A. 2000, The Second Solar Spectrum: A high spectral resolution polarimetric survey of scattering polarization at the solar limb in graphical representation. Volume I: 4625 Å to 6995 Å

- Gandorfer, A. 2002, The Second Solar Spectrum: A high spectral resolution polarimetric survey of scattering polarization at the solar limb in graphical representation. Volume II: 3910 Å to 4630 Å
- Gandorfer, A. 2005, The Second Solar Spectrum: A high spectral resolution polarimetric survey of scattering polarization at the solar limb in graphical representation. Volume III: 3160 Å to 3915 Å
- Harrington, J. P. 2015, "Polarized Continuum Radiation from Stellar Atmospheres", in IAU Symposium, Vol. 305, *Polarimetry*, ed. K. N. Nagendra, S. Bagnulo, R. Centeno, & M. Jesús Martínez González, 395–400
- Keil, S. L., Rimmele, T. R., Wagner, J., & ATST Team. 2010, "Advanced Technology Solar Telescope: A status report", Astron. Nachr., 331, 609
- Kostogryz, N. M. & Berdyugina, S. V. 2015, "Center-to-limb polarization in continuum spectra of F, G, K stars", A&A, 575, A89 [arXiv:1408.5019]
- Kostogryz, N. M., Milic, I., Berdyugina, S. V., & Hauschildt, P. H. 2016, "Center-to-limb variation of intensity and polarization in continuum spectra of FGK stars for spherical atmospheres", A&A, 586, A87 [arXiv:1511.07213]
- Kostogryz, N. M., Yakobchuk, T. M., & Berdyugina, S. V. 2015, "Polarization in Exoplanetary Systems Caused by Transits, Grazing Transits, and Starspots", ApJ, 806, 97 [arXiv:1504.02943]
- Kunasz, P. & Auer, L. H. 1988, "Short characteristic integration of radiative transfer problems Formal solution in two-dimensional slabs", J. Quant. Spec. Radiat. Transf., 39, 67
- Landi Degl'Innocenti, E. & Landolfi, M. 2004, Astrophysics and Space Science Library, Vol. 307, *Polarization in Spectral Lines* (Kluwer Academic Publishers)
- Leroy, J. L. 1972, "New Measurements of the Polarization of Photospheric Light near the Solar Limb", A&A, 19, 287
- Manso Sainz, R. & Trujillo Bueno, J. 2003, "A Multilevel Radiative Transfer Program for Modeling Scattering Line Polarization and the Hanle Effect in Stellar Atmospheres", in ASP Conference Series, Vol. 307, Solar Polarization, ed. J. Trujillo Bueno & J. Sanchez Almeida, 251

Mickey, D. L. & Orrall, F. Q. 1974, "Broadband Polarization Measurements on the Quiet Sun's Disk near λ 5834", A&A, **31**, 179

- Neckel, H. 1996, "On the wavelength dependency of solar limb darkening ( $\lambda\lambda$  303 to 1099 nm)", Sol. Phys., **167**, 9
- Neckel, H. & Labs, D. 1994, "Solar limb darkening 1986-1990 ( $\lambda\lambda$  303 to 1099 nm)", Sol. Phys., **153**, 91
- Stenflo, J. O. 2005, "Polarization of the Sun's continuous spectrum", A&A, 429, 713
- Stenflo, J. O., Bianda, M., Keller, C. U., & Solanki, S. K. 1997, "Center-to-limb variation of the second solar spectrum.", A&A, 322, 985
- Trujillo Bueno, J. & Manso Sainz, R. 1999, "Iterative Methods for the Non-LTE Transfer of Polarized Radiation: Resonance Line Polarization in One-dimensional Atmospheres", ApJ, 516, 436
- Trujillo Bueno, J. & Shchukina, N. 2009, "Three-dimensional Radiative Transfer Modeling of the Polarization of the Sun's Continuous Spectrum", ApJ, 694, 1364 [arXiv:0812.3494]
- Uitenbroek, H. 1998, "The Effect of Photospheric Granulation on the Determination of the Lithium Abundance in Solar-Type Stars", ApJ, 498, 427
- Štěpán, J. & Trujillo Bueno, J. 2011, "Scattering Polarization of Hydrogen Lines in Weakly Magnetized Stellar Atmospheres. I. Formulation and Application to Isothermal Models", ApJ, 732, 80 [arXiv:1102.4012]
- Štěpán, J. & Trujillo Bueno, J. 2013, "PORTA: A three-dimensional multilevel radiative transfer code for modeling the intensity and polarization of spectral lines with massively parallel computers", A&A, 557, A143 [arXiv:1307.4217]
- Wiehr, E. 1978, "Measurement of solar disc polarization in a number of Fraunhofer lines and their adjacent continuum. II - Improved data, new line measurements", A&A, 67, 257
- Wiehr, E. & Bianda, M. 2003, "High spatial resolution solar polarimetry with interference filters", A&A, 398, 739

# Conclusion

This scientific contribution encompasses four different projects: the study of the evolution of the non-solenoidal component of the numerically evolved magnetic field in simulations using constrained transport methods (Chapter 3), the study of non-magnetic bright points appearing in the intergranular lanes of synthetic observations of the Sun (Chapter 4), the study of the immediate vicinity of the Balmer limit in the isolated Hydrogen atom by making a semi-analytic model of the total cross-section as a function of wavelength (Chapter 5), and the study of the linearly polarized solar continuum through synthetic observations (Chapter 6). The synthesis of the simulations used in these projects is also part of this work.

The use of numerical radiative (magneto-)hydrodynamic simulations, solar spectropolarimetry and radiative transfer are the recurrent topics that relate all these projects to each other. Although apparently independent, these topics emerged naturally throughout different developments of the research that lead to this Ph.D. thesis. Accordingly, distinct results and ideas for new investigations originated and where discussed in the corresponding conclusions for each chapter. We summarize here the main points.

Regarding the emergence of non-solenoidal magnetic fields in  ${\rm CO^5BOLD}$  simulations using constrained transport, the results are very satisfactory. In the typical 2 h time sequences spanned by our high-resolution simulations, no significant increase of the divergence of the magnetic field was observed. Longer but lower resolution models also performed extremely well.

Non-magnetic bright points (nMBPs) are shown to be an observable manifestation of vertically directed vortex tubes, in which the centripetal force is provided by the gradient pressure, hence sustaining a region with low-density plasma. This region is consequently more transparent than the surrounding plasma, allowing for photons to escape from deeper regions and to produce an enhanced intensity in the emerging light. This second project lead to the development of an algorithm for the detection of nMBPs and to a corresponding statistical study. The diameter of nMBPs is approximately  $60-80\,\mathrm{km}$ , and their bolometric intensity contrast is approximately 20% with respect to their immediate intergranular surroundings. Their lifespan ranges from approximately  $30\,\mathrm{s}$  up to the granular lifetime of a few minutes. Their small size makes them barely detectable with present telescopes, but we expect that the new generation of solar telescopes will be able to resolve such features.

The third project started with the naive question is there a discontinuity at the Balmer limit and lead to a semi-analytical modelling of the total cross-section due to bound-bound and bound-free transitions from the n=2 energy level of the isolated Hydrogen atom. We proved from quantum mechanical grounds and with modern formalism that there is no discontinuity at the Balmer limit, but a rapid drop of the lower-envelope of the total cross-section. We proposed a definition for the location of the Balmer jump and showed that its exact wavelength sensibly depends on the broadening mechanisms that come into play. We left the study of the interactions of the Hydrogen atom with the surrounding plasma as well as the computation of radiative transfer for a future work.

Finally, the study of linear polarization in the continuum and its centre-to-limb variation left a number of incognitos. An important result is that the far wing of Lyman- $\beta$  is a non-negligible contributor to scattering polarization with a contribution to the total corresponding absorption coefficient that is comparable to that of Thomson scattering at free electrons. However, the number of parameters that enter when computing opacities and radiative transfer significantly complicates the task of disentangling the different contributions to the emerging spectrum. With our methods the spatially averaged polarization is extremely similar in all of our models, but when comparing all available synthetic and real observations with each other we find discrepancies that remain unexplained at the present time. New and independent observations are advisable before making any final conclusion. The polarization maps revealed, at disc-centre, the familiar structure of the solar granulation, in which granules appear with almost-zero linear polarization, and integranular lanes exhibit a small but significant linear polarization of the order of  $5 \times 10^{-5} - 6 \times 10^{-5}$ .

# High-resolution simulations of the solar photosphere with focus on the polarimetry of the solar continuum

#### Abstract:

This Ph.D. dissertation combines four distinct projects in solar physics. They have the common thread of using high-resolution (magneto-)hydrodynamic numerical simulations of the Sun, extending from the upper convective layers up to the lower chromosphere. Solar spectropolarimetry and radiative transfer are the two other commonalities relating these projects. The present thesis hence embraces a broad field. One of the projects is devoted to the study of bright points appearing in the intergranular lanes in magnetic field-free simulations, to the understanding of their existence independently of magnetic fields, and to the statistical study of them. Since the size of the bright points is barely below the spatial resolution capabilities of present solar telescopes, this project makes a prediction arising from numerical simulations alone, and this prediction can possibly be verified in the near future with the new generation of solar telescopes. The study of the divergence of the magnetic field in numerical simulations is an other aspect of this research work. Since all numerical schemes are subject to round-off errors, verifying the ability of the used algorithmic to maintain the field divergence-free is required in order to exclude a significant contribution of unphysical forces in our modelling. A third project deals with the total cross-section due to bound-free and bound-bound electronic transitions in the isolated Hydrogen atom from the n=2 lower energy level. It is shown using a modern formalism that the total cross-section as a function of wavelength has no discontinuity at the Balmer limit, but a sharp rise of the cross-section when approaching the Balmer limit from the red side. The location of the sharp increase of the cross-section is shown to sensibly depend on the various mechanisms of spectral line broadening. The final project is a study of the linearly polarized light in the continuum radiation from the Sun, which was synthesized from the high-resolution simulations of the first project. The observable quantity that is compared to available observations and earlier model calculations is the centre-to-limb variation of the spatially averaged linear polarization. Discrepancies among the distinct available data suggest that further observations are required in order to draw conclusions. Additionally, we synthesize maps of linear polarization at different heliocentric angles. The maps at disc-centre are of particular interest, since they exhibit a small yet significant polarization due to the corrugated rather than plane-parallel surface of the Sun. This small level of polarization will have to be taken into account in the calibration procedures of the polarimeters of the new generation of telescopes.

#### **Keywords:**

magnetohydrodynamics (MHD) – hydrodynamics – Sun: photosphere – Sun: granulation – magnetic fields – turbulence – polarization – scattering – line: profiles – atomic process – opacity

# High-resolution simulations of the solar photosphere with focus on the polarimetry of the solar continuum

#### Résumé:

Cette dissertation doctorale aborde quatre suiets différents de la physique solaire. L'utilisation de simulations numériques (magnéto-)hydrodynamiques (MHD) s'étendant de la haute couche convective à la basse chromosphère est une caractéristique commune. La spectropolarimétrie ainsi que le transfert radiatif sont aussi deux sujets récurrents. Cette thèse doctorale couvre donc un large spectre. L'un des projets est consacré à l'étude de points brillants apparaissant dans la région intergranulaire, dans les simulations privées de champs magnétiques. On v explique leur existence, indépendamment des champs magnétiques, et on les étudie d'un point de vue statistique. Comme leur taille est légèrement plus petite que la résolution spatiale des présents télescopes solaires, ce projet réalise une prédiction basée uniquement sur les simulations. Celle-ci pourra être vérifiée dans un avenir proche, avec les nouveaux télescopes solaires. L'étude de la divergence du champ magnétique dans les simulations est un des autres sujets de ce travail de recherche. Toutes les méthodes numériques sont en proie aux erreurs d'arrondi, et vérifier que ces méthodes parviennent malgré tout à limiter la divergence du champ magnétique est nécessaire pour exclure l'existence d'importantes forces artificielles. Un troisième projet traite de la section efficace totale des processus de transition électronique lié-libre et lié-lié de l'atome d'hydrogène isolé, à partir de son niveau d'énergie n=2. On y démontre, avec un formalisme moderne, que la section efficace totale comme fonction de la longueur d'onde n'a pas de discontinuité à la limite de Balmer, mais une accroissement rapide en approchant la limite par le rouge. On montre que la position exacte de cet accroissement dépend des différents mécanismes d'élargissement des lignes spectrales. Le dernier projet est une étude de la lumière polarisée émergente de la partie continue du spectre solaire; on y fait usage des simulations à haute résolution pour la synthèse des données nécessaires. La variation centre-bord de la moyenne spatiale de la lumière polarisée linéairement est la quantité utilisée pour comparer les observations et les différents modèles numériques. Compte tenu des désaccords entre les différentes données, de nouvelles observations seront nécessaires pour tirer des conclusions solides. En outre, dans le cadre de ce projet, nous générons des observations synthétiques du soleil à différents angles héliocentriques. Celles correspondant au centre du soleil sont particulièrement intéressantes, du fait qu'elles présentent une polarisation petite mais bien présente, due à la surface ondulée et inhomogène du soleil. Ce petit niveau de polarisation devra être pris en compte dans les procédures de calibration des polarimètres de la nouvelle génération de télescopes.

#### Mots-clés:

magnétohydrodynamique (MHD) – hydrodynamique – Soleil: photosphère – Soleil: granulation – champs magnétiques – turbulence – polarisation – diffusion – lignes spectrales: profils – processus atomiques – opacité